All ETDs from UAB

UAB Theses & Dissertations

2014

High Spatiotemporal Resolution Mapping Of Retinal Physiology

Qiuxiang Zhang
University of Alabama at Birmingham

Follow this and additional works at: https://digitalcommons.library.uab.edu/etd-collection

Recommended Citation

HIGH SPATIOTEMPORAL RESOLUTION MAPPING OF RETINAL PHYSIOLOGY

by

QIUXIANG ZHANG

XINCHENG YAO, COMMITTEE CHAIR
FRANKLIN R. AMTHOR
CHRISTINE A. CURCIO
LEI LIU
STEVEN J. PITTLER

A DISSERTATION

Submitted to the graduate faculty of The University of Alabama at Birmingham,
in partial fulfillment of the requirements for the degree of
Doctor of Philosophy

BIRMINGHAM, ALABAMA

2014

HIGH SPATIOTEMPORAL RESOLUTION MAPPING OF RETINAL PHYSIOLOGY

Qiuxiang Zhang

BIOMEDICAL ENGINEERING

ABSTRACT

The objective of my PhD dissertation research is to explore high resolution imaging of retinal function using transient intrinsic optical signals (IOSs) correlated with retinal physiological activation. The retina is responsible for capturing photons and preliminary visual information processing. Functional examination of retinal neural cells is important for eye disease detection and treatment evaluation. It is known that different diseases can target different retinal cell types, and thus high resolution imaging of retinal function is desirable. Fast IOSs with time courses comparable to retinal electroretinogram (ERG) kinetics can act as a unique biomarker to map physiological distortions correlated with eye diseases. In vitro IOS imaging of wild-type and mutant mouse retinas has revealed IOS distortions correlated with retinal diseases.

In order to achieve *in vivo* IOS imaging, a rapid line-scan confocal ophthalmoscope was constructed. Confocal IOS imaging of laser-injured frog eyes unambiguously detected localized (30 μm) functional lesions in the retina before morphological abnormality is detectable. Comparative IOS and ERG measurement revealed a close correlation between the observed optical response and retinal electrophysiological dynamics, particularly the ERG a-wave, which has been widely used to evaluate photoreceptor function.

To further uncover the anatomic source of fast IOSs in retinal photoreceptors, a functional spectral domain optical coherence tomography (SD-OCT) system was

constructed to provide depth-resolved IOS mapping at subcellular resolution. High spatiotemporal resolution OCT disclosed that fast IOSs was predominantly confined to the outer retina, particularly in the photoreceptor outer segment. Comparative study of dark- and light-adapted retinas demonstrated the feasibility of functional OCT mapping of rod and cone photoreceptors, with great potential for early disease detection and improved treatment evaluation of age-related macular degeneration (AMD) and other eye diseases that can cause photoreceptor damage. In addition to functional retinal imaging, we also applied the SD-OCT system for *in vivo* dynamic observation of light-driven melanosome translocation in RPE. Comparative OCT examination of dark- and light-adapted frog eyes verified that RPE melanosomes are the primary source of reflectivity in the RPE band. To the best of our knowledge, this is the first time demonstration of the feasibility of dynamic OCT monitoring of sub-cellular RPE translocation. Thus, SD-OCT is a versatile tool to assess posterior segment dynamics that may have relevance in the clinical setting.

Keywords: transient intrinsic optical signals, in vivo imaging, line-scan confocal, spectral domain optical coherence tomography, photoreceptor

ACKNOWLEDGEMENTS

First and foremost, I would like to express my sincere gratitude to my advisor, Dr. Xincheng Yao. He provided me with this great opportunity to work on projects which helped me to develop my skills in optical system development, experimental design and data analysis. What impressed me most was his encouragement when I made any progress and valuable advice and guidance when I was confused. Without him, this thesis would not have been completed or written.

I would like to thank Dr. Christine A. Curcio, Dr. Franklin R. Amthor, Dr. Lei Liu and Dr. Steven J. Pittler for being my committee members and imparting knowledge to me in their field of expertise.

I would like to thank my colleagues, Rongwen Lu and Benquan Wang who offered me their help when needed. They shared with me a lot of useful experience and knowledge during the time of study and research.

I would also like to thank Jerry H Millican for helping me make specimen-holding cambers and stages, Dr. Youwen Zhang for his technical support on in *vivo* ERG recording.

Finally, I would like to give special thanks to my whole family for always showing confidence in me and totally supporting me.

TABLE OF CONTENTS

LIST OF TABLES

LIST OF FIGURES

IN VIVO OPTICAL COHERENCE TOMOGRAPHY OF LIGHT-DRIVEN MELANOSOME TRANSLOCATION IN RETINAL PIGMENT EPITHELIUM

FUNCTIONAL OPTICAL COHERENCE TOMOGRAPHY ENABLES *IN VIVO* PHYSIOLOGICAL ASSESSMENT OF RETINAL ROD AND CONE PHOTORECEPTORS

LIST OF ABBREVIATIONS

AMD   Age-Related Macular Degeneration

AOSLO   Adaptive Optics Scanning Laser Ophthalmoscope

CCD   Charged-Coupled Device

DPSS   Diode-Pumped Solid State

ERG   Electroretinogram

FWHM   Full Width at Half Maximum

IOS   Intrinsic Optical Signal

LED   Light-Emitting Diode

NIR   Near Infrared

OCT   Optical Coherence Tomography

SLD   Superluminescent Laser Diode

SNR   Signal To Noise Ratio

TD-OCT   Time Domain Optical Coherence Tomography

SD-OCT   Spectral Domain Optical Coherence Tomography

INTRODUCTION

Visual processing begins in the retina. The retina is a light-sensitive tissue, lining the inner surface of the eye. It contains multiple layers with several layers of neurons interacting through synaptic connections. At the outermost retina layer are the photoreceptor cells. Light enters the eye, passes through several layers of neuron cells and reaches the outermost photoreceptor layer. Photoreceptor cells are light sensitive, captioning light and converting it to biochemical and electrical activities. Many eye diseases can produce functional defects of the retina[1, 2, 3]. In a routine eye examination, the fundus camera is used to image the fundus of the eye for retinal disease diagnosis or screening. However, by the time abnormal morphological changes are observed from fundus examination, irreversible damage of the retina may have occurred. Therefore, retinal functional measurement may be very useful for earlier detection of eye diseases, opening a greater window of opportunity for intervention.

Electrophysiological measurements, such as full field electroretinogram (ERG) [4] and relative multifocal ERG [5] are well established for objective evaluation of retinal neural dysfunction. However, signal specificities and resolution of these ERG measurements are relatively low because of the integral effect of the electrophysiological changes over the whole depth of the retina. For full field ERG, unless 20% or more of the retina is affected by a diseased state, ERGs are usually normal. Low signal specificity and limited spatial resolution of ERG measurements make it difficult to identify localized retinal neural dysfunctions. Multifocal ERG measures electrical activities from more than

a hundred retinal areas per eye. Therefore, multifocal ERG can, to some extent, improve the spatial resolution or sensitivity for disease diagnosis. However, multifocal ERG measurement is time-consuming and the results may be too complex to interpret. In ophthalmology, visual field testing (perimetry) is regarded as the gold standard for detecting and monitoring the progression of retinal diseases, such as glaucoma. However, the sensitivity and specificity of perimetry are also poor due to its requirement of unattainable levels of patient cooperation. Investigators have found that unless over 50% of ganglion cells were lost, the functional test with perimetry is still normal [6]. Therefore, further development of high spatial resolution imaging technology is essential for early detection of functional disorders in the retina. Intrinsic optical signal (IOS) imaging of the retina holds promise as a high spatial resolution method for concurrent retinal morphological and functional measurements.

IOSs are generated in excitable biological tissue and featured by transient changes of light properties (e.g. light intensities or polarization). Early research found that light scattering and birefringence could be used to detect rapid structural changes accompanying the action potentials in the nerve fibers [7]. In other words, when the neurons in some tissues are activated or stimulated, they will undergo some microstructural or metabolic changes which induce dynamic changes of light properties, such as the light intensity, phase and polarization state. When we use detectors, such as a photodiode array or a charge-coupled device (CCD) to collect the light that is reflected from or transmitted through the living tissue before and after they are activated, the detected light (optical signal) carries the information of physiological function of stimulated neurons. The transient changes of light properties are "intrinsic", resulting

from the endogenous biological properties of the excitable tissue.

Background

IOS imaging has been widely explored in studying the functional cortical activities, such as the visual cortex. The functional organization of the various areas of the visual cortex[8], such as V1[9 10], V2[11], V4[12], MT[13], and TE[14] have been studied by this technique in the past decade. However, IOS imaging of cortical activities requires surgical exposure of the cortical surface and intense effort has to be made as to view the cortex clearly, hampering the clinical application of IOS imaging in brain function examination. IOS imaging of the retina shows greater promise to achieve clinical application. Because of the transparent ocular media in the eyeball, the retina can be easily accessed *in vivo* by optical systems. Without any surgical invasion, the light reflectance changes from the retina can be clearly and stably monitored.

The sources of IOSs are not fully understood because there are many changes occurring that affect neural activation. The origins might be originated from multiple metabolic changes including the oxygenation state of hemoglobin and blood vessel volume as well as microscopic morphologic changes, such as cell swelling and shrinking that will alter light-scattering properties[7]. Illumination/observation light with specific wavelengths or spatiotemporal resolutions might be applied to differentiate different IOS mechanisms. For example, IOSs measured at 540 nm illumination light are dominated by blood volume changes in capillaries. At 600 to 650 nm, they are dominated by changes in the deoxygenation level of hemoglobin. In other words, IOSs observed with visible light are mainly correlated with metabolic changes. They are usually slow signals and reach

peak around five to six seconds[8]. For IOS imaging in the retina, visible light is usually used to stimulate the retina, while near infrared (NIR) light is used to illuminate the retina, because NIR light is less absorbed by ocular components and it is beyond the absorption spectra of photopigments. At near-infrared wavelengths both oxyhemoglobin and deoxygenated hemoglobin have negligible absorbance and IOSs are dominated by light-scattering changes induced by microscopic morphologic changes[8]. It is believed that the light-scattering changes are more directly correlated with neural activities and IOSs derived from light-scattering changes are usually fast signals with onset times within 10 ms and peak times within 1 s [15, 16, 17]. Therefore, the high temporal resolution is indispensable for fast IOS recording. In addition, IOS images with high spatial resolution disclose signals with different polarities, i.e. both positive (increase) and negative (decrease) signals that are mixed together within a small area [18]. Previous studies with isolated photoreceptor outer segments and isolated retinas have demonstrated fast IOSs associated with phototransduction[19, 20, 21]. Both binding and releasing of G-proteins to photoexcited rhodopsin might contribute to the positive and negative IOSs[20]. Localized biochemical processes might produce non-homogeneous light intensity changes, i.e. spatially mixed positive and negative signals. In addition to these biochemical mechanisms, physical changes, such as stimulus-evoked cell volume changes associated with water influx due to ionic currents through gated membrane channels might also contribute to the IOS response [7, 22, 23, 24].

IOS imaging of the retina has been studied extensively over the past few years with different imaging modalities. The fundus camera that is typically used to visualize the posterior surface of the retina evaluation was modified to detect IOSs from the cat [25,

[26, 27, 28, 29, 30], monkey [31, 32, 33, 34, 35] as well as human retinas[36]. The fundus image provides a large field of view of the retina but the spatiotemporal resolution is relative low. The spatial resolution is around 50 μm in the transverse direction making it difficult to detect subtle structures. The temporal resolution of the fundus camera is typically on the second scale, which is to slow to track fast neuron activation. Adaptive optics scanning laser ophthalmoscope (AOSLO) has a high lateral resolution that can image the photoreceptor mosaic *in vivo* from human retina. However, the axial resolution of the AOSLO is low (150 μm). When it was used to record IOSs, the signals from photoreceptors may be contaminated by the activities of neurons from inner layers of the retina [37]. An optical coherence tomography (OCT) imaging system with high axial resolution can provide cross-sectional images of the retina for IOS imaging [38, 39, 40, 41, 42, 43, 44, 45, 46]. Therefore, IOSs can be detected simultaneously from multiple retinal layers using this imaging technique. However, the signal to noise ratio (SNR) is low compared with other imaging modalities such as the fundus camera and AOSLO. Robust and reliable IOS recording is highly dependent on system design and advanced signal extraction processing method. Our lab focuses on the IOS imaging of the retina. A lot of previous studies have been conducted to investigate the IOS characteristics or signal sources from isolated frog retinas [47, 48, 49, 50, 51, 52, 53, 54, 55, 56, 57]. The primary aim of my Ph.D.'s dissertation research was to design and develop optical systems for *in vivo* IOS recording from spatially distinct regions of the retina.

Specific Aims of this Dissertation Research

The purpose of my Ph.D. dissertation research is to pave the way towards clinical

application of IOS imaging for early retinal eye disease detection. My effort focuses on exploring the optical system design and signal post-processing method for reliable *in vivo* detection of fast IOSs.

Specific Aim 1: To develop a rapid line-scan confocal ophthalmoscope for *in vivo* IOS imaging at sub-cellular resolution in the lateral direction. In order to investigate the physiological mechanism of confocal IOS, comparative IOS and ERG measurements were conducted using normal frog eyes activated by variable intensity stimuli.

Specific Aim 2: To develop of a high performance SD-OCT for fast IOS recording and dynamic melanosome translocation monitoring in the retinal pigment epithelium (RPE).

Specific Aim 3: To compare IOSs between wild-type and mutant animals to demonstrate the clinical potential of the proposed technology. All of the previous studies on IOS imaging attempted to record IOSs for investigating the signal properties or identifying the signal sources from healthy retina. The ultimate goal of our research is to realize clinical application of IOS imaging for early retina disease diagnosis, therefore, it is essential to demonstrate the feasibility of using IOS imaging to differentiate normal and diseased retina.

Significance and Innovation

In vitro physiology and histology are traditional methods for studying retinal structure and function. Compared with isolated retina, *in vivo* IOS imaging allows for longitudinal studies from the same specimen, which can, to some extent, improve experimental reproducibility. Moreover, under *in vivo* conditions, the retina does not

require extra complex nutrition supply systems to ensure the viability of retinal cells. In addition, *in vivo* IOS imaging of animal models is a prerequisite step towards clinical application of IOSs for human retinal functional assessment.

To realize *in vivo* fast IOSs recording, a rapid line-scan confocal imager and SD-OCT system were developed. Both systems were featured by their high spatial and temporal resolutions. High temporal resolution is essential for recording neural activity related fast IOSs[15]. As retinal diseases usually progress gradually and target different retinal cells at different disease stages, high spatial resolution is therefore important for early and accurate eye disease assessment.

We used a green laser diode with adjustable power to reach more uniform stimulation at the retina. In addition, localized stimulation pattern were easily generated. IOS imaging of normal or healthy retina with a localized stimulation pattern produced natural control and experimental areas to verify the signal reliability. For IOS imaging of abnormal or diseased retina, localized retinal response detection can realized retinal disease diagnosis at a specific local area.

The low SNR has been the most significant obstacle in IOS imaging of the human retina[36, 41, 42, 58]. Because IOSs are obtained by comparing the observation light intensity changes before or after stimulation at the same area, ocular movement, heartbeat, breathing or blood flow might severely contaminate IOSs. Using our custom-designed optical system in conjunction with our advanced signal extraction methods, reliable IOSs with unprecedented SNR were obtained *in vivo* from the retina of an anesthetized frog. Heartbeat, breathing or blood flows complications remain that cannot be ignored in our *in vivo* IOS imaging. To address these issues, we developed advanced post-acquisition

image registration and adaptive IOS processing algorithms, which may also be applicable for IOS extraction in a clinical setting.

<div align="center">Line-scan Confocal Ophthalmoscope</div>

System Design and Development

To achieve *in vivo* localized fast IOS imaging with sub-cellular resolution in the lateral direction, we designed and developed a line-scan confocal ophthalmoscope. The schematic diagram of the system is showed in Fig. 1. It consists of two light sources: a NIR light for IOS recording, and a visible green light for retinal stimulation. The NIR light is produced by superluminescent laser diode (SLD) with center wavelength of 830 nm. The NIR light is less absorbed before it reaches the retina. The SLD has an additional advantage of having the high power of laser diodes (LD) and the low coherence of conventional LED. In other words, SLD has higher power than LED and has better SNR than LD. One unique component of THE line-scan confocal system is the cylindrical lens, which condenses the NIR recording light into one single line rather than a point. Therefore, the light illumination patterns are different when observed from the top (Fig. 1A) and from that observed from the side (Fig. 1B). Lens *L*1 and lens *L*2 work as the relay lenses for extending the system. The focal lengths of lenses *L*1, *L*2, *L*3, *L*4 and *L*5 are 80, 80, 25, 160 and 40 mm, respectively. Lenses *L*1, *L*2, *L*3 and *L*4 are achromatic doublets for minimizing the chromatic aberration. The optical magnification, *M*, of the line-scan confocal system can be calculated as follows:

$$M = \frac{f_{L3}}{f_{eye}} * \frac{f_{L4}}{f_{L2}} \tag{1}$$

where f_{L3} is the focal length of lens *L*3, f_{eye} is the focal length of the frog eye (2.87

mm[59]), f_{L2} is the focal length of lens L2 and f_{L4} is the focal length of lens L4. Thus, the calculated optical magnification is around 17.4.

Another unique component for line-scan confocal system is the linear CCD camera which detects the reflected light in a thin line rather than a point. The linear CCD camera (EV71YEM2CL1014-BA0, E2V, NY, USA) used in the system is equipped with a camera link interface, which greatly facilitated system control and data synchronization. For this camera, each CCD pixel size is 14 μm x 14 μm. Therefore, for each CCD pixel, the corresponding lateral size Δx in the retina is 0.8 μm (14 μm/ 17.4 magnifications). The image field of view in the lateral direction FOV_x is dependent on the light beam size d after the collimator as well as the focal lengths of lenses L1, L2, L3 and the frog eye (Fig. 1B).

$$FOV_x = d * \frac{f_{L2}}{f_{L1}} * \frac{f_{eye}}{f_{L3}} \tag{2}$$

where d is 2.5 mm after the collimator. Thus, the calculated FOV_x is around 287 μm.

For each CCD pixel, the corresponding lateral size Δy in the retina can be calculated as follows:

$$\Delta y = \frac{FOV_y}{N_{lines}} = \theta_{OA} * f_{L2} * \frac{f_{eye}}{f_{L3}} * \frac{1}{N_{lines}} \tag{3}$$

where FOV_y is the image field of view in the vertical direction, θ_{OA} is the optical angle of the scanner in radians, which is twice the size of the mechanical angle θ_{MA} of the scanner. N_{lines} is the number of scan lines. The scanner is a scanning galvo mirror (VA100, Thorlabs, NJ, USA) and the ratio between the input voltage and mechanical angle was set to be 0.5 v/degree. Therefore, to ensure Δy equals to Δx, there is a relationship between input voltage V and the number of scan lines N_{lines}.

$$N_{lines} = \frac{V}{0.5} * 2 * \frac{\pi}{180} * f_{L2} * \frac{f_{eye}}{f_{L3}} * \frac{1}{\Delta y} \qquad (4)$$

i.e.

$$V = N_{lines} * 0.5 * \frac{1}{2} * \frac{180}{\pi} * \frac{1}{f_{L2}} * \frac{f_{L3}}{f_{eye}} * \Delta y \qquad (5)$$

Therefore, if the number of scan lines, N_{lines} is set to 100, then the input voltage should be around 0.125 volts, the corresponding field of view in the vertical direction FOV_y is around 80 μm ($\Delta y * N_{lines}$).

The photo of the constructed system is showed in Fig. 2A. A single-mode fiber coupled 532-nm DPSS (diode-pumped solid state) laser module was used to produce the visible light for stimulating the retina locally or inducing a local lesion in the retina. It could provide adjustable output power from 0 to 20 mW at the fiber end. A mechanical slit was placed behind the collimated green stimulus light to produce a rectangular pattern (Fig. 2B) and to provide precise adjustment of stimulus width. A customized program (Labview 2011) was developed for real time image display, high speed image acquisition and signal synchronization. Before each IOS recording, the stimulus location in the field of view and the stimulus timing was tested to be highly repeatable and accurate.

SD-OCT

OCT is an established imaging technology for performing noninvasive, high-resolution cross-sectional imaging by measuring backscattered or back reflected light. When using OCT for retinal imaging, we can differentiate retinal layers as well as measure retinal thickness[60, 61, 62, 63, 64]. We can also use OCT for dynamic retinal functional measurement[38, 39, 40, 41, 42, 43, 44, 45, 46]. Ultrahigh resolution time domain OCT

(TD-OCT) and SD-OCT were previously used to detect local stimulus-evoked scattering changes both *in vitro* and *in vivo* [40, 42, 65]. Compared with TD-OCT, SD-OCT is featured by its high imaging speed, increased axial resolution without any deterioration of signal to noise ratio[66, 67], which greatly extends the application of this technique in both scientific research and clinical practice[66, 68, 69, 70, 71]. The high performance SD-OCT can not only provide structural information such as the thickness of the never fiber layer for retina disease diagnosis but also provide a useful and effective way to simultaneously perform functional measurement of multiple retinal layers' optical responses.

Interpretation of OCT Signals

OCT is akin to ultrasonic imaging, except that it uses light instead of sound. Acoustic impedance is the acoustic analog of the refractive index. As in ultrasonic imaging, where the proportion of the ultrasound pulse reflected back toward the transducer is dependent on the difference in acoustic impedance between two structures, OCT signals are mainly related with the refractive index within the interface of tissues. Theoretical and empirical studies on multilayered model systems have demonstrated that refractive index changes and scattering contribute to the OCT signals in the retinal image. Refractive index changes define the peak of reflected light and scattering properties give rise to the band thickness[72]. The more the light is scattered, the thinner the outer border. One possible reason for this may be the loss of coherence by the multiple scattering, resulting less light being returned to the detector.

In a conventional SD-OCT system as showed in Fig. 3, light from a low-coherence source (broadband SLD) is directed into a 2 × 2 fiber coupler that splits light

into the sample and reference arms. Light exiting the reference fiber usually goes through a dispersion compensation unit and arrives at a mirror surface where it is redirected back into the same fiber. Light exiting the sample fiber is guided to a scanning system and relayed by a pair of lenses to the eye, where a light beam is focused at the retina. The light that is backscattered or reflected from the retina is redirected back and interferes with the returning reference arm light in the fiber coupler, by which the combined light is delivered to a spectrometer. The spectrometer is the key component in the SD-OCT system which separates and detects the inference signals to multiple wavelength channels.

During imaging, the reference arm is fixed. The frequency of the interferometric fringes as a function of the source spectrum represents the optical path length difference between sample and reference reflections, i.e. the axial location of the tissue illuminated, with higher frequency oscillation corresponding to larger optical path length mismatches or usually deeper of the tissue location. Fourier transform is the mathematical tool used for extracting the frequency content of a signal. However, the true Fourier transform pair of distance is not wavelength (also units of distance), but in fact wavenumber (with units of inverse distance).

Design and Construction of the Spectrometer

The spectrometer design contains four main components: a collimator, a spectrally dispersive element, a focusing lens, and a detector array. The design of each component can have a dramatic effect on overall system performance. The axial resolution, imaging range and sensitivity fall-off are all dependent on the spectrometer's design.

Detector array. In SD-OCT, the array detector in the spectrometer has a bandwidth or spectral range limit, $\Delta\Lambda$. The detector used in our SD-OCT system is a linear CCD camera (EV71YEM4CL2014-BA9 OCT/Spectrometer versions, E2V, NY, USA) with 2048 pixels and 14 μm x 28 μm pixel sizes. The full width at half maximum (FWHM) of the light source is 104 nm (spanning from 794.3 nm to 898.3 nm). The full available spectrum is recorded by the CCD camera to approach theoretical axial resolution (3.04 μm) and to maximize the imaging range[61]. The light source spectrum covers the wavelength ranging from 764 nm to 928 nm and the resulting theoretical spectrum resolution is about 0.08 nm.

Grating. Most gratings are first order gratings since they are efficient with $m = 1$, the spectral resolution of a grating, depends upon the density of the grooves as well as the beam diameter incident on the grating. Groove density of 1200 mm^{-1} is usually selected because it is the highest density of the grating grooves that can be easily manufactured. To achieve δλ ≤ 0.08 nm with $m = 1$, groove density of 1200 mm^{-1} and maximum light wavelength of 928 nm, the beam diameter incident on the grating must be greater than 9.67 mm.

$$\frac{\lambda_{max}}{\delta\lambda} = mGD \qquad (6)$$

where m, the order of diffraction in the grating, λ_{max}, the maximum wavelength of the light source, G is the groove density and D is the beam diameter incident on the grating.

The SD-OCT system is a fiber-based setup and the light beam emanating from the fiber end will have a Gaussian profile. For a Gaussian beam, 9.67 mm is the diameter of the beam where the amplitude has dropped to 1/2 of the maximum, thus the actual aperture size of the grating should be greater to minimize beam clipping. To collect out to

1% of the maximum, the grating aperture must be at least 24.9 mm in diameter. Besides, the grating should be chosen with relative high efficiency for the light source wavelength range. According to grating equation, different wavelengths are diffracted at different angles given by:

$$(sin\alpha + sin\beta) = mG\lambda \qquad (7)$$

where α is the incident angle and β is the diffracted angle.

Therefore, transmission grating with the effective response wavelength range near the one of our system, groove density of 1200 mm^{-1} and clear aperture diameter greater than 25 mm will be applied in the system.

The specific incident angle will be determined to ensure high efficiency of the grating. The optimal efficiency for center wavelength λ_0 (846 nm) occurs at α of 30.5°. Using α = 30.5°, the angular dispersion for 764 nm to 928 nm can be determined using the grating equation (Eq.6). The spectrum from 764 nm to 928 nm disperses approximately from 24.16° to 37.31°, resulting in angular spread $\Delta\beta$ of 13.15°.

Focusing lens. The focusing lens focuses the spectrally dispersed light from the grating onto linear CCD array. The spectrum ranges from 764 nm to 928 nm, dispersed from 24.16° to 37.31° needs to be imaged onto the 28.672 mm array in the camera. The angular spread $\Delta\beta$ and the length of CCD array L determine the focal length of the focusing lens to be around 125 mm (Eq. 8). Besides, the clear aperture for the focusing lens should at least more than 30 mm.

$$f_{focus} = \frac{L}{2*tan(\Delta\beta)} \qquad (8)$$

System Parameters

Axial resolution. It is well established that axial and lateral resolution are decoupled in SD-OCT. Axial resolution is determined by the bandwidth of the light source. A broadband superluminescent diode with a center wavelength of 846 nm, spanning from 780 nm to 912 nm and FWHM of 104 nm was used as the light source in this system. According to Eq.9[73], the theoretical axial resolution is about 3 μm. However, because the shape of the spectrum is not perfectly Gaussian, the effective axial resolution is less than this optimum value.

$$\Delta z = \frac{2\ln(2)\lambda_0^2}{\pi\Delta\lambda} \tag{9}$$

Lateral resolution. Lateral resolution is determined by the beam spot size on the retina which relates to the numerical aperture and aberrations of the ocular refractive media (Eq.10[74]). Commercial human retinal OCT instruments typically use beam diameters of the order of ~ 1 mm, limiting the lateral resolution to ~ 20 μm. For the frog eye, due to its short focal length (2.87 mm) and large pupil size (5 mm), the light entering the pupil with beam diameter of 2 mm can achieve high lateral resolution around 1.5 μm. However, the actual lateral resolution will be severely degraded by the aberrations.

$$\Delta x = \frac{4\lambda_0 f_{obj}}{\pi d_{spot}} \tag{10}$$

where Δx is the lateral resolution, λ_0 is the center wavelength of the light source spectrum, f_{obj} is the focal length of the objective (frog eye) and d_{spot} is the beam spot size on the frog pupil. The actual lateral resolution we can achieve is around 3 μm.

Temporal resolution. A fast linear CCD camera with line rate up to 36 kHz was used in the imaging system. The camera is equipped with a camera link interface, which will greatly facilitate system control and data synchronization. An image acquisition board acquires the image captured by the camera and transfers it to a computer workstation for signal processing and image display. During IOS imaging with the constructed SD-OCT system, the A-line (depth scan) rate of the OCT system is set at 20 kHz for 100 Hz frame rate and 32 kHz for 500 Hz frame rate.

Imaging depth. According to the relation between Fourier transform of spectrum and optical path length[61] and based on Nyquist criteria, the maximum measurable depth is 1.14 mm in the retina if the effect of scattering or absorption in biological samples is excluded (Eq.11[73]).

$$Z_{max} = \frac{\Delta z}{2n}\frac{N}{2} = \frac{\ln 2}{2\pi n}\frac{\lambda_0^2}{\Delta\lambda} N \tag{11}$$

where Z_{max} is the maximum measurable depth, Δz is the axial resolution, *n* is the refractive index of the tissue, assuming 1.36 for the eye, *N* is the number of pixels of CCD arrays.
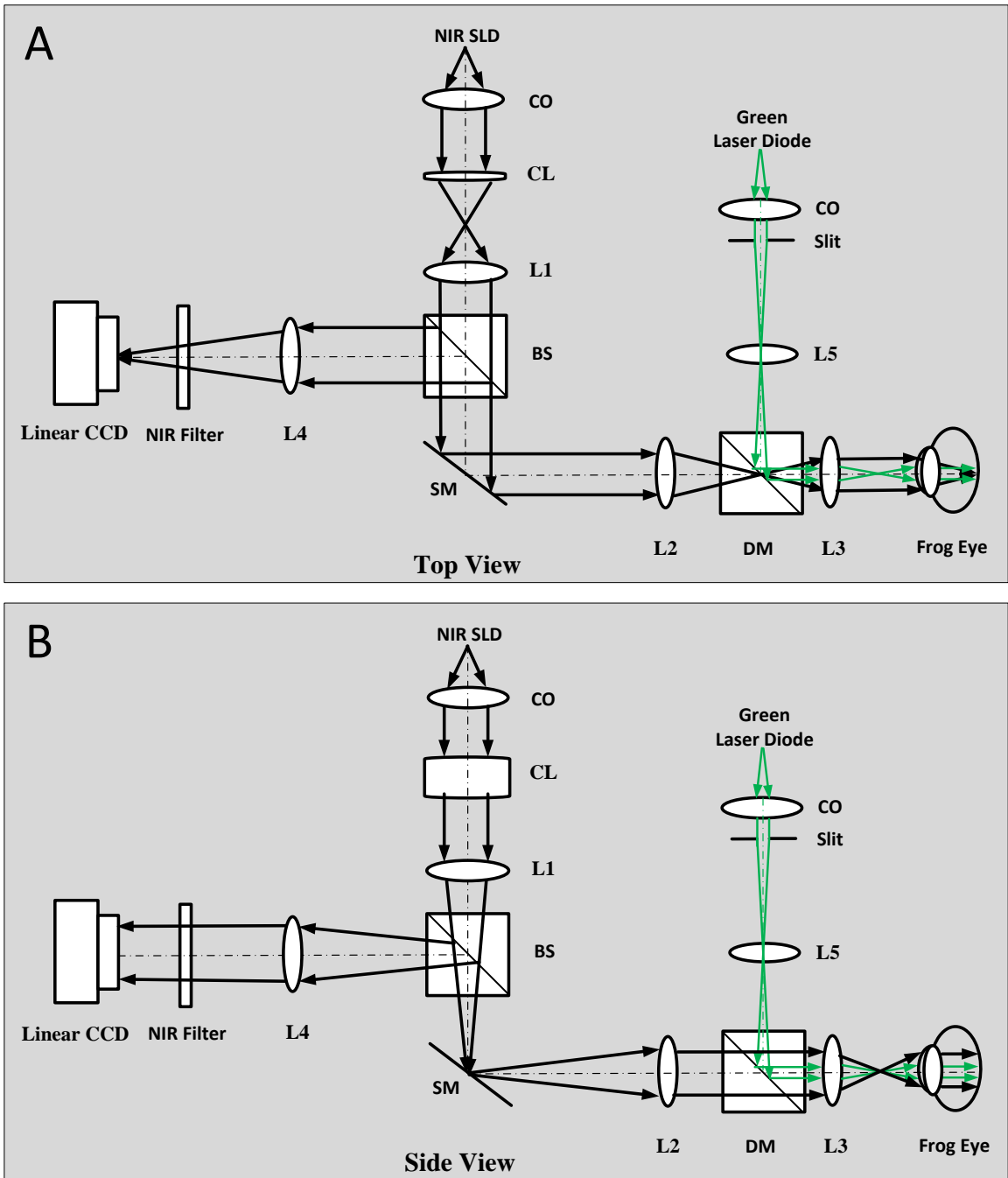
Figure 1. Schematic diagram of the line-scan confocal ophthalmoscope for *in vivo* IOS imaging of frog eye. Both top view (A) and side view (B) light paths are included. SLD, superluminescent laser diode; CO, collimator; CL, cylindrical lens; BS, beam splitter; SM, scanning mirror; DM, dichroic mirror; MS, mechanical slits; Lx, optical lenses.
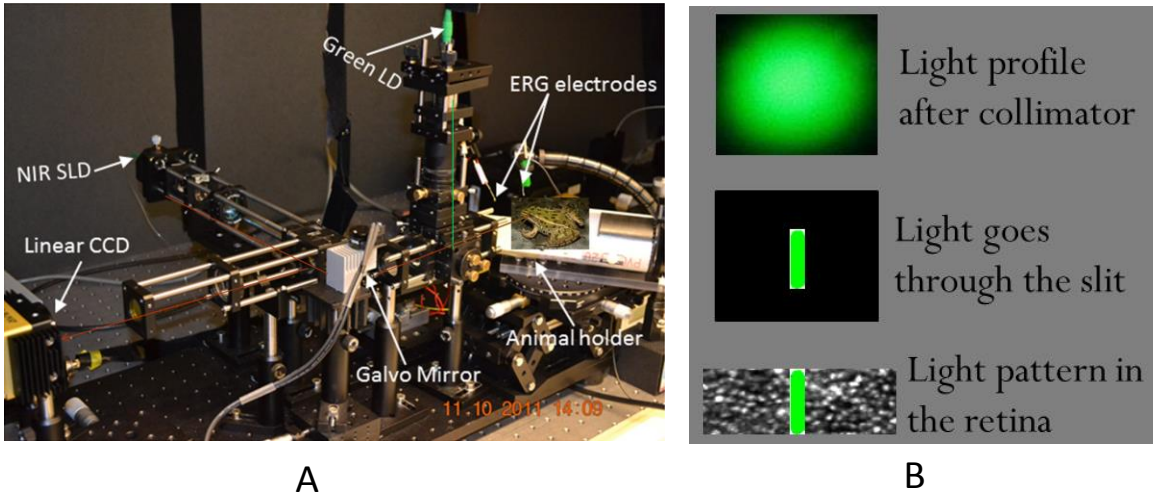
Figure 2. The line-scan confocal ophthalmoscope and stimulation pattern demonstration. (A) Some components of the ophthalmoscope, such as NIR SLD, green LD, ERG electrodes, linear CCD, galvo mirror and animal holder are indicated in the photo. (B) Light from the green laser diode is collimated and then passes through the slit to produce a rectangular pattern. The relative size and position of the stimulation pattern in the retina is also showed.
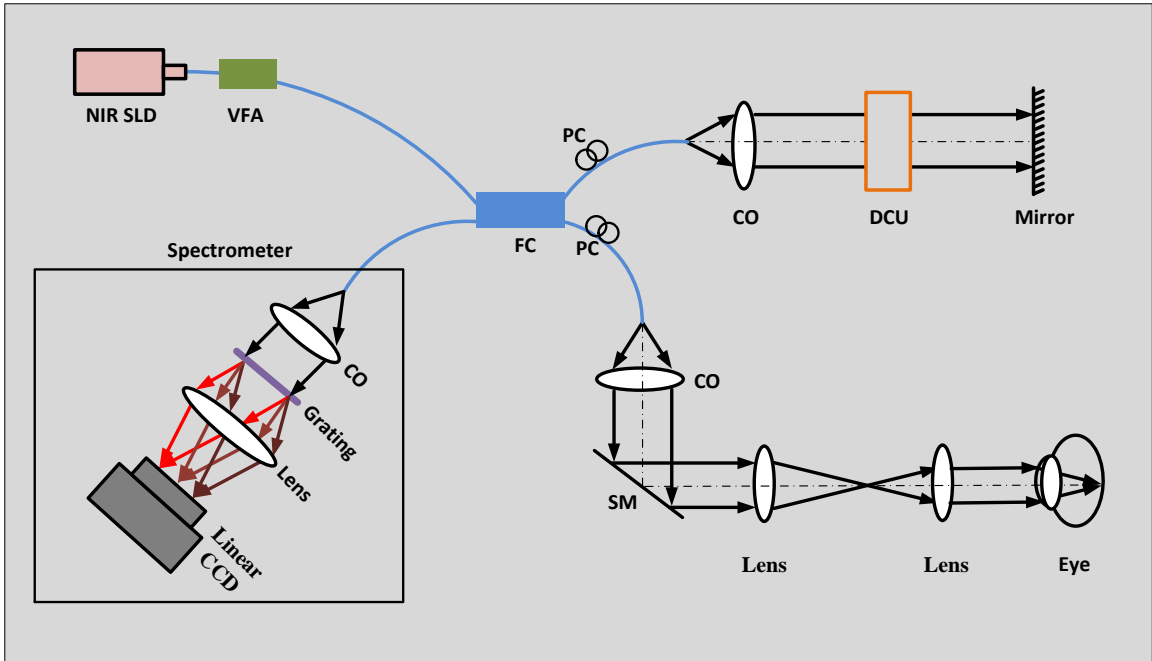
Figure 3. Schematic diagram of SD-OCT for *in vivo* retinal imaging. SLD, superluminescent laser diode; VFA, variable fiber attenuator; FC, fiber coupler; PC, polarization controller ; CO, collimator; DCU, dispersion compensation unit; SM, scanning mirror.

COMPARATIVE INTRINSIC OPTICAL SIGNAL IMAGING OF WILD-TYPE AND
MUTANT MOUSE RETINAS

by

QIUXIANG ZHANG, YOUWEN ZHANG, RONGWEN LU, YICHAO LI, STEVEN J.

PITTLER, TIMOTHY W. KRAFT AND XINCHENG YAO

Abstract

Functional measurement is important for retinal study and disease diagnosis. Transient intrinsic optical signal (IOS) response, tightly correlated with functional stimulation, has been previously detected in normal retinas. In this paper, comparative IOS imaging of wild-type (WT) and rod-degenerated mutant mouse retinas is reported. Both 2-month and 1-year-old mice were measured. In 2-month-old mutant mice, time course and peak value of the stimulus-evoked IOS were significantly delayed (relative to stimulus onset) and reduced, respectively, compared to age matched WT mice. In 1-year-old mutant mice, stimulus-evoked IOS was totally absent. However, enhanced spontaneous IOS responses, which might reflect inner neural remodeling in diseased retina, were observed in both 2-month and 1-year-old mutant retinas. Our experiments demonstrate the potential of using IOS imaging for noninvasive and high resolution identification of disease-associated retinal dysfunctions. Moreover, high spatiotemporal resolution IOS imaging may also lead to advanced understanding of disease-associated neural remodeling in the retina.

1. Introduction

Functional measurement is important for retinal study and diagnosis. Many eye diseases, such as age-related macular degeneration (AMD) [1], retinitis pigmentosa (RP) [2], diabetic retinopathy (DR) [3], and others, produce functional defects in the outer and/or inner retina. Morphological mapping of disease-associated structural abnormalities in the retina can provide valuable information for disease detection. In coordination with adaptive optics (AO) and optical coherence tomography (OCT), cellular resolution of

retinal fundus imaging has been achieved. However, disease-associated morphological and functional changes are not always correlated directly, in terms of time course and spatial location. Therefore, objective assessment of retinal function is essential. Electrophysiological measurements, such as full field electroretinogram (ERG) [4] and relative multifocal ERG [5] are well established for objective evaluation of neural retinal dysfunction. However, signal specificities and resolution of these ERG measurements are relatively low because of the integral effect of the electrophysiological changes over the whole depth of the retina.

Transient changes of intrinsic light properties (e.g., scattering, absorption, and polarization) in activated excitable cells can be used for functional imaging of living systems. Stimulus-evoked intrinsic optical signal (IOS) has been detected in nerve tissues [6–8], endocrine cells [9], and in the retina. IOS imaging may provide a noninvasive and high resolution method to evaluate functional integrity of the retina. Stimulus-evoked IOSs have been detected in isolated retinal tissues [10–15], intact animals [16, 17], and human subjects [18, 19]. Recently, IOS alterations were explored in vivo by OCT imaging of photoreceptors of patients with inherited retinal diseases [20]. The purpose of this study is to quantitatively compare temporal and spatial characteristics of IOS changes in normal and mutant retinas, and therefore to demonstrate the feasibility of using IOS imaging for high resolution identification of disease-associated retinal dysfunction.

A Cngb1 knockout mouse model (Mus musculus) that does not express the β-subunit of the cGMP-gated cation channel and the related GARP proteins was employed for this study [21]. Rod function is attenuated but detectable up to 6 months. By 1 year of age the ERG response is no longer detectable and all rod cells have degenerated. In this

paper, time courses and peak value of the IOS in normal and Cngb1 retinas are quantitatively compared. Our experiments indicated that IOS onset-time and time-to-peak (relative to stimulus onset) of mutant mice were significantly delayed compared to wild-type (WT) mice. In addition, dynamic IOS background images, i.e., without retinal stimulation, revealed spontaneous activity-associated spatiotemporal patterns in the knockout mouse retina, while the WT mice had a relatively clean background.

2. Method

2.1. System Setup

Figure 1 illustrates the schematic diagram of the experimental setup. Details of the optical imaging system have been reported in previous publications [14, 22]. Equipped with a high-speed CMOS camera (PCO1200, PCO AG, Kelheim, Germany), the imaging system provided millisecond temporal resolution and sub-cellular spatial resolution for dynamic monitoring of stimulus-evoked fast IOSs. As shown in Fig. 1, the imaging system consisted of two light sources: a near infrared (NIR) light for IOS recording, and a visible white light for retinal stimulation. The visible light produced by a fiber-coupled white light emitting diode (LED) was collimated to improve stimulation uniformity. A slit was placed behind the collimator to provide a rectangular stimulus of 80 μm x 180 μm. The NIR light produced by a 12-V 100-W halogen lamp (PHILIPS7724) was filtered by a band-pass filter (wavelength band: 800-1000 nm). The NIR filter, in front of the CMOS camera, was a long-pass filter which blocked visible stimulus light and transmitted NIR light that was detected. During the IOS recording, the retina was continuously illuminated by ~1 mW NIR light illumination. In each trial, pre-stimulus

recording was 0.4 s, followed by a 10 ms visible light flash and 1.0 s post-stimulus recording. The raw images were captured at the frame rate of 1000 frames per second with image size of 400 x 300 pixels (240 μm x 180 μm).

2.2. Mice strains, handling and genotyping

Knockout mice (Mus musculus) were generated as previously described [21] and maintained by homozygous crosses. Knockout mice originated in a 129 Sv background crossed into a C57Bl/6 background and were bred congenic (> 10 generations) prior to initiation of this study. Genotypes were verified as previously described [21] using standard PCR technology. WT mice were originally obtained from crosses of heterozygous knockout mice and maintained on a C57Bl/6 background. WT mice were verified by PCR [21] to be absent for the knockout allele. Mice were handled in accordance with university animal resources program guidelines and according to the ARVO "Statement for the Use of Animals in Ophthalmic and Visual Research". Mice were maintained on standard chow and water ad libitum and on a 12 on /12 off light cycle with overall light exposure limited to less than 300 lux.

2.3 Sample preparation

Isolated WT and Cngb1 knockout mutant mouse retinas [21] (without retinal pigment epithelium) were used to test stimulus-evoked IOS responses. Without the complications of hemodynamic changes and eye movements, isolated retina is a simple preparation to verify the differences produced by retinal neuronal cells. The experiments were performed following the protocols approved by the Institutional Animal Care and Use Committee of University of Alabama at Birmingham. Briefly, retinal dissection was

conducted in a dark room with dim red illumination. After overnight dark adaptation, eyeballs from anesthetized mice were rapidly enucleated and the retina was carefully isolated from the eyeball in Ames media, and then transferred to a recording chamber under a nylon grid mesh for IOS imaging. During the experiment, the sample was continuously super-fused (~2 ml/min) with oxygenated bicarbonate-buffered Ames medium, maintained at pH 7.4 and 33~37°C.

2.4 Data Processing

IOS images shown in Figs. 2(b-d) are presented in the unit of ΔI/I, where ΔI/ is transient optical change and I is reference baseline. Dynamic differential data processing was employed to construct the IOS images [22]:

$$IOS_{t_i}(x,y) = \frac{\Delta I}{I} = \frac{I_{t_i}(x,y) - \frac{1}{m}\sum_{j=1}^{j=m} I_{t_{i-j}}(x,y)}{\frac{1}{m}\sum_{j=1}^{j=m} I_{t_{i-j}}(x,y)} \tag{1}$$

where $I_{t_i}(x,y)$ was the intensity at the time point of t_i, and i=1,2,3, … represented the image index. m was the number of images before the image i. In other words, the dynamic reference baseline of the pixel at (x, y) was calculated by using the averaged pixel value of m consecutive frames recorded before the time point t_i. In this article, we selected m=100 (i.e., images recorded over 100 ms).

Since the recording light intensities could increase or decrease upon stimulus, to better categorize the changes and identify signal from noise, we quantified pixel numbers of positive and negative signals as the following: the signal at pixel (*x, y*) is defined as positive, if

$$IOS_{t_i}(x, y) > \overline{IOS}(x, y) + 3\sigma(x, y) \tag{2-a}$$

Likewise, it is negative, if

$$IOS_{t_i}(x, y) < \overline{IOS}(x, y) - 3\sigma(x, y) \tag{2-b}$$

where

$$\overline{IOS}(x, y) = \frac{1}{n} \sum_{j=1}^{j=n} IOS_{t_j}(x, y) \tag{3}$$

$$\sigma(x, y) = \sqrt{\frac{1}{n} \sum_{j=1}^{j=n} \left(IOS_{t_j}(x, y) - \overline{IOS}(x, y) \right)^2} \tag{4}$$

where n is the pre-stimulus image number. For each dynamic differential IOS image, given the position of x_0, we counted the positive/negative pixel numbers along the y axis. In this way, we converted the 2-dimensional IOS image to a single line (one dimension). The value of each pixel in the line indicated the pixel numbers with positive /negative signals along the y axis (300 pixels). By combining such lines over time, we reconstructed the *x-t* spatiotemporal images (Fig. 3(a)).

There were spontaneous activities or granular patterns observed from IOS background images. Coefficient of variation (*CV*) [23] was used to quantify and represent the spontaneous activities:

$$CV(x, y) = \frac{\sigma(x, y)}{\overline{IOS}(x, y)} \tag{5}$$

Here, we call the array of CV as the texture image. For each trial, we had a texture image, and correspondingly, a quantitative approach was used to measure the uniformity and smoothness of the texture image [24]. The uniformity is defined as:

$$U = \sum_{k=0}^{k=L-1} H^2(CV) \tag{6}$$

26

where *H(CV)* is the histogram of the texture image, and *L* is the number of histogram bins. And the smoothness is defined as:

$$S = 1 - \left(\frac{1}{1 + \delta_{CV}^2} \right) \tag{7}$$

where δ_{CV}^2 denotes the variance over the whole texture image.

3. Results

3.1. Stimulus-evoked IOS comparison between WT and mutant mouse retinas

Figure 2 shows a dynamic differential IOS comparison between WT and Cngb1 mouse retinas activated by a single flash. Each image (400 x 300 pixels) is an average over 200 images. Fig. 2(a) shows a representative mouse retina image sequence. For each trial, pre-stimulus baseline recording was collected for 0.4 s (i.e., 200 frames) before a 10 ms visible white light stimulus was delivered. The black arrowhead (Fig. 2(a)) indicates the onset of stimulus. Fig. 2(b) shows IOS images of 2- month-old WT mouse retina. Upon the stimulus, IOS image revealed a robust and rectangular pattern spread out over the stimulus activated region (Fig.2 (b)). Under the same experimental conditions, IOS images of 2-month-old rod degenerated mouse retina also showed a regular rectangular pattern, however, due to ongoing retinal degeneration [21], signal strength was greatly attenuated (Fig. 2(c)). In 1-year-old mutant mice, visible light stimulus evoked optical signals were no longer detectable (Fig. 2(d)) due to the photoreceptor absence [21].

In order to investigate spatial and temporal characteristics of the positive and negative IOSs, we depicted spatiotemporal images of the quantities of positive and negative signals in Fig. 3(a). The white dash lines in Fig. 3(a) indicated the stimulus edges. As shown in Fig. 3(a), positive and negative signals shared similar time courses

and spread out around the stimulus area. Because of the comparable time courses of the overall positive and negative signals, to simplify analysis, we inverted the negative signals and used the absolute value of IOSs as the IOS magnitude to quantify the strength of the localized stimulus-evoked activities. In order to quantitatively investigate the response differences between WT and mutant retinas over time, the IOS magnitude curves corresponding to Fig. 2(b)-2(d) were plotted in Fig. 3(b). As shown in Fig. 3(b), the signal magnitude of 2-month-old WT retina was more than five times larger than that in mutant retina of the same age. In 1-year-old mutant retina, IOS was not observed (Fig. 3(b)). Figs. 3(c) and 3(d) show statistical analysis of IOS results based on 7 two-month-old WT and 11 two-month-old mutant mice. In addition to magnitude difference, the IOS of WT mouse retinas occurred and reached peak value earlier in comparison with that of mutant retinas (Fig. 3(d)), which was consistent with previous reported ERG changes [21, 25].

3.2. Spontaneous activity in WT and mutant mouse retinas

Two-month-old *Cngb1* knockout mutant mice retinas did not show remarkable structural changes visually compared to WT mice (Fig. 4(a)). However, functional IOS images of the mutant retinas revealed irregular spatiotemporal patterns (Figs. 2(c)-2(d)). These irregular spontaneous changes occurred, without the requirement of retinal stimulation. Texture images (described in the data process section) of 4 trials of WT and mutant mouse retinas are shown in Fig. 4(b). In comparison with relative clean texture images of WT retinas, mutant retinas showed various sizes of granular like particles distributed randomly around the whole area. In order to better quantify their spatial differences, the smoothness and uniformity of texture images of 21 WT and 19 mutant

mouse retinas were compared. Statistical analysis results showed texture image for WT was four times smoother (Fig. 4(c)) and significantly more homogeneous (Fig. 4(d)) as compared to the mutant.

4. Discussion

In summary, we compared stimulus-evoked IOS responses in normal and mutant retinas to demonstrate the feasibility of IOS identification of retinal dysfunction. Both 2-month and 1-year-old mice were measured. In 2-month-old mutant mice, time course and peak value of the stimulus-evoked IOS were significantly delayed (relative to stimulus onset) and reduced, respectively, compared to age-matched WT mice. In 1-year-old mutant mice, stimulus-evoked IOSs were totally absent.

Recent morphological study of Cngb1 gene knockout mice has revealed shorter and disorientated photoreceptor (rod) outer segments over the whole retina area [21], which might result in the reduced IOS response correlated with retinal stimulation. Moreover, functional defects of the photoreceptors might further affect the IOS response. Previous studies with isolated photoreceptor outer segments and isolated retinas have demonstrated transient IOSs associated with phototransduction [26-28]. Both binding and release of G-proteins to photoexcited rhodopsin might contribute to the positive (increasing) and negative (decreasing) IOSs [27]. Localized biochemical processes might produce non-homogeneous light intensity changes, i.e. positive and negative signals mixed together. Besides the biochemical mechanism, physical changes, such as stimulus-evoked cell volume changes associated with water influx due to ionic currents through gated membrane channels might also contribute to the IOS response [29-32]. In Cngb1 gene knockout mice, it is established that the cyclic-nucleotide-gated cation channels

29

regulating ion flow into rod photoreceptor outer segment are not functioning properly, which can reduce ion movement and light sensitivity of rod photoreceptor cells [21]. Therefore, stimulus-evoked IOS changes might be substantially reduced. For 1-year knockout mice, the photoreceptors, which are responsible for capturing photons and initiating phototransduction, were completely gone, and therefore no detectable stimulus-evoked IOS was observed (Figs. 2(d) and 3(b)).

In addition to overall changes of IOS magnitude (Fig. 3(c)) and time course (Fig. 3(d)), distinct spontaneous IOS patterns were observed in WT and mutant retinas. WT mouse retinas showed clean background baseline before retinal stimulation (Fig. 2(b), and first row of Fig. 4(c)). In contrast, mutant mice showed enhanced spontaneous IOS responses which might attribute to spontaneous activity at inner neural layers. It is known that mammalian retinal degeneration gradually proceeds from outer retina to inner neural network, from the death of rods and cones to dendrite truncation in bipolar cells or even entire neural network remodeling [25, 33]. Previous reports on rod degenerated mouse models have demonstrated that the loss of photoreceptors was accompanied by a marked increase of spontaneous activity in remnant neural networks [34]. Recent studies suggested that this spontaneous activity initiated at the presynaptic network including ON cone bipolar and AII amacrine cells [35]. At early stages, before major morphological modifications in the inner retina, of retinal degeneration, abnormal time course and magnitude of ERG b-wave has been observed [25].

We anticipate that fast IOS imaging may provide a supplemental method for better understanding of disease-associated retinal dysfunctions. In comparison with ERG recording, the IOS imaging can provide improved spatial resolution and three-

dimensional imaging capability. Since Fast IOS imaging could be done noninvasively, it may lead to a new methodology for early detection of retinal dysfunction *in vivo*. High resolution IOS imaging will allow accurate disease detection and reliable treatment evaluation of age-related macular degeneration (AMD), retinitis pigmentosa (RP), diabetic retinopathy (DR), glaucoma, and other eye diseases that are known to produce retinal dysfunctions.

5. Conclusion

Unambiguous IOS abnormalities, in term of time course, magnitude, and spontaneous activity, were observed in *Cngb1* knockout mutant mouse retinas. Comparative study of WT and mutant mouse retinas demonstrates the potential of using IOS imaging for objective evaluation of disease-associated retinal dysfunctions. Further development of the IOS imaging technology may provide improved retinal disease study and diagnosis. Moreover, high spatiotemporal resolution IOS imaging may foster advanced understanding of disease-associated neural remodeling in the retina.

Acknowledgments

Reference

1. C. A. Curcio, N. E. Medeiros, and C. L. Millican, "Photoreceptor loss in age-related macular degeneration," Invest Ophthalmol Vis Sci 37, 1236-1249 (1996).

2. D. Nagy, B. Schonfisch, E. Zrenner, and H. Jagle, "Long-term follow-up of retinitis pigmentosa patients with multifocal electroretinography," Invest Ophthalmol Vis Sci 49, 4664-4671 (2008).

3. Y. W. Qin, G. Z. Xu, and W. J. Wang, "Dendritic abnormalities in retinal ganglion cells of three-month diabetic rats," Curr Eye Res 31, 967-974 (2006).

4. H. P. Scholl and E. Zrenner, "Electrophysiology in the investigation of acquired retinal disorders," Surv of ophthalmol 45, 29-47 (2000).

5. D. C. Hood, "Assessing retinal function with the multifocal technique," Prog Retin Eye Res 19, 607-646 (2000).

6. K. Holthoff and O. W. Witte, "Intrinsic optical signals in vitro: a tool to measure alterations in extracellular space with two-dimensional resolution," Brain Res Bull 47, 649-655 (1998).

7. R. D. Andrew, C. R. Jarvis, and A. S. Obeidat, "Potential sources of intrinsic optical signals imaged in live brain slices," Methods 18, 185-196, 179 (1999).

8. M. Haller, S. L. Mironov, and D. W. Richter, "Intrinsic optical signals in respiratory brain stem regions of mice: neurotransmitters, neuromodulators, and metabolic stress," J Neurophysiol 86, 412-421 (2001).

9. Y. C. Li, W. X. Cui, X. J. Wang, F. Amthor, R. W. Lu, A. Thompson, and X. C. Yao, "Intrinsic optical signal imaging of glucose-stimulated insulin secreting beta-cells," Opt Express 19, 99-106 (2011).

10 X. C. Yao, A. Yamauchi, B. Perry, and J. S. George, "Rapid optical coherence tomography and recording functional scattering changes from activated frog retina," Appl Opt 44, 2019-2023 (2005).

11. X. C. Yao and J. S. George, "Dynamic neuroimaging of retinal light responses using fast intrinsic optical signals," Neuroimage 33, 898-906 (2006).

12. X. C. Yao and J. S. George, "Near-infrared imaging of fast intrinsic optical responses in visible light-activated amphibian retina," J Biomed Opt 11, 064030 (2006).

13. X. C. Yao and Y. B. Zhao, "Optical dissection of stimulus-evoked retinal activation," Opt Express 16, 12446-12459 (2008).

14. X. C. Yao, L. Liu, and Y. G. Li, "Intrinsic optical signal imaging of retinal activity in frog eye," J Innov Opt Health Sci 2, 201–208 (2009).

15. Q. X. Zhang, J. Y. Wang, L. Liu, and X. C. Yao, "Microlens array recording of localized retinal responses," Opt Lett 35, 3838-3840 (2010).

16. J. Schallek, H. Li, R. Kardon, Y. Kwon, M. Abramoff, P. Soliz, and D. Ts'o, "Stimulus-evoked intrinsic optical signals in the retina: spatial and temporal characteristics," Invest Ophthalmol Vis Sci 50, 4865-4872 (2009).

17. Qiu-Xiang Zhang, Rong-Wen Lu, Yang-Guo Li, and Xin-Cheng Yao, "In vivo confocal imaging of fast intrinsic optical signals correlated with frog retinal activation," Opt. Lett. 36, 4692-4694 (2011).

18. V. J. Srinivasan, Y. Chen, J. S. Duker, and J. G. Fujimoto, "In vivo functional imaging of intrinsic scattering changes in the human retina with high-speed ultrahigh resolution OCT," Opt Express 17, 3861-3877 (2009).

19. R. S. Jonnal, J. Rha, Y. Zhang, B. Cense, W. H. Gao, and D. T. Miller, "In vivo functional imaging of human cone photoreceptors," Opt Express 15, 16141-16160 (2007).

20. T. Theelen, C. B. Hoyng, B. J. Klevering, and C. B, "Functional imaging of inherited retinal disease with a commercial optical coherence tomography," Proc of SPIE 8091, 8009110-8009118 (2011).

21. Y. Zhang, L. L. Molday, R. S. Molday, S. S. Sarfare, M. L. Woodruff, G. L. Fain, T. W. Kraft, and S. J. Pittler, "Knockout of GARPs and the beta-subunit of the rod cGMP-gated channel disrupts disk morphogenesis and rod outer segment structural integrity," J Cell Sci 122, 1192-1200 (2009).

22. Y. G. Li, Q. X. Zhang, L. Liu, F. Amthor, and X. C. Yao, "High spatiotemporal resolution imaging of fast intrinsic optical signals activated by retinal flicker stimulation," Opt Express 18, 7210-7218 (2010).

23. G. L. Kesteven, "The coefficient of variation," Nature 158, 520 (1946).

24. X. Huang, W. Kong, Y. Zhou, and G. Gregori, "Distortion of axonal cytoskeleton: an early sign of glaucomatous damage," Invest Ophthalmol Vis Sci 52, 2879-2888.

25. C. Gargini, E. Terzibasi, F. Mazzoni, and E. Strettoi, "Retinal organization in the retinal degeneration 10 (rd10) mutant mouse: a morphological and ERG study," J Comp Neurol 500, 222-238 (2007).

26. K. P. Hofmann, R. Uhl, W. Hoffmann, and W. Kreutz, "Measurements on fast light-induced light-scattering and -absorption changes in outer segments of vertebrate light sensitive rod cells," Biophys Struct Mech 2, 61-77 (1976).

27. H. Kuhn, N. Bennett, M. Michel-Villaz, and M. Chabre, "Interactions between photoexcited rhodopsin and GTP-binding protein: kinetic and stoichiometric analyses from light-scattering changes," Proc Natl Acad Sci U S A 78, 6873-6877 (1981).

28. V. Y. Arshavsky, T. D. Lamb, and E. N. Pugh, Jr., "G proteins and phototransduction," Annu Rev Physiol 64, 153-187 (2002).

29. X. C. Yao, D. M. Rector, and J. S. George, "Optical lever recording of displacements from activated lobster nerve bundles and Nitella internodes," Appl Opt 42, 2972-2978 (2003).

30. I. Tasaki and P. M. Byrne, "Rapid structural changes in nerve fibers evoked by electric current pulses," Biochem Biophys Res Commun 188, 559-564 (1992).

31. G. H. Kim, P. Kosterin, A. L. Obaid, and B. M. Salzberg, "A mechanical spike accompanies the action potential in Mammalian nerve terminals," Biophys J 92, 3122-3129 (2007).

32. L. B. Cohen, "Changes in neuron structure during action potential propagation and synaptic transmission," Physiol Rev 53, 373-418 (1973).

33. R. E. Marc, B. W. Jones, C. B. Watt, and E. Strettoi, "Neural remodeling in retinal degeneration," Prog Retin Eye Res 22, 607-655 (2003).

34. S. F. Stasheff, "Emergence of sustained spontaneous hyperactivity and temporary preservation of OFF responses in ganglion cells of the retinal degeneration (rd1) mouse," J Neurophysiol 99, 1408-1421 (2008).

35. J. Borowska, S. Trenholm, and G. B. Awatramani, "An intrinsic neural oscillator in the degenerating mouse retina," J Neurosci 31, 5000-5012.
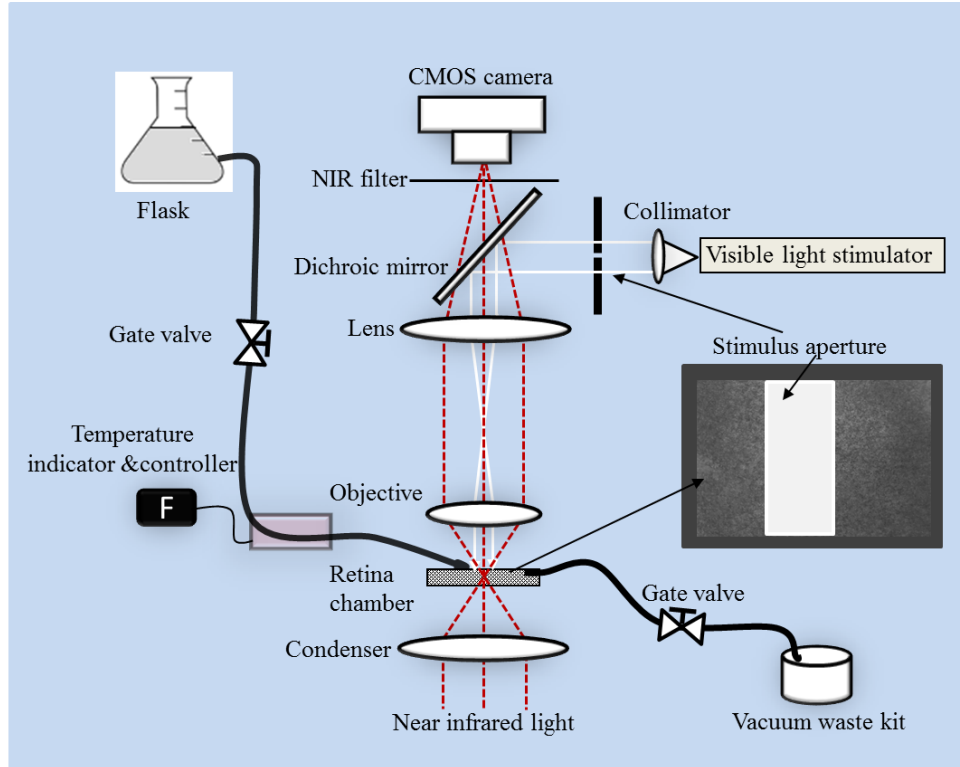
Figure 1. Schematic diagram of experiment setup. A custom modified microscope, with 20x objective and high speed CMOS camera (10 bits depth and 1000 frames/s), was used for this study. During the measurement, the mouse retina was continuously illuminated by the NIR light for IOS recording; a 10 ms visible light flash was used for retinal stimulation.
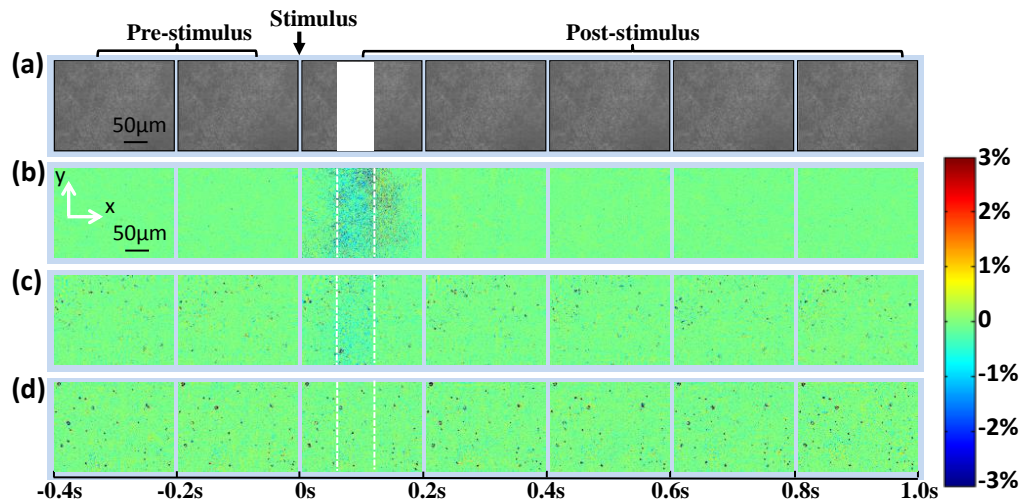
Figure 2. Representative images of a mouse retina. (a) Representative images of a mouse retina. The white rectangle in the third frame showed the visible stimulus pattern. The black arrow indicated the delivery of stimulus light. (b) Dynamic differential IOS images of two-month-old WT mouse retina. (c) Dynamic differential IOS images of two-month-old mutant mouse retina. (d) Dynamic differential IOS images of 1-year-old mutant retina. Scale bars (in black) represent 50 μm.
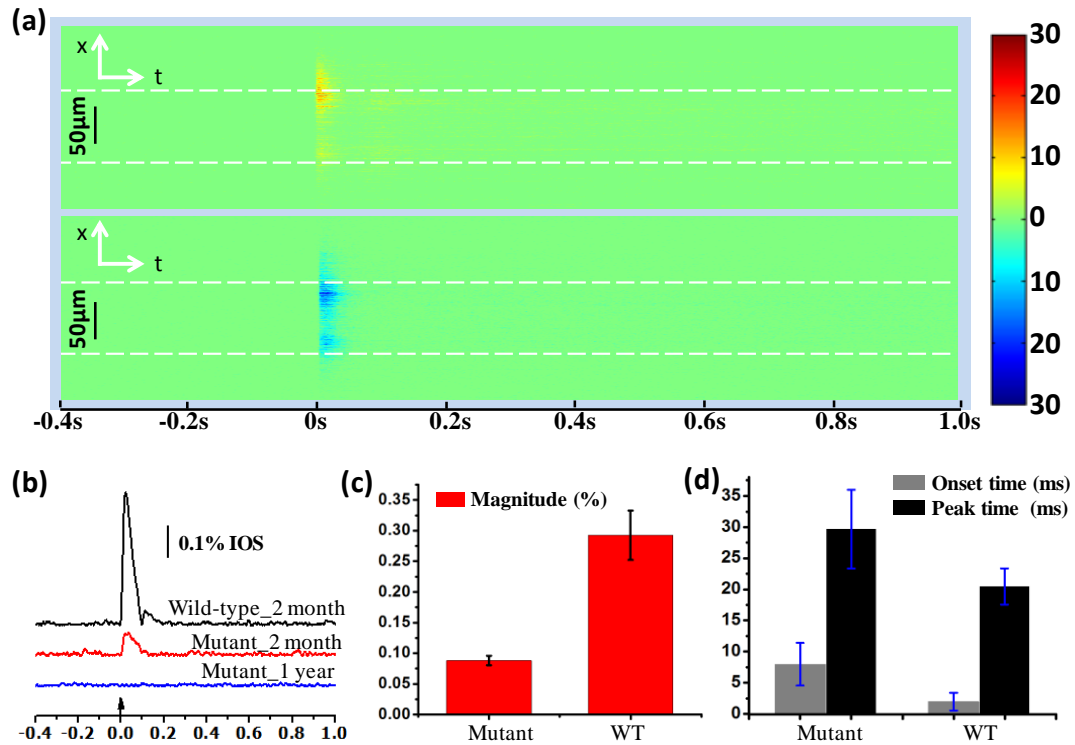
Figure 3. Spatiotemporal patterns of positive and negative IOS signals. (a) Spatiotemporal patterns of positive and negative IOS signals, corresponding to Fig. 2(b). The top panel is the image of positive pixel numbers and the bottom is negative signal pixel numbers. The unit of the color bar is pixel number. Scale bars (in black) represent 50 μm. The vertical axis (x) corresponds to the horizontal axis (x) in Fig. 2(b). The method to reconstruct spatiotemporal images was described in the section of data processing. (b) Dynamic IOS magnitude changes of the three retinas shown in Fig. 2(b)-2(d). (c) Statistical analysis of IOS magnitude of 7 two-month-old WT and 11 two-month-old mutant mouse retinas ($p<0.0001$). (d) Statistical analysis of corresponding IOS onset time ($p<0.0004$) and peak time ($p<0.002$).
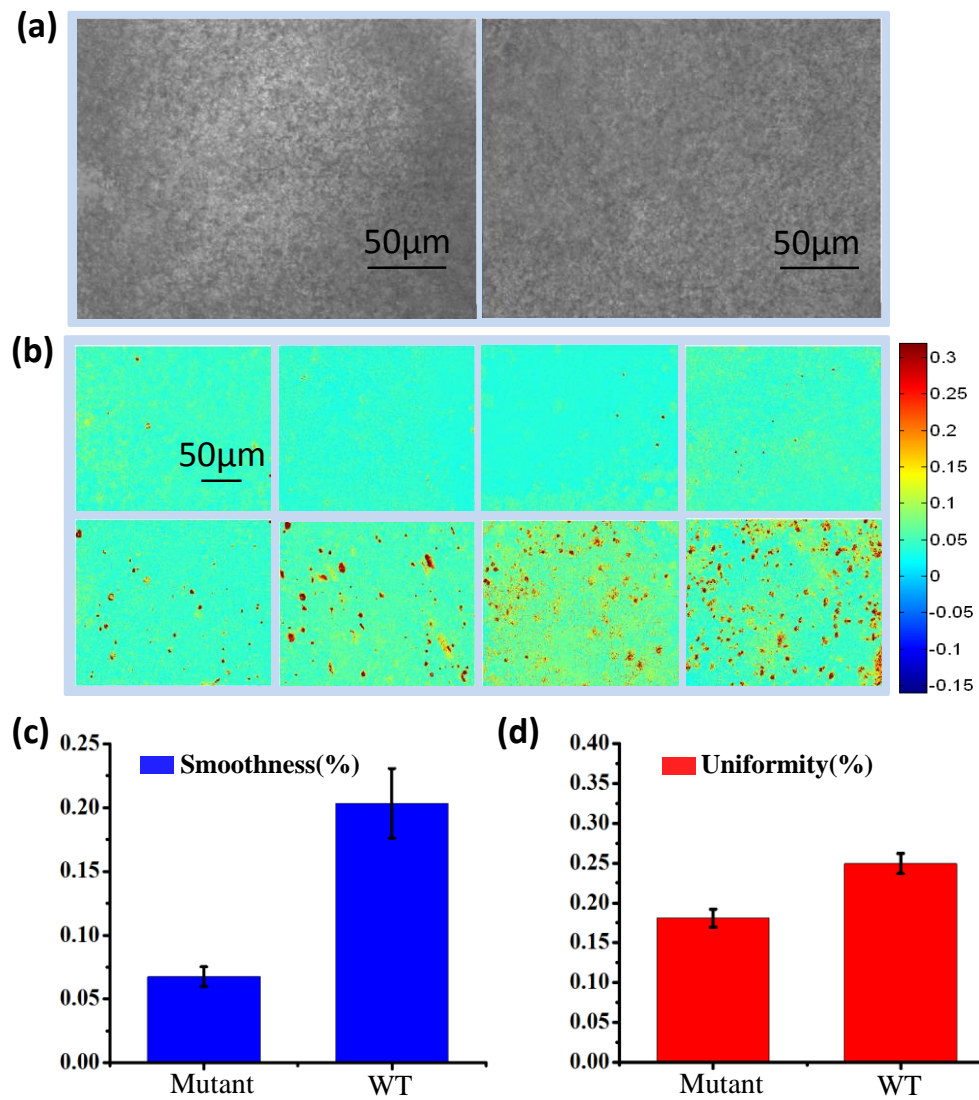
Figure 4. Structural images of 2-month-old WT (left) and mutant (right) mouse retinas. (a) Raw structure images of 2-month-old WT (left) and mutant (right) mouse retinas; (b) Texture images of WT (top) and mutant (bottom) mouse retina. The texture images represent the strength of spontaneous activity over the pre-stimulus time. (c) Statistical analysis of background smoothness of 21 WT and 19 mutant mouse retinas

(p<0.0001). (d) Statistical analysis of background uniformity (p=0.002). Scale bars represent 50 µm.

IN VIVO CONFOCAL INTRINSIC OPTICAL SIGNAL IDENTIFICATION OF
LOCALIZED RETINAL DYSFUNCTION

by

QIUXIANG ZHANG, RONGWEN LU, CHRISTINE A. CURCIO AND XINCHENG

YAO

Format adapted and errata corrected for dissertation

Abstract

Purpose: The purposes of this study are to investigate the physiological mechanism of stimulus-evoked fast intrinsic optical signals (IOSs) recorded in dynamic confocal imaging of the retina, and to demonstrate the feasibility of *in vivo* confocal-IOS mapping of localized retinal dysfunctions.

Methods: A rapid line-scan confocal ophthalmoscope was constructed to achieve *in vivo* confocal-IOS imaging of frog (*Rana Pipiens*) retinas at cellular resolution. In order to investigate the physiological mechanism of confocal-IOS, comparative IOS and electroretinography (ERG) measurements were conducted using normal frog eyes activated by variable intensity stimuli. A dynamic spatiotemporal filtering algorithm was developed to reject the contamination of hemodynamic changes on fast IOS recording. Laser-injured frog eyes were employed to test the potential of confocal-IOS mapping of localized retinal dysfunctions.

Results: Comparative IOS and ERG experiments revealed a close correlation between the confocal-IOS and retinal ERG, particularly the ERG a-wave which has been widely used to evaluate photoreceptor function. IOS imaging of laser-injured frog eyes indicates that the confocal-IOS can unambiguously detect localized (30 µm) functional lesions in the retina before a morphological abnormality is detectable.

Conclusions: The confocal-IOS predominantly results from retinal photoreceptors, and can be used to map localized photoreceptor lesion in laser-injured frog eyes. We anticipate that confocal-IOS imaging can provide applications in early detection of age-

related macular degeneration, retinitis pigmentosa and other retinal diseases that can cause pathological changes in the photoreceptors.

Introduction

It is well established that many eye diseases involve pathological changes of photoreceptors and/or their support system, including different forms of retinitis pigmentosa (RP)[1] and age-related macular degeneration (AMD)[2-5], a highly prevalent outer retinal disease. To prevent or slow the progress of vision loss associated with outer retinal disease, early detection and reliable assessment of medical interventions, including morphological examinations, are key elements. The application of adaptive optics (AO) and optical coherence tomography (OCT) has enabled retinal fundus imaging with cellular resolution. However, disease-associated morphological and functional changes, if independently measured, are not always correlated directly in time course and spatial location[6, 7]. Therefore, a combined assessment of retinal function and structure is essential.

Psychophysical methods that access outer retinal function, such as visual acuity (VA) testing, are practical in clinical applications, but the VA test involves extensive higher order cortical processing. Therefore, VA testing does not provide information on retinal function exclusively and lacks sensitivity for early detection of outer retinal diseases, such as AMD[8, 9] . Electroretinography (ERG) methods, including full-field ERG[10], focal ERG[11-15], multifocal ERG[16-18], etc., have been established for objective examination of retinal function. However, the spatial resolution of ERG may not be high enough to

provide direct comparison of localized morphological and functional changes in the retina.

Stimulus-evoked fast intrinsic optical signals (IOSs) provide a promising alternative to ERG for objective measurement of retinal function with improved spatial resolution[19, 20]. We have recently demonstrated *ex vivo* IOS identification of localized retinal dysfunction in an inherited photoreceptor degeneration model [21]. Because functional IOS images are constructed through spatiotemporal processing of pre- and post-stimulus images, concurrent structural and functional measurements can be naturally achieved using a single optical instrument. Conventional fundus cameras have been used to detect IOSs from anesthetized cats and monkeys[22-25] and awake humans[26]. Given limited axial resolution, fundus IOS imaging does not exclusively reflect retinal neural function due to complex contaminations of other ocular tissues. In principle, adaptive optics[27-29], and optical coherence tomography (OCT) imagers [30-32] can provide resolution at cellular resolution. However, the signal source and mechanism of these imaging modalities are not well established, and functional mapping of fast IOSs that have time courses comparable to retinal electrophysiological kinetics is still challenging.

We recently developed a line-scan confocal microscope to achieve fast IOS imaging at high-spatial (μm) and high-temporal (ms) resolution[33]. Rapid *in vivo* confocal-IOS imaging has revealed a transient optical response with a time course comparable to ERG. In this paper, we report comparative confocal-IOS imaging and retinal ERG recording to investigate the physiological mechanism of confocal-IOS[33-35], and demonstrate confocal-IOS identification of localized acute retinal lesions in an animal model, i.e., laser-injured frog eyes.

Methods

Experimental Setup

Figure 1 illustrates the schematic diagram of our line-scan confocal ophthalmoscope for confocal-IOS imaging. The optical rationale of the line-scan confocal-IOS imaging has been reported in our previous publication[34]. In this study, the imaging system was upgraded with a new fast linear CCD camera (EV71YEM2CL1014-BA0, E2V, NY, USA). The new camera was equipped with camera link interface that greatly facilitated system control and data synchronization. The line-scan confocal imaging system consisted of two light sources: near infrared (NIR) for IOS recording and visible green for retinal stimulation. The NIR light was produced by a superluminescent laser diode (SLD) (SLD-35-HP, Superlum, Co.Cork, Ireland) with center wavelength of 830 nm. A single-mode fiber coupled 532-nm DPSS laser module (FC-532-020-SM-APC-1-1-ST, RGBLase LLC, CA, USA) was used to produce the visible light for stimulating or injuring the retina locally. It provided adjustable output power from 0 to 20 mW at the fiber end. A mechanical slit (VA100, Thorlabs, NJ, USA) was placed behind the collimated green stimulus light to produce a rectangle pattern and provide precise adjustment of stimulus width.

A custom program (Labview 2011) was developed for system synchronization, high-speed image acquisition, and real-time image display. Before each IOS recording, stimulus timing and location in the field of view were tested for repeatability and accuracy. During each experiment, the retina was continuously illuminated by the NIR light at ~600 µW. For each IOS recording trial, 400 ms pre-stimulus and 800 ms after-stimulus images were recorded at the speed of 100 frames/s, with frame size of 350 x 100

pixels (~ 300 μm x 85 μm at the retina). Exposure time of the line-scan CCD camera was 71.4286 μs. Scanning speed of the mirror was 100 Hz.

The ERG was recorded by placing differential electrodes on two eyes. The ERG signal was amplified with a physiological amplifier (DAM 50, World Precision Instruments, FL, USA) equipped with a band-pass (0.1 Hz to 10 kHz) filter. The pre-amplified ERG was digitized using a 16-bit DAQ card (NI PCIe-6351, National Instruments, TX, USA) with a resolution of 1.6 mV and was sent to the computer for averaging, display and storage.

Animal Preparation

The northern leopard frog (*Rana pipiens*) was selected to take advantage of the high-quality optics of the ocular lens[36] and the large size of the retinal photoreceptors (cone, 3 μm; rod, 6 μm)[37]. Together, these characteristics made it possible to resolve individual photoreceptors (blue arrowhead in Figure 2A) and blood vessels (yellow arrowheads in Figure 2A and movie 1) in vivo. The experimental procedure was approved by the Institutional Animal Care and Use Committee of the University of Alabama at Birmingham and carried out in accordance with the guidelines of the ARVO Statement for the Use of Animals in Ophthalmic and Vision Research. Frogs were dark adapted for at least 2 hours prior to functional IOS imaging. Then, the frog was anesthetized by immersion in tricaine methanesulfonate solution (TMS, MS-222; 500 mg/liter)[38]. Pupils were fully dilated with topical atropine (0.5%) and phenylephrine (2.5%). After confirmation of the anesthesia, the frog was placed in a custom-built holder for IOS imaging. The holder provided five degrees of freedom to facilitate adjustment of body orientation and retinal area for IOS imaging.

Experimental Design

A rectangular stimulus bar with 30-µm width (Figure 3A) and 20-ms duration was used for localized retinal stimulation. Estimated maximum stimulus flash intensity was $3.5\text{x}10^5$ photons/µm^2/ms ($7\text{x}10^6$ photons/µm^2 for 20 ms) at the retina. Neutral density filters were used to adjust light intensity for retinal stimulation. The IOS and ERG were recorded over a 5.0 log unit range in 9 steps, namely, -5.0, -4.0, -3.0, -2.5, -2.0, -1.5, -1.0, -0.5, and 0.0. Stimulus flashes were presented at 2-minute intervals (Figure 4). IOS and ERG recordings were performed consecutively in the same frog eye, as explained in the results.

Both normal and laser-injured frogs were used in this study. To produce a localized retina laser-injury, a 30-µm width green laser light bar with output power of 1 mW at the retina surface was continuously delivered into the retina for 30 s. Thirty minutes after local damage was induced, a full-field stimulus (Figure 5) was applied to injured and non-injured area to obtain the retinal response pattern.

Data Analyses

The raw images were processed using a custom program with a user friendly GUI interface in MATLAB R2011a (The MathWorks, Natick, MA, USA). Raw images were registered to compensate for eye movements before IOS calculation (Fig. 3A). Basic procedures of IOS data processing have been previously reported[19].

As shown in Figure 2A, ocular blood vessels can superimpose on photoreceptor cells, and hemodynamic changes inherent to rapid blood flow may contribute to fast IOS recording. Retinal blood vessels can be mapped based on dynamic optical changes correlated with

blood flow [39]. We adapted the strategy to separate stimulus-evoked fast IOS in retinal photoreceptors from blood flow-induced optical change. Key procedures of the dynamic spatiotemporal filtering are summarized as follows:

1) To calculate the mean $\bar{I}(x, y)$ of each pixel in the pre-stimulus baseline recording (n frames)

$$\bar{I}(x, y) = \frac{1}{n}\sum_{j=1}^{j=n} I_{t_j}(x, y)$$

(1)

2) To calculate the standard deviation $\sigma(x, y)$ of each pixel in the pre-stimulus baseline recording: (n frames)

$$\sigma(x, y) = \sqrt{\frac{1}{n}\sum_{j=1}^{j=n}\left[I_{t_j}(x, y) - \bar{I}(x, y)\right]^2}$$

(2)

3) To conduct spatiotemporal filtering of potential noises. Because blood flow changes dynamically, the variability of light intensity at the blood vessels in temporal is much larger than that at the blood-free area, i.e. before the stimulus, the temporal $\sigma(x, y)$ of blood flow is much larger than that of photoreceptors. Upon stimulation, blood flow may increase, but within the short recording time (1s), hemodynamic change is slow. Therefore, the temporal $\sigma(x, y)$ change of blood flow is insignificant compared with the fast IOSs from the photoreceptors. To reject noise attributable to blood flow, values three standard deviations above or below the mean at each pixel was used as a filtering criterion. This filter (3-σ) allowed us to plot the vasculature profile as shown in Figure 2B. In other words, the pixel change will be assumed to reflect noise, if

$$\bar{I}(x,y) - 3\sigma(x,y) < I_{t_i}(x,y) < \bar{I}(x,y) + 3\sigma(x,y)$$

(3)

Therefore, a high threshold is used to define stimulus-evoked IOS in the retinal area superimposed by blood vessels. The signals at pixel (x, y) with light intensity greater than the mean above three standard deviations are positive and less than the mean below three standard deviations are negative. IOS images with pixels that fall into the noise range are forced to be zero and only positive or negative IOSs are left. Therefore, after dynamic spatiotemporal filtering (Fig. 3C), most hemodynamic-driven optical signals (Fig. 3B) can be rejected.

Confocal-IOS imaging of Localized Retinal Response

Experiments were designed to validate the feasibility of line-scan confocal-IOS imaging of localized retinal response in intact frog eye. The stimulus light intensity was at -1 log unit. Each illustrated frame in Figure 3 is the average of two raw/IOS images obtained during a 20-ms epoch. Additionally, 40-ms pre-stimulus and 80-ms post-stimulus recordings are shown.

In Figure 3B, an IOS pattern was observed after a rectangular stimulus was delivered, whereas the blood vessels showed persistent optical changes. After setting the pixels falling within the range defined by Eq. (3) to zero, most of the rapid blood flow activities were excluded from stimulus-evoked retinal responses. With a clean background, the stimulus activated IOS pattern can be visualized clearly from Figure 3C. Both positive and negative signals were observed almost immediately after retinal stimulation. Fig. 3D shows the IOS pattern by plotting absolute magnitude and ignoring the signal polarities.

Physiological Source of the Confocal-IOS

Experiments were designed to determine the physiological source of confocal-IOS by comparing IOS imaging and ERG recording. Figure 4A shows representative IOS magnitude dynamics elicited by 9 different stimulus strengths over a 5 log unit range. Figure 4B illustrates ERG waveforms recorded under the same conditions. The amplitude of the a-wave was measured from baseline to trough. The amplitude of the b-wave was measured from the a-wave trough to b-wave peak. IOS and ERG signals were not measured simultaneously. Rather, they were recorded with the same stimulus/illumination light and in the same eye. Both IOS and ERG signals were averaged based on 4 trials/eyes. For the first and third trial/eye, IOSs was first recorded, then ERG. For the second and fourth trial/eye, the order was changed to ERG recording first, followed by IOSs. In this way, differences in experiment conditions between IOS and ERG recordings could be minimized. It was typically observed that the IOS occurred almost immediately after the stimulus delivery, reaching peak magnitude within 150 ms. To compare time courses of IOS and ERG dynamics, ERG a-wave, b-wave, and IOS magnitudes were normalized as shown in Figure 4C. The amplitude of the b-wave first increased almost linearly with the gradual increased intensity of the stimulus, reached a maximum and then decreased as light intensity became higher than -1.5 log units. The a-wave is widely accepted as a measure of photoreceptor function[40]. At low stimulus light intensities (below -3 log units), a-wave amplitude increased slowly with increased stimulus intensity, whereas it increased much faster when the light intensity was above -3 log units. Maximum a-wave amplitude was found at the light intensity of -0.5 log units, ten times higher than the maximum of -1.5 log units for the b-wave. As we can see from

Figure 4C, the overall trend of IOS magnitude was quite consistent with that of a-wave amplitude, including the threshold and maximum response. This suggests that confocal-IOSs predominantly originate from retinal photoreceptors.

Time-to-peak values of the IOS and ERG recordings also show similar dependency on stimulus intensity, decreasing as the light intensity increased (Figure 4D).

IOS Detection of Localized Retinal Lesion

This experiment was designed to demonstrate IOS identification of localized retinal lesions in laser-injured frog eyes.

Figure 5A1 shows retinal structure before laser damage. A full field stimulus with moderate intensity (at -1.5 log units) was applied to conduct confocal-IOS imaging. The corresponding 3D surface envelope of the IOS image recorded within 0.1 s after stimulus delivery is illustrated in Figure 5A2. For better visualization of the overall IOS distribution pattern, we smoothed the IOS image using a mean filter (kernel size 15 μm x 15 μm). A relatively homogeneous signal distribution pattern was displayed (Figure 5A3).

In order to demonstrate the feasibility of detecting localized retinal damage, a 30-μm lesion was introduced after a control test (Figure 5A1-3). Thirty minutes after the laser exposure, the same full field stimulus was applied to this retinal area. From the structural images of Figure 5A1 and Figure 5B1, we could barely observe any visible changes. However, IOS images with full field stimulus showed a signal-absent slit area located at the place where the laser damage was introduced (Figure 5B2). By using the smoothing method described above, the IOS magnitude image (Figure 5B3) showed a clear 30-μm-wide rectangle of markedly reduced signal. Therefore, our experiment indicated that

rapid line-scan IOS imaging of intact frogs could be used for *in vivo* investigation of this localized retinal lesion.

Discussion

In summary, a rapid line-scan confocal imager was employed to achieve cellular resolution IOS imaging of retinal photoreceptors *in vivo*. The confocal-IOS patterns show tight correlation with localized retinal stimulation (Figure 3). A spatiotemporal filtering algorithm was developed to separate stimulus-evoked fast IOS response from blood flow. Given the fact that blood flow could induce significant optical fluctuation independent of retinal stimulation and blood flow associated artifact could be readily excluded by dynamic threshold rejection. This spatiotemporal filtering assumes that blood flow associated optical changes at any one location were consistent before and after stimulus delivery. Although it is possible that retinal stimulation may produce hemodynamic changes in the blood vessel area, we did not detect significant changes in the short (0.8 s) after-stimulus recording epoch.

Comparative ERG measurements were conducted to investigate physiological sources of the confocal-IOS. Our experiments revealed tight correlation between the IOS response and ERG a-wave. Both magnitudes and time-courses of the IOS and a-wave showed similar responses to stimulus intensity changes. The time-to-peak of IOSs fell between the a-wave and b-wave. It is well established that the a-wave leading edge is dominated by retinal photoreceptors, and the later phase is truncated by electrophysiological response of inner retinal neurons, particularly ON bipolar cells. If we record a pure photoreceptor response, i.e., post-photoreceptor neurons are blocked, the a-wave should take more time to return the baseline, which results in longer time to

reach peak compared with the a-wave of standard ERGs[41-43]. From this perspective, if we assume the fast IOSs originate from retinal photoreceptors, the measured time-to-peak of the IOS should be longer than that of the standard a-wave, but shorter than b-wave, which is consistent with our experimental results. Therefore, we speculate that the confocal-IOSs originate mainly from retinal photoreceptors. In addition, because of the frog eye's high numerical aperture (0.4), the axial resolution of confocal-IOS imaging was estimated at ~10 μm. This resolution was sufficient to distinguish the photoreceptors from other retinal layers. Previous studies with isolated photoreceptor outer segments and isolated retinas have demonstrated transient IOSs associated with phototransduction[44-46]. Both binding and release of G-proteins to photo-excited rhodopsin might contribute to the positive (increased) and negative (decreased) IOSs[45]. Localized biochemical processes might produce non-homogeneous light intensity changes, i.e. positive and negative signals mixed together.

A laser-injured frog model was used to validate confocal-IOS identification. By inducing localized retinal lesions through green laser exposure, we demonstrated that confocal-IOS imaging can provide high transverse resolution, at least 30 μm. Based on early investigations of laser damage in other animal models[47-49], we estimated that our laser exposure could produce severe photoreceptor damage. Further investigation is required to quantify the laser thresholds that can produce detectable cone and rod photoreceptor damages.

Better development of high-resolution confocal-IOS imaging can lead to reliable physiological assessment of individual retinal photoreceptors. This prospect is particularly important for rods, known to be more vulnerable than cones in aging and in

early AMD [2, 50], the most common cause of severe vision loss and legal blindness in adults over 50[2, 51]. Early detection and reliable assessment of medical interventions are key elements in preventing or slowing the progress of AMD associated vision loss. Both morphological[52] and functional[50, 53] tests are important for reliable detection of AMD. Currently, there is no established strategy to allow objective assessment of retinal dysfunction at high resolution to allow direct comparison between localized physiological and morphological abnormalities in early AMD or other eye diseases. Confocal-IOS imaging will enable concurrent morphological and functional assessment of localized retinal dysfunctions *in vivo*. Further, it can be combined with technologies that assess structure and function of the photoreceptor support system that is affected even earlier in AMD. This combination could revolutionize the study, diagnosis and therapy assessment of AMD.

Acknowledgments

References

1. Nagy D, Schonfisch B, Zrenner E, Jagle H. Long-term follow-up of retinitis pigmentosa patients with multifocal electroretinography. *Invest Ophthalmol Vis Sci* 2008;49:4664-4671.

2. Curcio CA, Medeiros NE, Millican CL. Photoreceptor loss in age-related macular degeneration. *Invest Ophthalmol Vis Sci* 1996;37:1236-1249.

3. Falsini B, Serrao S, Fadda A, et al. Focal electroretinograms and fundus appearance in nonexudative age-related macular degeneration. Quantitative relationship between retinal morphology and function. *Graefes Arch Clin Exp Ophthalmol* 1999;237:193-200.

4. Hogg RE, Chakravarthy U. Visual function and dysfunction in early and late age-related maculopathy. *Prog Retin Eye Res* 2006;25:249-276.

5. Jackson GR, Owsley C, Curcio CA. Photoreceptor degeneration and dysfunction in aging and age-related maculopathy. *Ageing Research Reviews* 2002;1:381-396.

6. Falsini B, Marangoni D, Salgarello T, et al. Structure-function relationship in ocular hypertension and glaucoma: interindividual and interocular analysis by OCT and pattern ERG. *Graefes Arch Clin Exp Ophthalmol* 2008.

7. Oishi A, Otani A, Sasahara M, et al. Retinal nerve fiber layer thickness in patients with retinitis pigmentosa. *Eye* 2008.

8. Klein R, Wang Q, Klein BE, Moss SE, Meuer SM. The relationship of age-related maculopathy, cataract, and glaucoma to visual acuity. *Investigative ophthalmology & visual science* 1995;36:182-191.

9. Siderov J, Tiu AL. Variability of measurements of visual acuity in a large eye clinic. *Acta Ophthalmol Scand* 1999;77:673-676.

10. Scholl HP, Zrenner E. Electrophysiology in the investigation of acquired retinal disorders. *Survey of ophthalmology* 2000;45:29-47.

11. Vaegan, Billson F, Kemp S, Morgan M, Donnelley M, Montgomery P. Macular electroretinograms: their accuracy, specificity and implementation for clinical use. *Australian journal of ophthalmology* 1984;12:359-372.

12. Seiple WH, Siegel IM, Carr RE, Mayron C. Evaluating macular function using the focal ERG. *Invest Ophthalmol Vis Sci* 1986;27:1123-1130.

13. Fish GE, Birch DG. The focal electroretinogram in the clinical assessment of macular disease. *Ophthalmology* 1989;96:109-114.

14. Binns A, Margrain TH. Development of a technique for recording the focal rod ERG. *Ophthalmic and Physiological Optics* 2006;26:71-79.

15. Binns A, Margrain TH. Evaluation of retinal function using the dynamic focal cone ERG. *Ophthalmic and Physiological Optics* 2005;25:492-500.

16. Hood DC, Odel JG, Chen CS, Winn BJ. The multifocal electroretinogram. *J Neuroophthalmol* 2003;23:225-235.

17. Hood DC. Assessing retinal function with the multifocal technique. *Prog Retin Eye Res* 2000;19:607-646.

18. Ball SL, Petry HM. Noninvasive assessment of retinal function in rats using multifocal electroretinography. *Invest Ophthalmol Vis Sci* 2000;41:610-617.

19. Yao XC, Zhao YB. Optical dissection of stimulus-evoked retinal activation. *Opt Express* 2008;16:12446-12459.

20. Li YG, Zhang QX, Liu L, Amthor F, Yao XC. High spatiotemporal resolution imaging of fast intrinsic optical signals activated by retinal flicker stimulation. *Opt Express* 2010;18:7210-7218

21. Zhang QX, Zhang Y, Lu RW, et al. Comparative intrinsic optical signal imaging of wild-type and mutant mouse retinas. *Opt Express* 2012;20:7646-7654.

22. Schallek J, Li H, Kardon R, et al. Stimulus-evoked intrinsic optical signals in the retina: spatial and temporal characteristics. *Invest Ophthalmol Vis Sci* 2009;50:4865-4872.

23. Schallek JB, McLellan GJ, Viswanathan S, Ts'o DY. Retinal intrinsic optical signals in a cat model of primary congenital glaucoma. *Invest Ophthalmol Vis Sci* 2012;53:1971-1981.

24. Tsunoda K, Hanazono G, Inomata K, Kazato Y, Suzuki W, Tanifuji M. Origins of retinal intrinsic signals: a series of experiments on retinas of macaque monkeys. *Jpn J Ophthalmol* 2009;53:297-314.

25. Inomata K, Tsunoda K, Hanazono G, et al. Distribution of retinal responses evoked by transscleral electrical stimulation detected by intrinsic signal imaging in macaque monkeys. *Invest Ophthalmol Vis Sci* 2008;49:2193-2200.

26. Abramoff MD, Kwon YH, Ts'o D, et al. Visual stimulus-induced changes in human near-infrared fundus reflectance. *Investigative ophthalmology & visual science* 2006;47:715-721.

27. Jonnal RS, Rha J, Zhang Y, Cense B, Gao WH, Miller DT. In vivo functional imaging of human cone photoreceptors. *Optics Express* 2007;15:16141-16160.

28. Grieve K, Roorda A. Intrinsic signals from human cone photoreceptors. *Invest Ophthalmol Vis Sci* 2008;49:713-719.

29. Rha J, Schroeder B, Godara P, Carroll J. Variable optical activation of human cone photoreceptors visualized using a short coherence light source. *Optics letters* 2009;34:3782-3784.

30. Yao XC, Yamauchi A, Perry B, George JS. Rapid optical coherence tomography and recording functional scattering changes from activated frog retina. *Applied Optics* 2005;44:2019-2023.

31. Srinivasan VJ, Wojtkowski M, Fujimoto JG, Duker JS. In vivo measurement of retinal physiology with high-speed ultrahigh-resolution optical coherence tomography. *Opt Lett* 2006;31:2308-2310.

32. Bizheva K, Pflug R, Hermann B, et al. Optophysiology: depth-resolved probing of retinal physiology with functional ultrahigh-resolution optical coherence tomography. *Proceedings of the National Academy of Sciences of the United States of America* 2006;103:5066-5071.

33. Li YG, Liu L, Amthor F, Yao XC. High-speed line-scan confocal imaging of stimulus-evoked intrinsic optical signals in the retina. *Optics Letters* 2010;35:426-428.

34. Zhang QX, Lu RW, Li YG, Yao XC. In vivo confocal imaging of fast intrinsic optical signals correlated with frog retinal activation. *Opt Lett* 2011;36:4692-4694.

35. Zhang QX, Wang JY, Liu L, Yao XC. Microlens array recording of localized retinal responses. *Optics Letters* 2010;35:3838-3840.

36. Li G, Zwick H, Stuck B, Lund DJ. On the use of schematic eye models to estimate retinal image quality. *J Biomed Opt* 2000;5:307-314.

37. Nilsson SE. An Electron Microscopic Classification of the Retinal Receptors of the Leopard Frog (Rana Pipiens). *J Ultrastruct Res* 1964;10:390-416.

38. Cakir Y, Strauch SM. Tricaine (MS-222) is a safe anesthetic compound compared to benzocaine and pentobarbital to induce anesthesia in leopard frogs (Rana pipiens). *Pharmacological reports : PR* 2005;57:467-474.

39. Wang RK, Jacques SL, Ma Z, Hurst S, Hanson SR, Gruber A. Three dimensional optical angiography. *Opt Express* 2007;15:4083-4097.

40. Hood DC, Birch DG. A quantitative measure of the electrical activity of human rod photoreceptors using electroretinography. *Visual neuroscience* 1990;5:379-387.

41. Algvere P. The A-wave of the human electroretinogram during the course of dark adaptation. *Acta ophthalmologica* 1967;45:703-719.

42. Hood DC, Birch DG. Human cone receptor activity: the leading edge of the a-wave and models of receptor activity. *Visual neuroscience* 1993;10:857-871.

43. Paupoo AA, Mahroo OA, Friedburg C, Lamb TD. Human cone photoreceptor responses measured by the electroretinogram [correction of electoretinogram] a-wave during and after exposure to intense illumination. *The Journal of physiology* 2000;529 Pt 2:469-482.

44. Hofmann KP, Uhl R, Hoffmann W, Kreutz W. Measurements on fast light-induced light-scattering and -absorption changes in outer segments of vertebrate light sensitive rod cells. *Biophys Struct Mech* 1976;2:61-77.

45. Kuhn H, Bennett N, Michel-Villaz M, Chabre M. Interactions between photoexcited rhodopsin and GTP-binding protein: kinetic and stoichiometric analyses from light-scattering changes. *Proceedings of the National Academy of Sciences of the United States of America* 1981;78:6873-6877.

46. Arshavsky VY, Lamb TD, Pugh EN, Jr. G proteins and phototransduction. *Annu Rev Physiol* 2002;64:153-187.

47. Braisted JE, Essman TF, Raymond PA. Selective regeneration of photoreceptors in goldfish retina. *Development* 1994;120:2409-2419.

48. Tso MO, Wallow IH, Powell JO. Differential susceptibility of rod and cone cells to argon laser. *Arch Ophthalmol* 1973;89:228-234.

49. Paulus YM, Jain A, Gariano RF, et al. Healing of retinal photocoagulation lesions. *Invest Ophthalmol Vis Sci* 2008;49:5540-5545.

50. Owsley C, McGwin G, Jr., Jackson GR, Kallies K, Clark M. Cone- and rod-mediated dark adaptation impairment in age-related maculopathy. *Ophthalmology* 2007;114:1728-1735.

51. Bressler NM, Bressler SB, Fine SL. Age-related macular degeneration. *Survey of ophthalmology* 1988;32:375-413.

52. Sunness JS, Massof RW, Johnson MA, Bressler NM, Bressler SB, Fine SL. Diminished foveal sensitivity may predict the development of advanced age-related macular degeneration. *Ophthalmology* 1989;96:375-381.

53. Dimitrov PN, Robman LD, Varsamidis M, et al. Visual Function Tests as Potential Biomarkers in Age-Related Macular Degeneration. *Investigative ophthalmology & visual science* 2011;52:9457-9469.
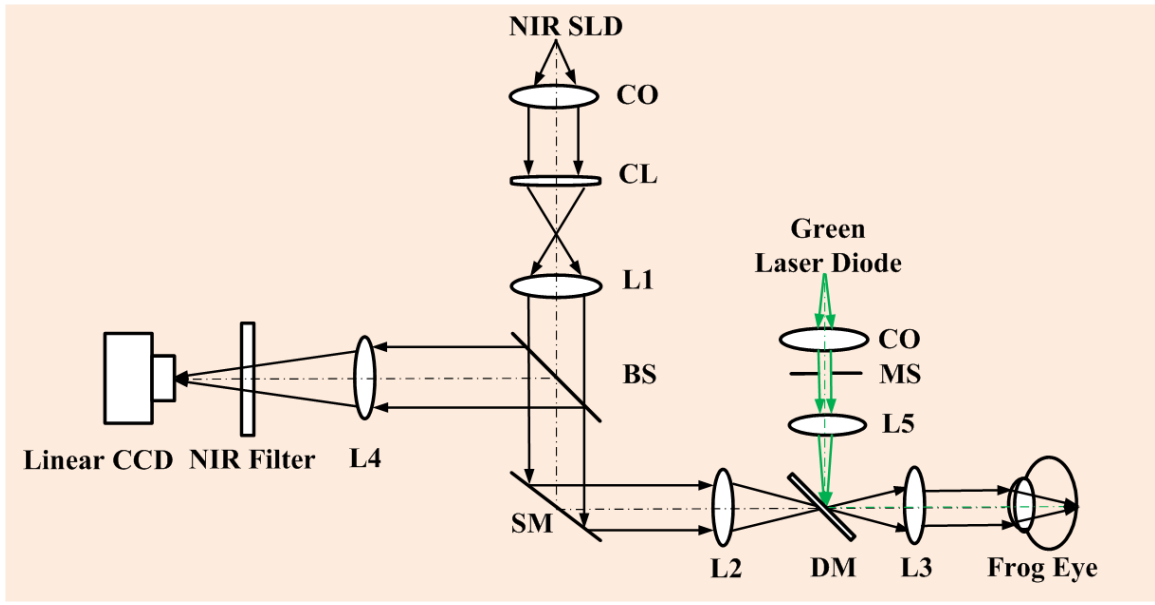
Figure 1. Schematic diagram of the line-scan confocal ophthalmoscope for in vivo IOS imaging. CO, collimator; CL, cylindrical lens; BS, beam splitter; SM, scanning mirror; DM, dichroic mirror; MS, mechanical slits; Lx, optical lenses.
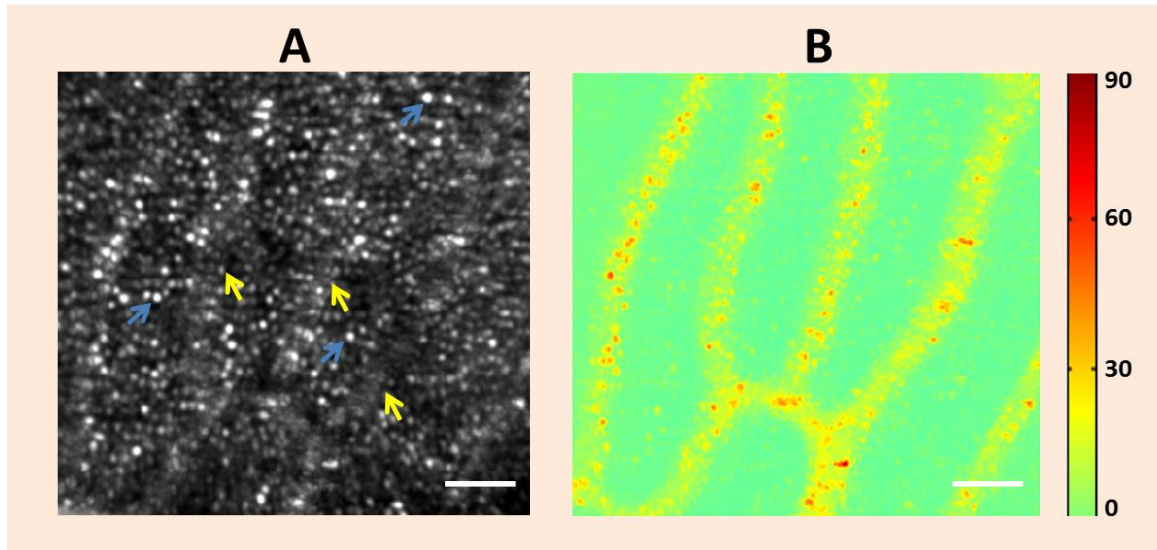
Figure 2. Representative in vivo confocal image of frog retina and 3-σ map of the pre-stimulus images to show blood vessel pattern. (A) Representative *in vivo* confocal image of frog retina. Individual blood vessels (Yellow arrowheads and Movie 1) and photoreceptors (Blue arrowheads) were clearly observed. (B) 3-σ map of the pre-stimulus images to show blood vessel pattern. Scale bars (in white) represent 50 μm.

Movie 1: A representative movie is provided to illustrate blood flow dynamics. The confocal images were recorded over 1.2 s, at the speed of 25 frames/s. Each frame consists of 400x380 pixels. Image registration was employed to compensate for eye movements in the movie.
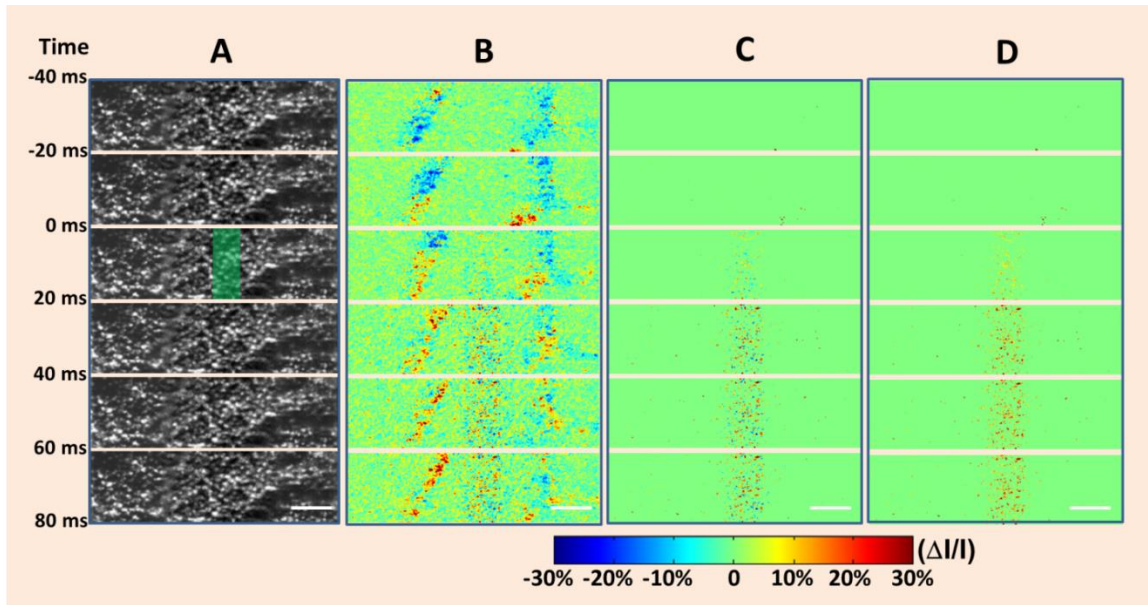
Figure 3. Confocal images of frog retina. (A) Confocal images of frog retina; each illustrated frame was the average over 20 ms. Epochs of 40 ms (pre-stimulus) and 80 ms (post-stimulus) are shown. The green rectangle in the third frame of column A indicates the size and location of the stimulus pattern. (B) The spatial IOS image sequence before filtering blood dynamics. (C) The spatial IOS image sequence after filtering blood dynamics. (D) The IOS strength distribution image sequence after filtering blood dynamics. Scale bars (in white) represent 50 µm.
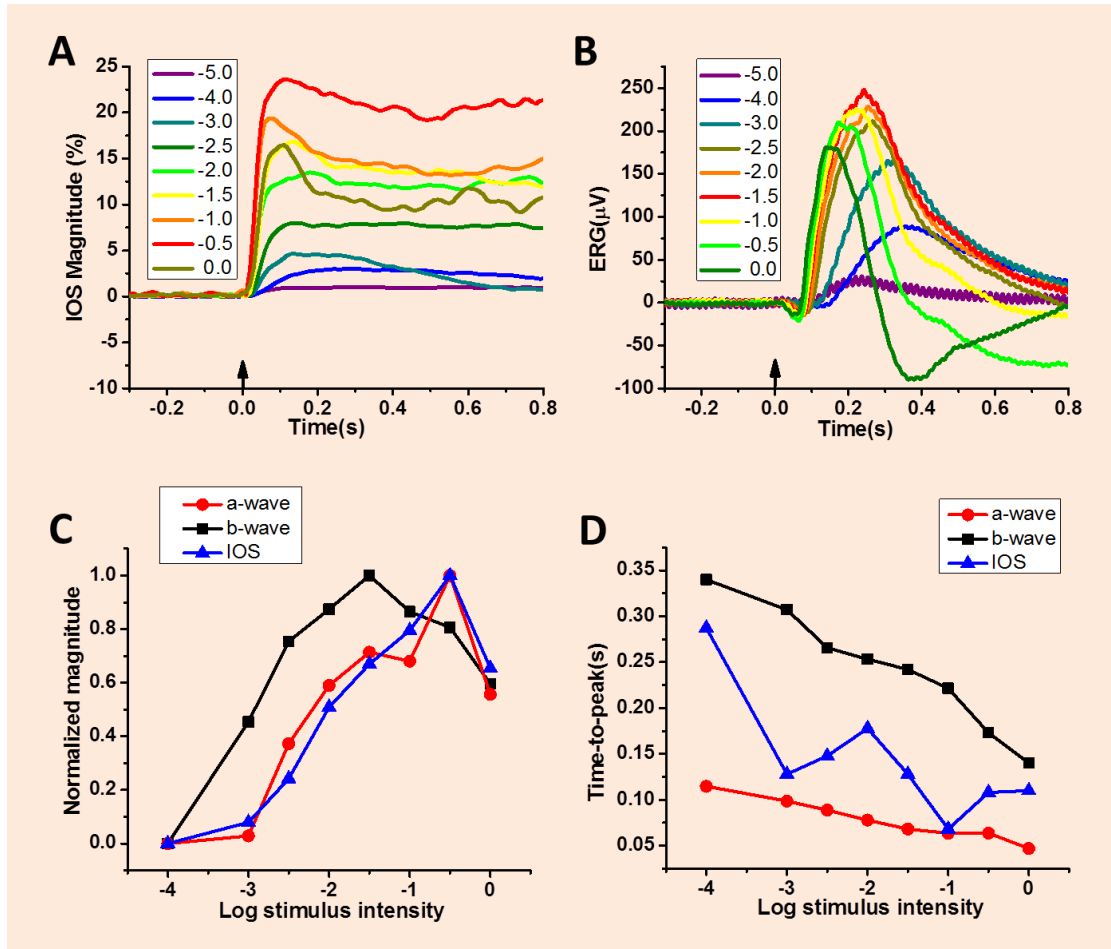
Figure 4. Comparative IOS and ERG analysis. IOS (A) and ERG (B) were recorded from the same groups of frogs. Each tracing represents an average of 4 responses evoked by light flashes of progressively brighter intensities over 5.0 log unit (log I/Imax) as indicated by the legend. (C) Normalized magnitude and (D) time-to-peak of ERG a-wave, b-wave and confocal-IOS plotted as a function of stimulus strength.
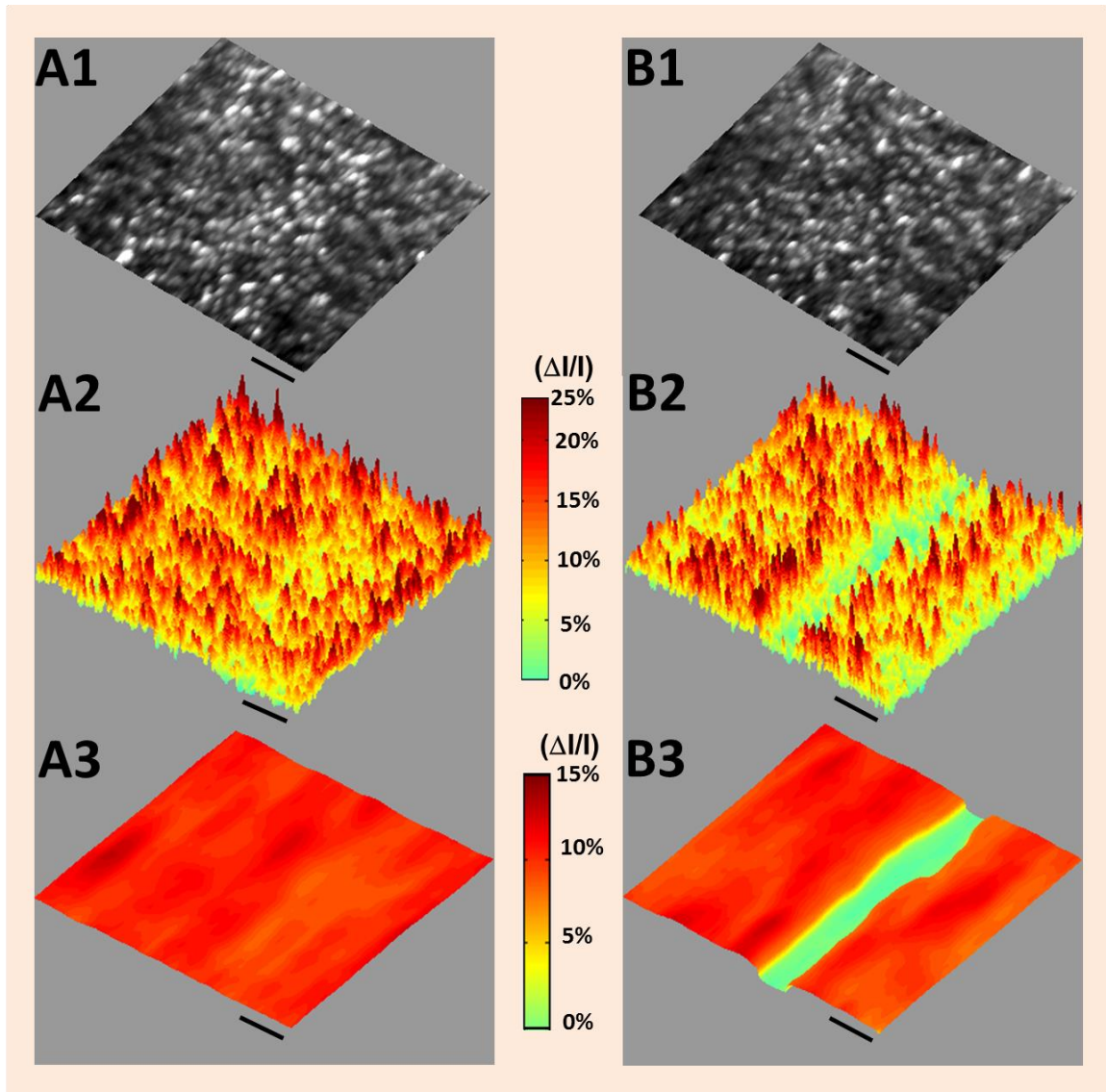
Figure 5. Structural and IOS images before and after laser injury. Retinal structure of normal frog eye (A1) and the same retinal area after laser injury (B1); Three dimension IOS image with full field stimulus before (A2) and after (B2) laser injury; The corresponding overall IOS distribution images obtained by smoothing (A3 and B3). Scale bars (in black) represent 50 μm.

IN VIVO OPTICAL COHERENCE TOMOGRAPHY OF LIGHT-DRIVEN
MELANOSOME TRANSLOCATION IN RETINAL PIGMENT EPITHELIUM

by

QIUXIANG ZHAN, RONGWEN LU, JEFFREY D. MESSINGER, CHRISTINE A.

CURCIO, VINCENZO GUARCELLO, AND XINCHENG YAO

Journal of Scientific Reports 3, 2644, 2013

Abstract

Optical coherence tomography (OCT) may revolutionize fundamental investigation and clinical management of age-related macular degeneration and other eye diseases. However, quantitative OCT interpretation is hampered due to uncertain sub-cellular correlates of reflectivity in the retinal pigment epithelium (RPE) and photoreceptor. The purpose of this study was twofold: 1) to test OCT correlates in the RPE, and 2) to demonstrate the feasibility of longitudinal OCT monitoring of sub-cellular RPE dynamics. A high resolution OCT was constructed to achieve dynamic imaging of frog eyes, in which light-driven translocation of RPE melanosomes occurred within the RPE cell body and apical processes. Comparative histological examination of dark- and light-adapted eyes indicated that the RPE melanin granule, i.e., melanosome, was a primary OCT correlate. In vivo OCT imaging of RPE melanosomes opens the opportunity for quantitative assessment of RPE abnormalities associated with disease, and enables longitudinal investigation of RPE kinetics correlated with visual function.

Introduction

This study was designed to achieve two objectives simultaneously: 1) to investigate optical coherence tomography (OCT) correlates in the retinal pigment epithelium (RPE); 2) to demonstrate the feasibility of in vivo OCT monitoring of RPE dynamics at sub-cellular level. Located posterior to the photoreceptors at the back of the eye, the RPE is a simple cuboidal epithelium attached firmly to the neurosensory retina at the apical aspect and Bruch's membrane at the basal aspect. The RPE is essential in maintaining physiological function of photoreceptors and choroidal vasculature[1, 2]. It is known that the RPE plays multiple roles including phagocytosing retinal photoreceptors [3],

manufacturing the photopigment 11-cis retinal [4, 5], transporting nutrients and new retinoid from choriocapillaris [3], and scavenging stray light [6]. RPE abnormalities can occur in eye diseases, including age-related macular degeneration (AMD)[7, 8], which is a leading cause of impaired vision and legal blindness [9, 10]. In the U.S. alone, more than 10 million people are estimated to have early AMD, and 1.75 million patients suffer visual impairment due to late AMD[11]. A key to preventing the sight-threatening damages of late AMD is reliable detection and assessment of early AMD. By providing unprecedented resolution to differentiate individual retinal layers, optical coherence tomography (OCT) may revolutionize the fundamental study and clinical management of AMD and other eye diseases [12, 13, 14, 15, 16, 17, 18]. However, quantitative interpretation of the OCT outcomes is challenging by uncertain OCT correlates to subcellular structures in RPE and photoreceptors[19, 20].

Melanin granules (i.e., melanosomes) are candidate OCT reflectivity sources in the RPE[19, 20], but direct evidence has not been provided. In this study, we selected leopard frog for testing the contribution of RPE melanosomes to OCT reflectivity. It is known that light-driven translocation of RPE melanin granules (i.e., melanosomes) can occur in frog eyes [21] and other animal species [22, 23]. Based on early histological study [21], it has been established that frog RPE melanosomes could move into the proximal ends of the RPE apical processes (microvilli) in dark-adapted retinas (Fig. 1, left). In contrast, RPE melanosomes migrate distally within the apical processes, which interdigitated with the photoreceptors, in light-adapted retinas (Fig. 1, right). The light-driven translocation of frog RPE melanosomes provided an excellent model to quantify the contribution of RPE melanin to OCT-detectable reflectivity. If the melanosome is a primary OCT correlate in

the RPE, high OCT reflectivity of the RPE band should be expected in dark-adapted retina, due to melanosomes confined in the basal RPE (Fig. 1, left). In contrast, reduced reflectivity of the RPE band and enhanced reflectivity of the photoreceptor and external limiting membrane (ELM) zone should be expected in light-adapted retina, due to melanosome translocation within the apical processes from proximal (near the RPE cell body) to distal (near the ELM) (Fig. 1, right).

We tested the hypothesis by comparing OCT scans of dark- and light- adapted frog retinas. A custom-designed spectral domain OCT (SD-OCT) was developed to provide sub-cellular resolution in both lateral (2 μm) and axial (3 μm) directions. Hyper-reflective OCT bands that encompass the RPE, photoreceptor, and ELM were quantitatively analyzed. Our observed OCT dynamics showed tight correlation with RPE melanosome migration, and the feasibility of dynamic OCT monitoring of sub-cellular RPE translocation was demonstrated for the first time.

Results

OCT imaging of dark-adapted and light-adapted frog eyes

The OCT images in Fig. 2A1-A2 were collected from two different frogs that were dark-adapted over-night. The OCT images in Fig. 2B1-B2 were collected from two different frogs with 8-hour light adaptation. Before each OCT recording, with the reference arm at a stationary position, we adjusted the position of nerve fiber layer located near 150 μm from the zero-depth position (positive delay) first. The position adjustment was based on dynamic monitoring of the reflectivity profile of the twin (real/mirror) OCT A-lines. After that, the reference arm and the sample arm were adjusted simultaneously, i.e., in the same direction and same distance, to focus the light at

the photoreceptor layer, where we observed the sharpest pattern of photoreceptor mosaic. Each B-scan image consisted of 512 A-scans. OCT reflectivity profiles averaged over 50 A-scans across whole retinal depth were superimposed on B-scan images in Fig. 2A1 (dashed yellow line), Fig. 2A2 (solid yellow line), Fig. 2B1 (dashed red line) and Fig. 2B2 (solid red line).   In dark-adapted eyes, sub-cellular resolution B-scan (i.e. cross-sectional) OCT images consistently revealed a hyper-reflective band at the RPE. The external limiting membrane (ELM) and photoreceptor inner segment ellipsoid (ISe) could be unambiguously differentiated (Fig. 2A1-A2). In comparison with OCT images of dark-adapted eyes (Fig. 2A1-A2), both reflectivity and bandwidth of the RPE band were decreased significantly in light-adapted eyes (Fig. 2B1-B2). Moreover, the ELM and ISe bands were merged together. Therefore, the ISe OCT band in the eye with light adaptation became wider compared to that in the eye with dark adaptation.

In order to verify the axial locations of individual OCT bands, en-face (i.e., projection) images of the retina/RPE were reconstructed (Fig. 2C-D). En face images (projection within 25

μm depth) of the nerve fiber layer (Fig. 2C) and photoreceptor OS (Fig. 2D) were reconstructed from the same data set of 400 B-scans. The display window and level of each enface projection image (Fig. 2C-D) was adjusted separately for a better visualization of cellular structures. In Fig. 2C, individual blood vessels were clearly observed. The photoreceptor mosaic was unambiguously shown in Fig. 2D. By superimposing the reflectivity profiles (from NFL to RPE complex) generated from Fig. 2A1-A2 and Fig. 2B1-B2, significant OCT changes were revealed only at the outer

retina/RPE; while the OCT change of inner retina (from NFL to OPL) were negligible (Fig. 2E).

In order to verify the repeatability of the observation, eight dark-adapted and eight light-adapted frogs have been used for comparative OCT imaging. Table 1 illustrates quantified thicknesses of the RPE-ISe layer (blue bars in Fig. 2A-B) and whole retina including the RPE (green bars in Fig. 2A-B) of the sixteen frogs. Statistical analysis revealed significant change of the RPE-ISe layer thicknesses ($p < .00005$, student's t-test) between dark- and light- adapted conditions. In contrast, no significant differences were observed in the retinal thicknesses ($p > 0.5$, student's t-test) between dark- and light-adapted conditions. Box charts with data overlay in Fig. 3. revealed that the thickness of the RPE-ISe layer increased in light-adapted condition compared to that in dark-adapted condition.

OCT imaging of light-to-dark transition in frog eyes

In order to verify the reliability of OCT changes correlated with light conditions, we conducted dynamic OCT imaging of a frog eye over ~ 1 hour (Fig. 4). The frog was light-adapted for 8 hours, and OCT images were captured continuously during the transition from light to dark at the same retinal location. Fig. 4A shows the cross-sectional image in light condition. After the light was turned off, the frog was maintained in the dark room for longitudinal OCT monitoring. After 1 hour in the dark room, the ELM was gradually appeared as an individual layer in Fig. 4B, which was mixed with the ISe band in Fig. 4A. Fig. 4C-F shows light intensity distribution changes in local cross-sectional images 0 min, 20 min, 40 min and 60 min later after the light-adapted eye was left in the darkness. As we can see, inner retina only changed slightly over time. In

contrast, in the outer retina, the peak of reflected light was gradually translated to the outermost layer. Basically, it took as long as 60 min for pigment to transit from light-adapted to dark-adapted position.

In order to quantify the light reflectivity change, linear scale was used in the images in Fig. 5A. The averaged reflected light changes of outer retina and inner retina were plotted in Fig. 5B. It was observed thatthe total light reflected from outer retina and inner retina were almost constant ($< \pm 7\%$ change over time) during the light-dark transition. The slight different might reflect the effect of pigment bleaching and outer segment changes correlated with retinal adaptation. Therefore, it further supports our hypothesis that the observed light changes in outer retina and RPE complex were tightly correlated with light-driven melanosome translocation.

Histological images of dark- and light-adapted frog eyes

In order to verify the light-driven melanosome translocation, histological examination of dark- and light-adapted frog eyes was conducted. Fig. 6A-B shows transmission microscopy (40X) images of 14 μm-thick cryostat sections of eyecup slices with dark (Fig. 6A) and light (Fig. 6B) adaptations, respectively. We speculate that the significant difference at the RPE/photoreceptor attributed to RPE melanosome translocation. In order to verify it, histological examination of 0.75 μm-thick eyecup slices was conducted, with improved microscopy resolution (60X). The melanosome redistribution was clearly revealed in dark- (Fig. 6C) and light-adapted (Fig. 6D) eyes. Using 6,000X transmission electron microscopy, the structure of individual melanosomes within RPE microvilli was confirmed (inserted panel in Fig. 6D).

Discussion

In summary, we employed a custom-designed SD-OCT to achieve in vivo imaging at subcellular resolution. Comparative OCT examination of dark- and light-adapted frog eyes verified that RPE melanosomes is a primary source of reflectivity. Early polarization-sensitive OCT imaging has suggested that RPE OCT signal could be attributed to RPE melanosomes [24, 25, 26, 27]. Melanosome is an organelle that synthesizes and stores melanin. In humans, the melanin determines the skin color. Besides in the RPE, It is also found in hair, the pigmented tissue underlying the iris of the eye and the brain. Melanin has a high index of refraction [28, 29], in confocal microscopy images, melanin has been shown to provide strong contrast[30]. OCT images of brain, skin and hair also indicate higher scatter or increased signal in melanin accumulated area[28, 29, 31, 32, 33].

The purpose of this study is to use the unique animal (frog) model, which possesses light-driven melanosome translocation, to test the OCT correlate (i.e. melanosomes) in retinal RPE. Our experiment results showed OCT imaging consistently revealed a hyper-reflective band at the RPE in dark-adapted retinas, which was much stronger than other hyper-reflective bands such as the ELM and photoreceptor ISe. Given the fact that melanosomes were aggregated at the apical aspect of the RPE in dark-adapted eyes (Fig. 1, left , Fig. 5A and 5C), the observed hyper-reflective OCT band observed at the RPE (Fig. 2A-B) supported the primary scatter candidacy of melanosomes on OCT imaging. When the frog eye was exposed to visible light illumination, reflectivity of the RPE band was decreased gradually. In contrast, the reflectivity of photoreceptor band, particularly the inner segment, was enhanced, and the ELM band merged with the photoreceptor IS band (Fig. 4A-B). This phenomenon was

consistent with the histological observation in light- adapted retina, in which RPE melanosome translocated within the apical processes from proximal to distal (up to the ELM) (Fig. 6B and 6D). In other words, our observed OCT dynamics associated with light changes tightly correlated with RPE melanosome redistribution shown in Fig. 1. In-depth understanding of the OCT correlates in the outer retina will pave the way for quantitative analysis of OCT outcomes.

Although light-driven melanosome translocation has not been consistently observed in human and mammal animals [34], recent study has suggested possible changes of RPE melanosomes correlated with light/dark adaptation in human eye. Moreover, RPE abnormality is a common occurrence associated with AMD[7, 8,] and RPE pigment relocation has been reported in mouse models of inherited retinopathies[28] and human patients with retinitis pigmentosa[29] and AMD[30]. In *vivo* ophthalmologic imaging of retinal and corneal morphology with an axial resolution of 1-2 μm was present for human eye imaging. Therefore, we expect that the pathological translocation of RPE melanosomes in human subjects can be quantitatively assessed by the OCT. In addition, in vivo functional OCT imaging may advance the study of RPE/photoreceptor interactions in animal models. Without the requirement of destructive histologic preparations [21], OCT imaging of the RPE/photoreceptor dynamics is easy, time- and cost-effective. Besides, functional OCT imaging of the same animals under different light conditions can be reliably implemented, without artifacts due to different samples prepared for endpoint histologic examination. Previous studies have suggested that melanosome aggregation towards the dark-adapted position could depend upon the external ionic concentration, such as the external Ca^{+2} or Na^{+} [21], as well as the elevated

intracellular cAMP [35]; while melanosome dispersion to the light-adapted position was affected by chemical messengers such as dopamine [21, 35] rather than the Ca^{+2} or Na^+ concentration. It can provide excellent models to investigate the diurnal and circadian regulation of photoreceptor and RPE physiology[36]. For example, the recognition of the role that dopamine plays in light and circadian signaling. The demonstrated *in vivo* OCT imaging will allow quantitative analysis of effects of these physiological parameters by longitudinal monitoring of animal retinas under variable pharmacological treatments.

Materials and Methods

Animal preparation: Adult northern leopard frogs (Rana Pipiens) were used in this study. The experimental procedure was approved by the Institutional Animal Care and Use Committee of the University of Alabama at Birmingham and carried out in accordance with the guidelines of the ARVO Statement for the Use of Animals in Ophthalmic and Vision Research.

In vitro histological preparation: Following over-night dark adaptation and 8-hour light adaptation, frogs were euthanized by rapid decapitation and double pithing before enucleating the eyes. After the eyes were removed from the sockets, 1-2 small holes were created by a needle at the cornea of the intact eyes, and the eyeballs were still spherical in shape. Then eyes were immersed in 4% paraformaldehyde for 3 hours and hemisected below the equator with a pair of fine scissors to remove the lens and anterior structures. After that, the complete retina-RPE-choroid-sclera complexes were transferred to 2% paraformaldehyde and 0.25% glutaraldehyde for storage. For dark-adapted frogs, procedures were conducted in a dark room with dim red illumination. After fixation,

retinas were cryoprotected in 30% sucrose, embedded in a 2/1 mixture of 30% sucrose and frozen tissue embedding media (HistoPrep; FisherScientific, Pittsburg, PA) and cryo-sectioned (14 μm sections), thaw-mounted on SuperFrost plus slides (Fisher Scientific, Pittsburg, PA) and stored at 2^0C until use. Images were obtained using a Zeiss Axioplan2 microscope, a 40X objective with numerical aperture = 0.95. Another set of eyes was post-fixed in osmium tannic acid paraphenylenediamine, dehydrated with ethanol and acetonitrile for semi-thin (0.75 μm) epoxy sections in the horizontal plane through the optic nerve[37]. Images were obtained using bright field microscopy, a 60X oil objective with numerical aperture = 1.4, and a CCD camera (Olympus XC10). High resolution (6,000X) transmission electron microscopy was also conducted to confirm the structure of individual melanosomes.

In vivo SD-OCT imaging: To compare the melanosome position differences under light and dark conditions, frogs underwent the over-night dark adaptation and 8-hour light adaptation, respectively. Before NIR (Near Infrared) OCT imaging, the frog was anesthetized through the skin when it was immersed in the tricaine methanesulfonate (TMS, MS-222) solution (500 mg/liter)[38]. After confirmation of the anesthesia, topical atropine (0.5%) and phenylephrine (2.5%) were applied to fully dilate the pupil to ~5 mm. After that, the frog was placed in a custom-built holder for OCT imaging. The holder provided six degrees of freedom to facilitate adjustment of body orientation and retinal area for OCT imaging[39].

For the experiment designed to monitor melanosome movement from light to dark, after the initial 8-hour light adaptation, the frog eyes were imaged under light condition for the first half hour at 10 min intervals. Then the eyes would be left in full darkness.

The 10 min intervals NIR retinal imaging was performed continuously for another one hour in the dark. In order to optimize the comparison between light and darkness, we imaged the identical areas in the retina over time.

SD-OCT system configuration: A schematic diagram of our SD-OCT system is illustrated in Fig. 7.   The light source used in this system is a broadband superluminescent diode (SLD; Superlum Ltd., Ireland) with a center wavelength of 846 nm, full width at half maximum (FWHM, $\Delta\lambda$) of 104 nm.   The beam from the SLD is coupled to fiber-based Michelson interferometer via a 50:50 fiber coupler (Thorlabs, Inc., USA), which split the source light into the sample and the reference arms. A fiber optic isolator (Thorlabs, Inc., USA) is employed between the SLD and the fiber coupler to exclude back reflection. The sample arm consists of an X-Y transverse galvanometer scanner and a pair of relay lens for delivering sample light to the frog retina and collecting the back-reflected sample light. The optical power entering the pupil was measured to be ~1.25 mW, which meets the safety requirements set by the American National Standards Institute (ANSI) Z136.1 limits. In the reference arm, we employed similar lenses to match the dispersion between the reference and the sample arms. Instead of a neutral density filter, a slit was used to adjust reference power without inducing extra dispersion.

The interference signal between the reference arm and sample arm was collected by the fiber coupler and delivered to a custom-built spectrometer. The spectrometer consists of an IR achromatic f=150 mm doublet lens (Thorlabs, Inc., USA) as the collimator, a 1200 line/mm transmission grating (Wasatch Photonics, Inc., USA) and rapid rectilinear lenses with two 300mm achromatic doublet lens pair (Thorlabs, Inc.,

USA). The detector is a line scan charge-coupled device camera (EV71YEM4CL2014-BA9 OCT/Spectrometer versions, E2V, NY, USA) with 2048 pixels and 14μm x 28 μm pixel sizes. The calculated spectral resolution was 0.0498 nm, which corresponds to a detectable depth range of 3.59 mm in air[73].

An image acquisition board acquired the image captured by the camera and transferred it to a computer workstation (Intel Xeon CUP, dual 2.26 GHz processor, 6 GB memory; Dell Inc., Texas, USA) for signal processing and image display. The A-line (depth scan) rate of the OCT system was set at 5 kHz. At this operating condition, the OCT sensitivity was approximately 95 dB. The numerical aperture of the system is 0.4 with depth of focus around 3.6 mm. The theoretical axial resolution was approximately 3.04 μm in air, corresponding to 2.25 μm in tissues [73] (the refractive index of the retina was approximately 1.35) and theoretical lateral resolution around 2 μm.

Author contributions

Q.X.Z. contributed to OCT construction, performed OCT imaging and data processing, and contributed to manuscript preparation. R.W.L. contributed to optical construction and data processing. J.D.M and V.D. performed histological examination. C.A.C. contributed to histological examination, experimental design, and manuscript preparation. X.C.Y conceived and supervised the project, contributed to OCT design, experimental design, data analysis and manuscript preparation.

Additional Information

ELM

Cone ISe

Rod ISe

RPE
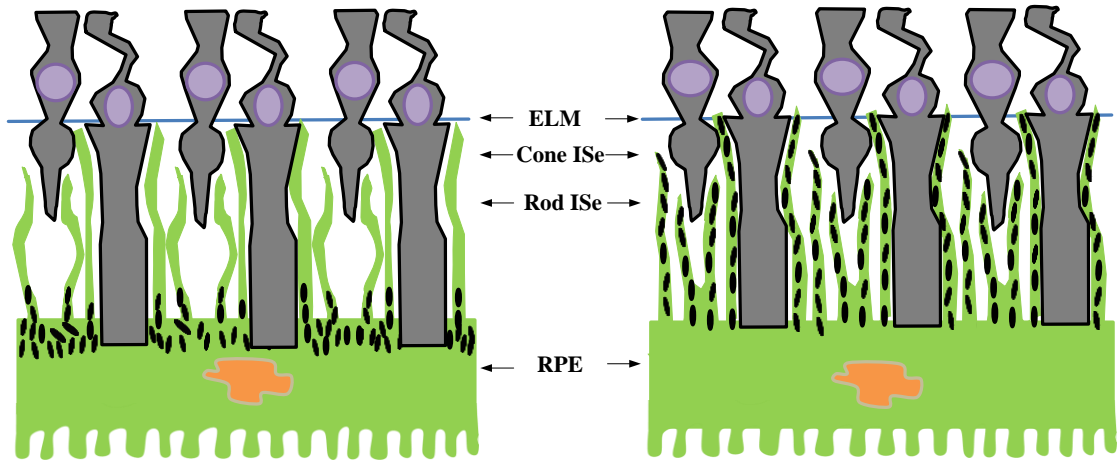
Figure 1. Cartoon illustration of melanosome position in dark-adapted (left) and light-adapted (right) frog retinas. RPE melanosomes are confined in the basal ends of the RPE cells in dark-adapted retinas; while they migrate into the apical projections in light-adapted retinas. ISe, inner segment ellipsoid.
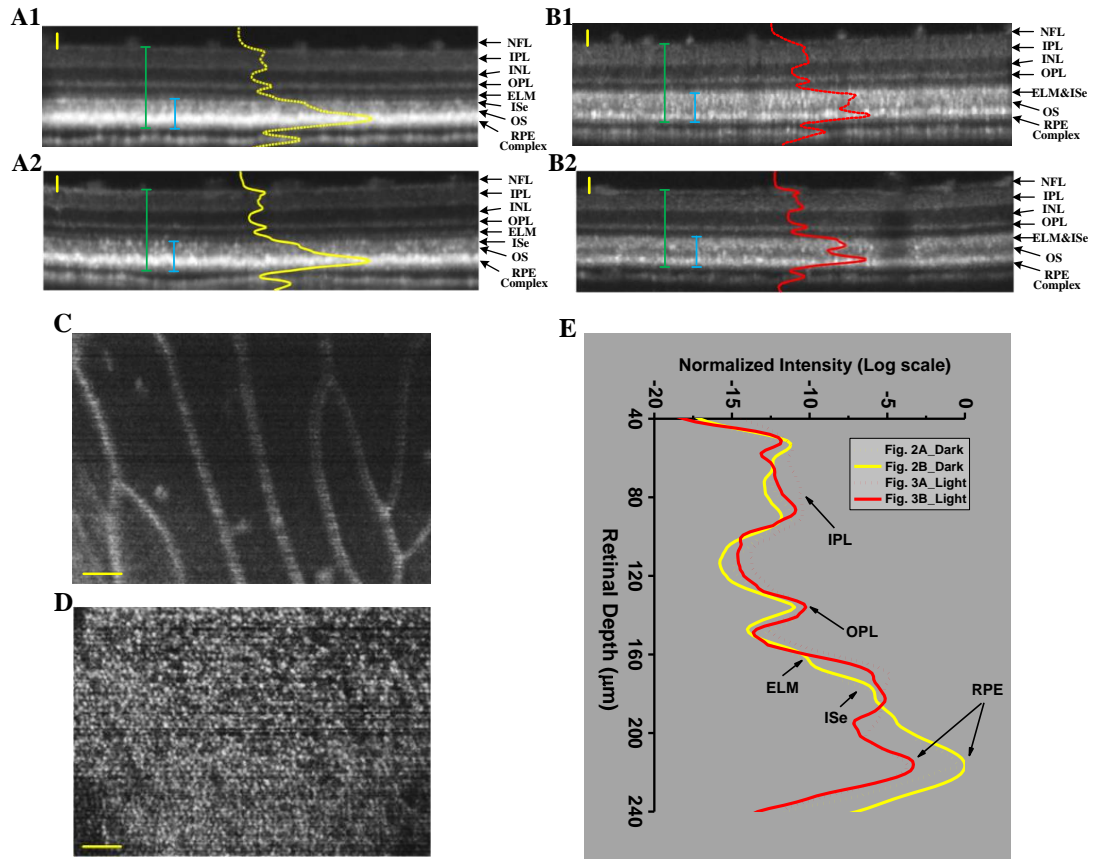
Figure 2.   Representative OCT images of dark-adapted and light-adapted frog eyes. The cross-sectional images (A1) and (A2) were collected from two separate frogs, with over-night dark-adaptation. NFL: nerve fiber layer, IPL: inner plexiform layer, INL: inner nuclear layer, OPL: outer plexiform layer, ELM: external limiting membrane, IS: inner segment, OS: outer segments and RPE: retinal pigment epithelium. The cross-sectional images (B1) and (B2) were collected from two separate frogs, with 8-hour light-adaptation. The green bars measured the retinal thickness with RPE complex included and the blue bars measured the RPE-ISe layer thickness; (C) Reconstructed en-face projection of blood vessels obtained nearby the NFL layer in Fig. 2A1; (D) Reconstructed   en-face projection   of   photoreceptor   mosaic   obtained   from   the

photoreceptor layer in Fig. 2A1. The contrast and brightness were adjusted for best visualization. (E) OCT reflectivity profiles of dark- (yellow) and light- (red) adapted frog eyes. The two yellow traces correspond to the two dark-adapted images in Fig. 2A1-2A2. The two red traces correspond to the two light-adapted images in Fig. 2B1-B2. Scale bars indicate 50 μm.

	Light-adapted			Dark-adapted	
Frog	RPE-ISe thickness (µm)	Retina thickness(µm)	Frog	RPE-ISe thickness (µm)	Retina thickness(µm)
1	75	216	9	70	212
2	76	212	10	74	218
3	75	211	11	68	213
4	74	223	12	67	216
5	77	220	13	68	220
6	79	209	14	73	216
7	78	222	15	68	203
8	77	220	16	70	220

Table 1. Summary of 16 frogs under dark- and light- adapted conditions.
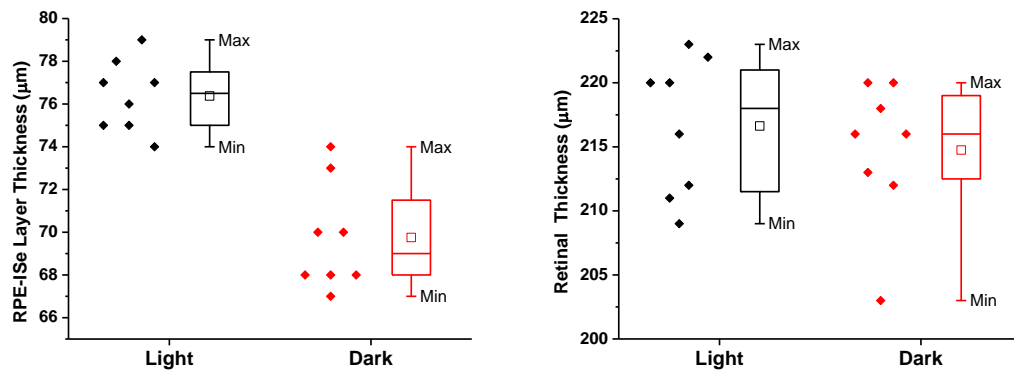
Figure 3. Box charts of RPE-ISe layer thickness (left) and retinal thickness (right) with data overlay. Box=25th and 75th percentile.
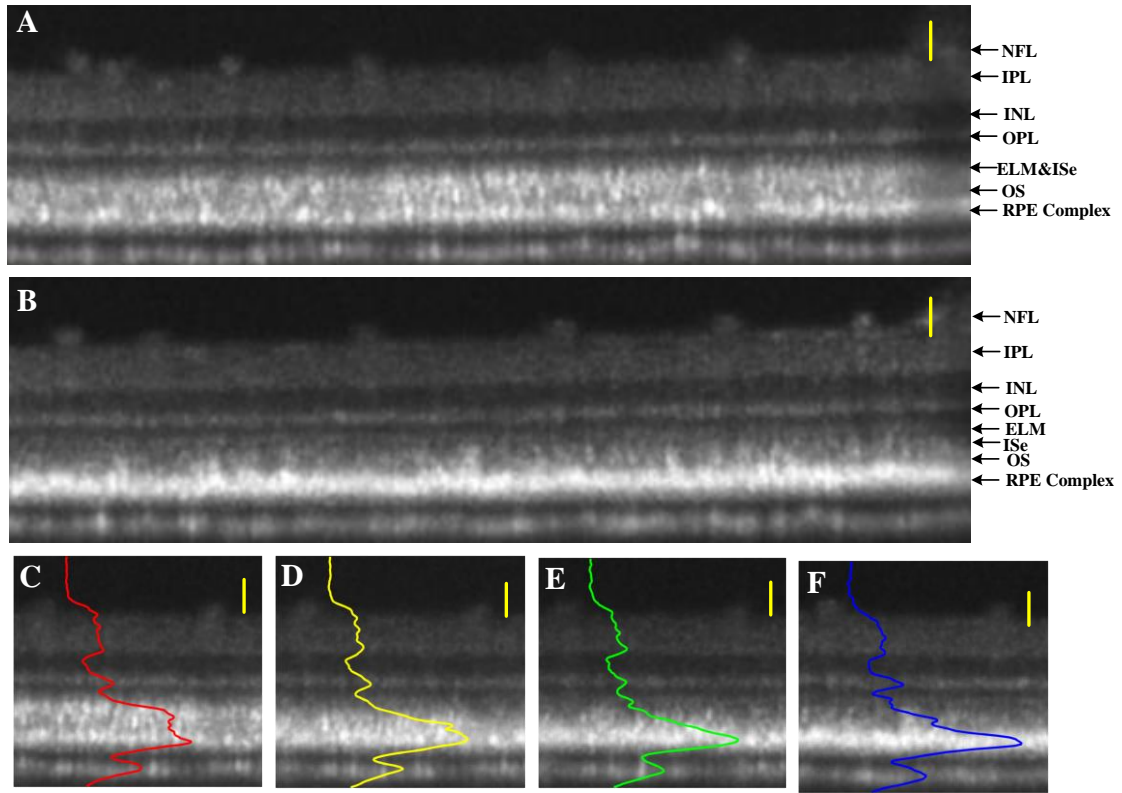
Figure 4. OCT imaging of retina during light-to-dark transition. (A) Cross-sectional image of light-adapted frog eye; (B) Cross-sectional image at the identical location in the retina 1 hour later after maintained in the darkness. Panels C-F illustrate the same local areas of the cross-sectional images recorded at 0-min, 20-min, 40-min and 60-min after the light-adapted (A) retina was left in the darkness. Scale bars indicate 50 μm.
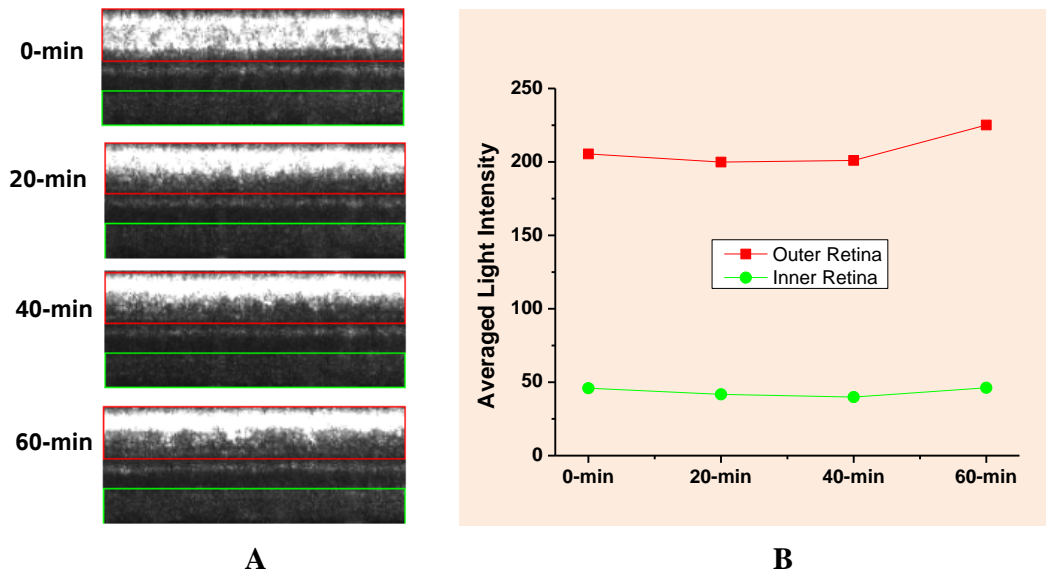
Figure 5. Light reflectivity change of inner and outer retina during light-to-dark transition. (A) Red box indicates outer retina area with RPE complex included and green box indicates inner retina area; (B) the averaged reflectivity change of inner and outer retina during light-to-dark transition.
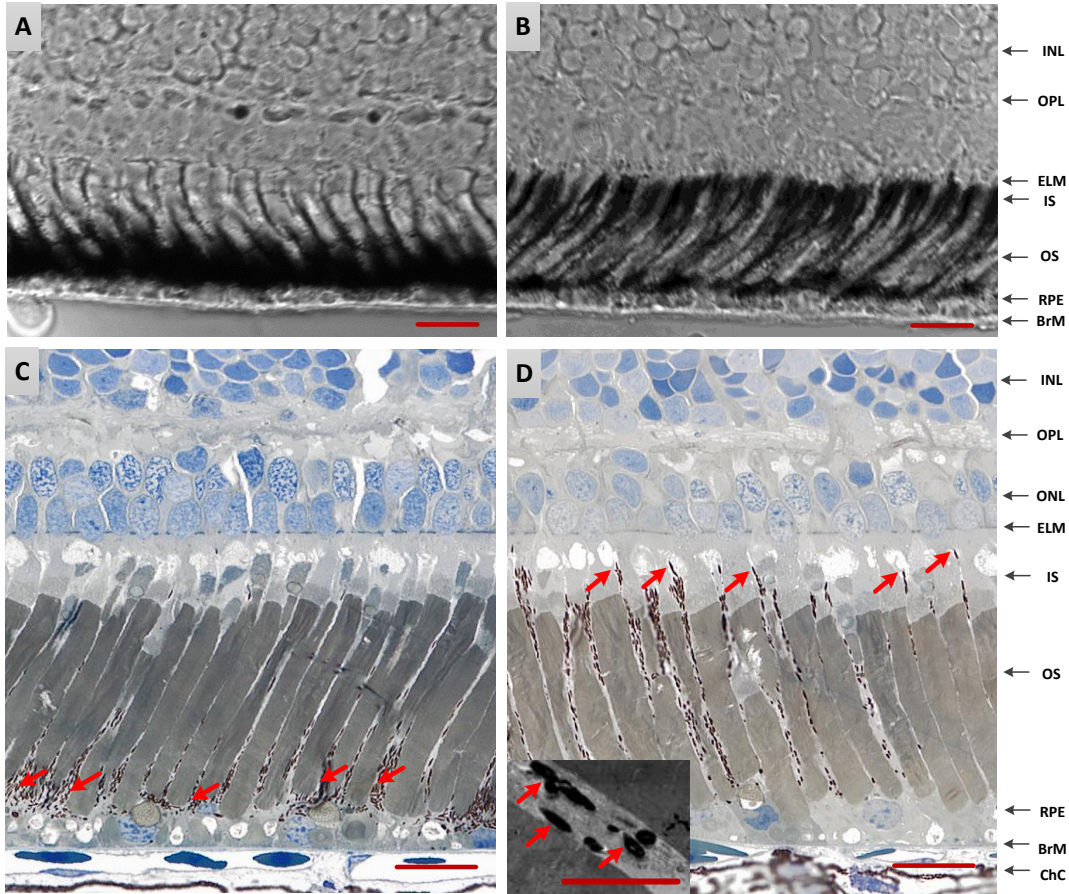
Figure 6. Histological images of dark- (A, C) and light-adapted (B, D) frog eyes. For A and B, images unstained 14 μm thick frozen sections were obtained by bright field microscopy (40X) with N.A. 0.95 objective; For C and D, section thickness is 0.75 μm, and images were obtained by bright field microscopy (60X) with N.A. 1.4 objective. The inset to panel D shows individual melanosomes (arrows) within apical processes of RPE, flanked by photoreceptor outer segments, as obtained by transmission electron microscopy (6000X original magnification). Scale bars indicate 25 μm in A-D and 5 μm for D inset.
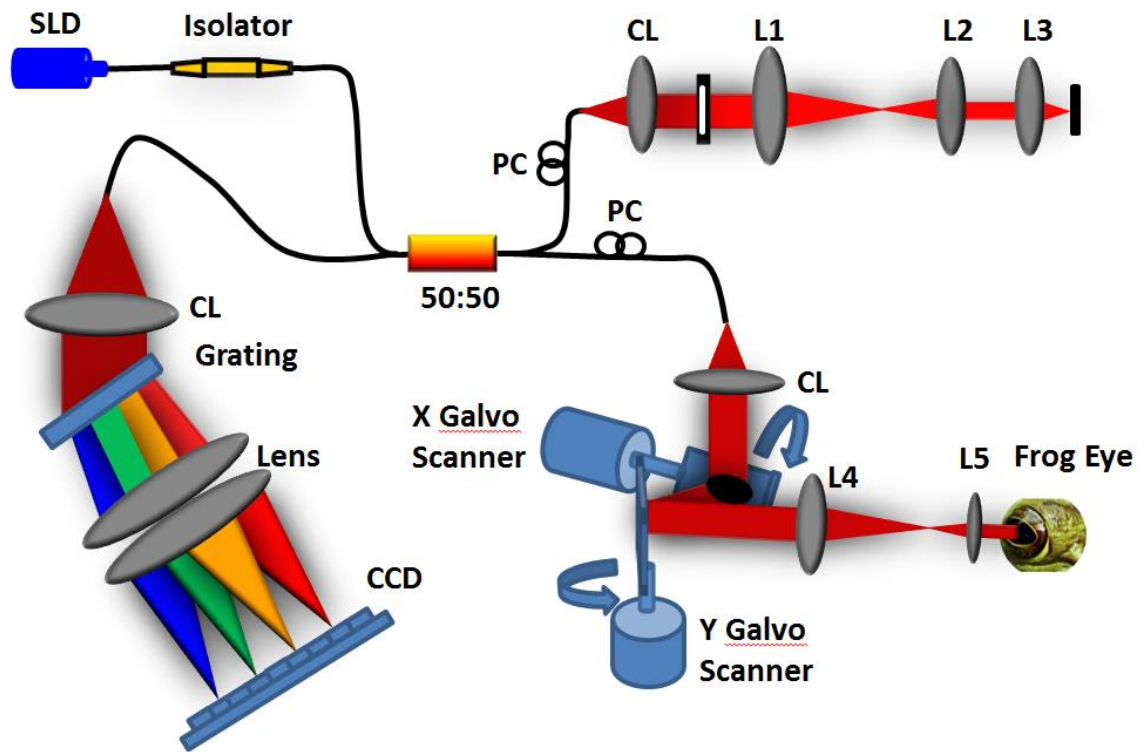
Figure 7. Schematic diagram of the experimental setup. Schematic of the SD-OCT system at 846 nm designed to acquire in vivo images of the retina of the frog eye. SLD: superluminescent diode, PC: polarization controller, CL: collimation lens, L1–L5: lens.

FUNCTIONAL OPTICAL COHERENCE TOMOGRAPHY ENABLES *IN VIVO*
PHYSIOLOGICAL ASSESSMENT OF RETINAL ROD AND CONE
PHOTORECEPTORS

by

QIUXIANG ZHAN, RONGWEN LU, BENQUAN WANG, JEFFREY D. MESSINGER,

CHRISTINE A. CURCIO, AND XINCHENG YAO

Abstract

Transient intrinsic optical signal (IOS) change has been observed in retinal photoreceptors, promising a unique biomarker to revolutionize eye disease detection. However, clinical deployment of IOS imaging is challenging due to unclear IOS sources and limited signal-to-noise ratio (SNR). Here, by developing a high spatiotemporal resolution optical coherence tomography (OCT) and applying adaptive algorithm for IOS processing, we are able to record robust IOSs from single-pass measurements. Transient IOSs, which might reflect early stage of light phototransduction, are consistently observed at photoreceptor outer segment almost immediately (<4 ms) after retinal stimulation. Comparative studies of dark- and light-adapted retinas demonstrate the feasibility of functional OCT mapping of rod and cone photoreceptors, promising a new method for early disease detection and improved treatment evaluation of age-related macular degeneration (AMD) and other eye diseases that can cause photoreceptor damage.

Introduction

Many eye diseases, such as age-relate macular degeneration (AMD), retinitis pigmentosa (RP), glaucoma and diabetic retinopathy (DR) can produce retinal damage that is associated severe vision loss including legal blindness. It is well known that different diseases target different retinal cell types. In principle, physiological abnormalities in diseased cells can occur before neuron loss and corresponding retinal thickness changes are detectable. Therefore, functional evaluation of physiological integrity of retinal cells is important for early disease detection and reliable treatment management. Psychophysical methods, such as Amsler grid test, visual acuity[1,2] and

hyperacuity perimeter[3], are practical in clinical applications, but they involve extensively higher order cortical processing. Therefore, they do not provide exclusive information on retinal function and lacks the sensitivity in detecting early disease detection. Electrophysiological methods, such as focal electroretinography (ERG) [4-8], multifocal ERG[9,10] and dark adaptometry[11,12] [13], allow objective assessment of retinal function. However, understanding the relationship of the low-spatial resolution of ERG to localized morphological changes is complicated.

Stimulus-evoked fast intrinsic optical signal (IOS) imaging promises an alternative to ERG for objective measurement of retinal physiological function[14,15]. Because functional IOS images are constructed through computer-based dynamic differentiation of retinal images recorded at pre- and post-stimulus periods [16], concurrent structural and functional assessment can be naturally achieved at high resolution. Conventional fundus cameras[17-22], adaptive optics [23-25] and optical coherence tomography (OCT) [26-28] have been explored for IOS imaging. However, reliable mapping of fast IOSs that have time courses comparable to retinal electrophysiological kinetics is still challenging [23]. Using a rapid line-scan confocal imager, we recently demonstrated *in vivo* IOS imaging of frog retinas with high lateral resolution[14,29]. Comparative IOS and ERG experiments revealed a close correlation between confocal IOS and retinal ERG a-wave, which has been widely used to evaluate photoreceptor function. The photoreceptor mosaic we observed from the confocal imager is known to reflect the waveguide properties of outer segment (OS). Therefore, we speculated that the confocal IOS might be mainly from the photoreceptor OS. However, due to the limited axial resolution of the

confocal system, it has been challenging to accurately verify the axial location of the IOS source in the retina which consists of multiple layers.

In order to achieve subcellular identification of IOS sources, a custom-designed OCT is developed with sub-cellular spatial resolution in three dimensions (3.0 μm x 3.0 μm x 3.0 μm) and millisecond temporal resolution (500 Hz). An adaptive algorithm is developed to achieve high signal to noise ratio (SNR) in IOS processing. A animal model (*Rana Pipiens*), that has rod and cone photoreceptors stratified into different retinal depths (Fig. 1), is selected for this study[30]. As shown in Fig. 1, cone OS is almost at the level of the inner segment ellipsoid (ISe) of red rods. Transient IOS, which might reflect early stage of light phototransduction, is consistently observed at photoreceptor OSs almost immediately (<4 ms) after retinal stimulation. Comparative studies of dark- and light-adapted retinas demonstrate the feasibility of functional OCT mapping of rod and cone photoreceptors.

Results

High resolution OCT guided by combined fundus camera

The custom designed SD-OCT system, configured with retinal stimulator and fundus camera, is employed for functional IOS imaging of anesthetized frogs. The integrated fundus camera can provide real time enface mapping (Fig. 2a) to guide transverse location of OCT B-scan recording (Fig. 2b). As shown in Fig. 2a, blood vessels around the optical nerve head (ONH) can be clearly observed, and thus enables easy localization of OCT B-scan required for IOS recording. Fig. 2b illustrates an OCT B-scan image across the ONH. Fig. 2c shows comparative OCT and histological image of

frog retina with individual layers labeled[31]. The custom-designed OCT clearly provides sub-cellular resolution to separate photoreceptor outer/inner segments from other retinal layers and the supporting tissues such as choroid and sclera (Figure 2c).

Spatiotemporal characteristics of fast IOSs

Figure 3 represents typical IOS images evoked by a 10 ms visible light (green) flash (Supplementary Movie 1). As shown in Fig. 3a, transient IOSs are predominantly observed at outer retina. Combined IOS map (functional image) and OCT B-scan image (structural image) reveal photoreceptor OS as the major IOS source in retinal photoreceptors, although slight IOSs are occasionally observed at photoreceptor ISe and RPE-Bruch's membrane complex (Fig. 3b). We speculate that the IOSs observed at ISe and RPE bands might attribute to, at least be partially affected by, cone and rod OS, respectively. In order to better understand anatomic sources of these IOSs around the photoreceptor layer, comparative OCT-IOS and histological images of outer retina are shown in Fig. 3e. Retinal cone photoreceptors in the histology image are highlighted with green and red dotted circles. As shown in Fig. 3e, OS of some cones are located at the level of rod ISe section, while OS of some rods can penetrate further sclerally into the RPE, which is consistent to the observation in Fig. 130. Therefore, it is reasonable to occasionally observe IOSs at ISe and RPE layers, even if the OS is the only IOS signal source at outer retina.

As shown in Fig. 3a and Fig. 3b, both positive and negative IOSs are consistently observed in adjacent retinal areas, which further confirm that high resolution is essential for functional IOS imaging. Without necessary spatial resolution to separate localized positive and negative IOSs, the IOS sensitivity will be degraded 32. Given the excellent

OCT resolution in both transverse (3 μm) and axial (3 μm) directions, high sensitivity is ensured to achieve robust IOS recording from single-pass measurements, without average requirement of multiple trials. Fig. 3c illustrates temporal dynamics of averaged positive and negative IOSs. It is observed that both positive and negative IOSs occur within 10 ms, with similar time courses (Fig. 3c). Since the OCT frame speed is set at 100 Hz, with frame size of 140 pixels (lateral) x 200 pixels (axial), for the experiment in Fig. 3, it is not possible to measure the actual onset time which is obviously shorter than the 10 ms interval. In order to characterize the onset time of the observed IOSs, the OCT frame speed is increased to 500 Hz, with reduced frame size (40 x 200 pixels), for the experiment in Fig. 4. With 2 ms temporal resolution, the IOSs can be unambiguously detected as early as 4 ms (Fig. 4c). The overall time courses are similar between 100 Hz (Fig. 3b) and 500 Hz (Fig. 4b) IOSs, but the SNR of the 100 Hz (20 kHz line rate) IOSs is slight better than that of 500 Hz (32 kHz line rate) IOSs because the higher A-line rate, resulting in a shorter exposure time, is employed with 500 Hz frame rate.

In order to further characterize time courses of positive and negative IOSs, Fig. 4d-e shows representative IOSs of individual pixels. It is observed that localized IOSs can have different onset times. Some of these IOSs are very fast (Figs. 4d1, d3, d5, e1 & e3), while others are relatively slow (Figs. 4d2, d4, d6 & e2). The overall temporal curves are also variable. Some of them can be sustained at the peak value (Figs. 4d1, d3, e1 & e2), while others are gradually recovered to baseline (Fig 4d5 & 3d6). Figs. 4d1-d2 represent the pixels from the same axial depth (y=107) but at adjacent pixel, different time courses are observed. The IOS at the position (x=31, y=107) increases rapidly upon stimulus and reaches the peak within 200 ms. While the IOS at the position (x=32, y=107)

increases almost linearly after the stimulus.

With short flash (10 ms) stimulation, transient IOSs are observed at outer retina (Figs. 3 and 4). In contrary, prolonged (500 ms) stimulation evoked IOSs at both outer and inner retinal layers (Fig. 5 and supplementary Movie 2). As shown in Figs. 5a3, a4 and b2, early phase IOSs are consistently confined in the outer retina, i.e., photoreceptor OS. After 1-2 s, later phase IOSs can spread into inner retina (Figs. 5a5, a6, a7, b3 and b4). In Figs. 5c1-c5, averaged IOSs at individual retinal layers consistently reveal that the IOSs from photoreceptor OS occur immediately after the stimulus onset. However, the onset time of IOSs at other layers, such as IPL and OPL is delayed to ~1.5 s.

Comparative IOS imaging of rod and cone photoreceptors

In order to demonstrate the potential of functional IOS imaging of rod and cone functions, comparative experiments are conducted with variable background light controls. In dark condition, transient IOSs are observed in both cone and rod OS (Figs. 6a1-a3 and supplementary movie 3). Combined light reflectance (OCT B-scans) and IOS distribution curves reveal similar signal densities across the photoreceptor OS and slight IOSs at ISe and RPE-Bruch's membrane complex regions. In contrary, under light condition (~200 cd·s/m^2), the IOS distribution pattern is significantly changed. It is observed that major signals are confined around the cone OS area (Figs. 6b1- b3 and supplementary movie 4). The light intensity profile of the outer retina is also changed dramatically (Fig. 6) due to melanosome translocation[33]. The IOS differences under dark and light conditions demonstrate the potential of functional IOS mapping of rod and cone systems, and provide additional evidence to support that the transient IOSs in retinal photoreceptors might be attributed to the OS, i.e., the center of phototransduction.

Discussion

In summary, a custom-designed SD-OCT system with fundus monitor and retinal stimulator is employed to achieve *in vivo* structural and functional imaging of the frog retina at subcellular resolution. Unprecedented temporal resolution is achieved at 2 ms to reveal robust IOS as early as 4 ms after retinal stimulation. High spatiotemporal resolution instrument and adaptive data processing algorithm ensure high SNR of single-pass measurements, and thus to allow robust IOS imaging without the requirement of averaging multiple experiments. Combined OCT-IOS (structural-functional) images (Figs. 3b, 4a, 5a2 & b2) allow precise identification of anatomic sources of IOSs. With visible flash (10 ms) stimulation, fast IOSs is predominantly confined at outer retina, particularly in the photoreceptor OS. We speculate that the IOSs observed at ISe and RPE bands might attribute to, at least be partially affected by, cone and rod OS, respectively. As illustrated in Fig.1, a previous study by Nilsson SE [30] on the retinal photoreceptors of the leopard frog retina (Rana Pipiens), the same type of frog used in our study, shows clearly four types (red rod, green rod, single cone and double cone) of photoreceptors. More than half of the photoreceptors are red rods, agreeing with the histological image in Fig. 2c. They lined up well with each other and their ISe might form the second band while OS tip and apical processes of RPE form the IZ (Interdigitation zone) in OCT B-scan image. The green rods take up only 8% of the total photoreceptors and they are often somewhat longer than red rods. Therefore, their outer segments penetrate further into RPE, which probably contribute to the fast IOSs observed in the RPE complex region. For cone photoreceptors, their OS length is much shorter than rods. The single cones, making up around 20% of total photoreceptors, are shortest, and their OS end almost at

the level of the ISe of red rod. This indicates that the fast IOSs in the ISs band may originate from the OS of single cones.

Quantitative analysis of fast IOSs from individual pixels (subcellular scale) reveals varied time courses and different signal polarities (Fig. 4). Positive and negative signals are mixed together, both containing fast and slow components. One possible reason is due to localized differences in light absorption efficiency. Although the stimulus light is optimized for uniform illumination, it is impossible to ensure equal light absorption for individual photoreceptors due to the complexity of photoreceptor lengths, locations and spectral sensitivities. In addition, there are multiple factors that may affect the observed IOSs. Previous studies with isolated photoreceptor OS and isolated retinas have demonstrated transient IOSs associated with phototransduction[34-36]. Both binding and release of G-proteins to photoexcited rhodopsin might contribute to the positive (increasing) and negative (decreasing) IOSs[35]. Localized biochemical processes might also produce non-homogeneous light intensity changes, i.e. positive and negative signals mixed together.

Comparative study of dark- and light-adapted retinas demonstrates the feasibility of functional OCT mapping of rod and cone photoreceptors, promising a revolutionary approach to advance the study and diagnosis of eye diseases that can cause photoreceptor dysfunction, of which age-related macular degeneration (AMD) is the most prevalent. It is estimated that 33 million people worldwide experience AMD-associated vision impairment [37]. In the U.S. alone, at least 1.75 million people were estimated to have advanced AMD [38,39]; and more than 10 million people are estimated to have early AMD. Currently, there is no outright cure for the retinal degenerative disease that produces

irreversible damage to photoreceptors and RPE. A key strategy for preventing vision loss due to late AMD is to preserve function and be vigilant for changes in early AMD signifying progression. Therefore, early detection is essential in preventing (or at least slowing) late AMD[37,40]. Structural biomarkers, such as drusen and pigmentary abnormalities in the macula, have provided valuable information for AMD diagnostics. However, an examination of fundus morphology alone may be insufficient [41]. Moreover, rods are more vulnerable than cones in early AMD[42,43]. Currently, there is no established strategy to allow objective assessment of localized rod dysfunction at high resolution, e.g., 50 μm, for linking localized physiological and morphological abnormalities in early AMD. We anticipate that further development of the functional OCT-IOS will pave the way toward quantitative assessment of rod and cone photoreceptors.

Although short flash (10 ms) stimulation evoked transient IOSs predominately at outer retina (Figs. 3 and 4), prolonged (500 ms) stimulation evoked additional IOSs at inner retina, with a delayed time course (1.5-2 s). The delayed IOS response at inner retina is consistent to our early study of living retinal tissue[44]. We speculate that the observed IOSs at inner retina may involve complications of nonlinear information processing and retinal adaptation mechanisms. Further investigation is required to achieve in depth understanding of the IOS sources and mechanisms at inner retina, which may lead to a new method to advance the study and diagnosis of Glaucoma and other eye diseases that may affect inner retinal dysfunction.

Materials and Methods

Animal preparation: Adult northern leopard frogs (Rana Pipiens) are used in this study. Before NIR (Near Infrared) OCT imaging, the frogs are anesthetized through the

95

skin when they are immersed in the tricaine methanesulfonate (TMS, MS-222) solution (500 mg/liter)[45]. After confirmation of the anesthesia, the pupils are fully dilated with topical atropine (0.5%) and phenylephrine (2.5%). After that, the frog is placed in a custom-built holder for OCT imaging. The holder provided six degrees of freedom to facilitate adjustment of body orientation and retinal area for OCT imaging[14]. The experimental procedure has been approved by the Institutional Animal Care and Use Committee of the University of Alabama at Birmingham and carried out in accordance with the guidelines of the ARVO Statement for the Use of Animals in Ophthalmic and Vision Research.

Data Analysis: The raw OCT B-scan images are reconstructed with linear scale. Raw B-scan images are registered to compensate for eye movements before IOS calculation. The registration is composed of three steps. First, we use the method of principle component analysis (PCA) to evaluate the rotation of retinal layers thus to compensate for the torsional movement of the eye[46]. Before applying PCA, discrete curve evolution (DCE) [47] is employed to find a threshold value to separate hyper-reflective signals from the background. Implementation of PCA on two-dimensional coordinates of those hyper-reflective signals yields two orthogonal components, one denoting the direction parallel to the retinal layers, while the other perpendicular to retinal layers. Therefore, we can compensate for the rotational movement after the rotation angle of the retinal layers is known. The second step is to apply the localized normalized cross correlation (NCC) to correct large scale displacements. Dynamic blood vessel movements can corrupt the accuracy of the NCC method. Therefore, we only choose a small localized area without contamination of big blood vessels for estimating image

displacement through NCC. The NCC method can only estimate the integral displacements. Therefore, we use centroids of hyper-reflective landmarks to compensate for fine (i.e., sub-pixel) displacements, which is the third step of image registration. Because of the high lateral resolution of our system, the second hyper-reflective OCT band at the outer retina becomes granular rather than continuous, which enables us to select a small area containing only one hyper-reflective granule. After the granule is segmented from the background using histogram-based methods, the centroid of this granule over time can be obtained, which allows us register images with sub-pixel accuracy. Movies showing the images before and after registration could be assessed online (Supplementary Movie 5&6).

Basic procedures of IOS data processing are described as follows: a high threshold is used to define stimulus-evoked IOS in the retinal area. The pixel (x, y) is negative signal pixel if its light intensity is less than the mean below three standard deviations for five times continuously,

$$\text{I}_{t_i}(x,y), \text{I}_{t_{i+1}}(x,y), \text{I}_{t_{i+2}}(x,y), \text{I}_{t_{i+3}}(x,y), \text{I}_{t_{i+4}}(x,y) < \bar{\text{I}}(x,y) - 3\sigma(x,y)$$

Similarly, the pixel (x, y) is positive signal pixel if its light intensity is greater than the mean above three standard deviations for five times continuously,

$$\text{I}_{t_i}(x,y), \text{I}_{t_{i+1}}(x,y), \text{I}_{t_{i+2}}(x,y), \text{I}_{t_{i+3}}(x,y), \text{I}_{t_{i+4}}(x,y) > \bar{\text{I}}(x,y) + 3\sigma(x,y)$$

The time interval between t_i and t_{i+1} is 10 ms for 100 Hz frame rate. For the total recording time of 1.2 s (pre-stimulus 0.3 s and post-stimulus 0.9 s), the range for t_i is: $0 < t_i < 1.16$ s. In this way, we can generate the IOS distribution map with either positive or negative signals. The averaged IOSs are calculated based on those selected signals rather than the whole area, which can greatly increase the SNR. As showed in Fig.

7, if the traditional IOS processing method is used, the SNR of IOSs are inferior to those with adaptive IOS processing algorithm applied. In addition, the magnitudes of IOSs (positive and negative) are 10 times smaller (Fig. 7b).

Experimental setup: A schematic diagram of the custom-designed SD-OCT system with fundus camera and retinal stimulator is illustrated in Fig. 8. The light source used in the OCT system is a broadband superluminescent diode (SLD; Superlum Ltd., Ireland) with a center wavelength of 846 nm, full width at half maximum (FWHM, $\Delta\lambda$) of 104 nm. The theoretical axial resolution of the OCT system is 3.04 μm. The axial resolution experimentally measured is approximately 4 μm in air, corresponding to 3 μm in tissues[48] (the refractive index of the retina is approximately 1.35). The size of the light beam on the cornea is 2.1 mm and the estimated lateral resolution is around 3 μm. For fundus imaging subsystem, the light source is a NIR light-emitting diode (LED). A multi-mode optical fiber is used to couple the light into the lens. The optical power entering the pupil is measured to be ~1.5 mW, which meets the safety requirements set by the American National Standards Institute (ANSI) Z136.1 limits. The spectrometer consists of an IR achromatic f=150 mm doublet lens (Thorlabs, Inc., USA) as the collimator, a 1200 line/mm transmission grating (Wasatch Photonics, Inc., USA) and rapid rectilinear lenses with two 300mm achromatic doublet lens pair (Thorlabs, Inc., USA). The detector is a linear charge-coupled device (CCD) camera (EV71YEM4CL2014-BA9 OCT/Spectrometer versions, E2V, NY, USA) with 2048 pixels and 14μm x 28 μm pixel sizes. The A-line (depth scan) rate of the OCT system is set at 20 kHz for 100 Hz frame rate and 32 kHz for 500 Hz frame rate. The visible light stimulus is produced by a single-mode fiber coupled 532 nm DPSS laser module (FC-532-020-SM-APC-1-1-ST;

RGBLase LLC, Fremont, CA). Estimated stimulus flash intensity is 5×10^5 photons/μm^2/ms (5×10^6 photons/μm^2 for 10 ms) at the retina.

Acknowledgements

Author contributions

Q.X.Z. performed OCT imaging and data processing, contributed to manuscript preparation. R.W.L. contributed to data processing. B.Q.W. contributed to OCT experiment. J.D.M performed histological examination. C.A.C. contributed histological examination and manuscript preparation. X.C.Y conceived and supervised the project, contributed to experimental design, data analysis and manuscript preparation.

References

1. Klein, R., Wang, Q., Klein, B.E., Moss, S.E. & Meuer, S.M. The relationship of age-related maculopathy, cataract, and glaucoma to visual acuity. *Invest. Ophthalmol. Vis. Sci.* **36**, 182-91 (1995).

2. Siderov, J. & Tiu, A.L. Variability of measurements of visual acuity in a large eye clinic. *Acta Ophthalmol. Scand* **77**, 673-6 (1999).

3. Loewenstein, A. et al. Replacing the Amsler grid: a new method for monitoring patients with age-related macular degeneration. *Ophthalmol.* **110**, 966-70 (2003).

4. Seiple, W.H., Siegel, I.M., Carr, R.E. & Mayron, C. Evaluating macular function

using the focal ERG. *Invest. Ophthalmol. Vis. Sci.* **27**, 1123-30 (1986).

5. Vaegan et al. Macular electroretinograms: their accuracy, specificity and implementation for clinical use. *Aust. J. Ophthalmol.* **12**, 359-72 (1984).

6. Fish, G.E. & Birch, D.G. The focal electroretinogram in the clinical assessment of macular disease. *Ophthalmol.* **96**, 109-14 (1989).

7. Binns, A. & Margrain, T.H. Development of a technique for recording the focal rod ERG. *Ophthalmic. Physiol. Opt.* **26**, 71-79 (2006).

8. Binns, A. & Margrain, T.H. Evaluation of retinal function using the dynamic focal cone ERG. *Ophthalmic. Physiol. Opt.* **25**, 492-500 (2005).

9. Hood, D.C. Assessing retinal function with the multifocal technique. *Prog. Retin. Eye Res.* **19**, 607-46 (2000).

10. Ball, S.L. & Petry, H.M. Noninvasive assessment of retinal function in rats using multifocal electroretinography. *Invest. Ophthalmol. Vis. Sci.* **41**, 610-7 (2000).

11. Owsley, C. et al. Associations between abnormal rod-mediated dark adaptation and health and functioning in older adults with normal macular health. *Invest. Ophthalmol. Vis. Sci.* **55**, 4776-89 (2014).

12. Jackson, G.R. et al. Diagnostic sensitivity and specificity of dark adaptometry for detection of age-related macular degeneration. *Invest. Ophthalmol. Vis. Sci.* **55**, 1427-31 (2014).

13. Jackson, G.R. et al. Twelve-Month Natural History of Dark Adaptation in Patients with AMD. *Optom. Vis. Sci.* **91**, 925-31 (2014).

14. Zhang, Q.X., Lu, R.W., Curcio, C.A. & Yao, X.C. In vivo confocal intrinsic optical signal identification of localized retinal dysfunction. *Invest. Ophthalmol. Vis. Sci.* **53**, 8139-45 (2012).

15. Yao, X.C. & George, J.S. Near-infrared imaging of fast intrinsic optical responses in visible light-activated amphibian retina. *J. Biomed. Opt.* **11**(2006).

16. Yao, X.C. & Zhao, Y.B. Optical dissection of stimulus-evoked retinal activation. *Opt. Express* **16**, 12446-12459 (2008).

17. Schallek, J. et al. Stimulus-evoked intrinsic optical signals in the retina: spatial and temporal characteristics. *Invest. Ophthalmol. Vis. Sci.* **50**, 4865-72 (2009).

18. Schallek, J.B., McLellan, G.J., Viswanathan, S. & Ts'o, D.Y. Retinal intrinsic optical signals in a cat model of primary congenital glaucoma. *Invest. Ophthalmol. Vis. Sci.* **53**, 1971-81 (2012).

19. Tsunoda, K. et al. Origins of retinal intrinsic signals: a series of experiments on retinas of macaque monkeys. *Jpn. J. Ophthalmol.* **53**, 297-314 (2009).

20. Inomata, K. et al. Distribution of retinal responses evoked by transscleral electrical stimulation detected by intrinsic signal imaging in macaque monkeys. *Invest. Ophthalmol. Vis. Sci.* **49**, 2193-200 (2008).

21. Abramoff, M.D. et al. Visual stimulus-induced changes in human near-infrared fundus reflectance. *Invest. Ophthalmol. Vis. Sci.* **47**, 715-721 (2006).

22. Ts'o, D. et al. Noninvasive functional imaging of the retina reveals outer retinal and hemodynamic intrinsic optical signal origins. *Jpn. J. Ophthalmol.* **53**, 334-44 (2009).

23. Jonnal, R.S. et al. In vivo functional imaging of human cone photoreceptors. *Opt. Express* **15**, 16141-16160 (2007).

24. Grieve, K. & Roorda, A. Intrinsic signals from human cone photoreceptors. *Invest. Ophthalmol. Vis. Sci.* **49**, 713-9 (2008).

25. Rha, J., Schroeder, B., Godara, P. & Carroll, J. Variable optical activation of human cone photoreceptors visualized using a short coherence light source. *Opt. Lett.* **34**, 3782-3784 (2009).

26. Yao, X.C., Yamauchi, A., Perry, B. & George, J.S. Rapid optical coherence tomography and recording functional scattering changes from activated frog retina. *Appl. Opt.* **44**, 2019-2023 (2005).

27. Srinivasan, V.J., Wojtkowski, M., Fujimoto, J.G. & Duker, J.S. In vivo measurement of retinal physiology with high-speed ultrahigh-resolution optical coherence tomography. *Opt. Lett.* **31**, 2308-10 (2006).

28. Bizheva, K. et al. Optophysiology: depth-resolved probing of retinal physiology with functional ultrahigh-resolution optical coherence tomography. *Proc. Natl. Acad. Sci. U.S.A.* **103**, 5066-71 (2006).

29. Zhang, Q.X., Lu, R.W., Li, Y.G. & Yao, X.C. In vivo confocal imaging of fast intrinsic optical signals correlated with frog retinal activation. *Opt. Lett.* **36**, 4692-4 (2011).

30. Nilsson, S.E. An Electron Microscopic Classification of the Retinal Receptors of the Leopard Frog (Rana Pipiens). *J. Ultrastruct. Res.* **10**, 390-416 (1964).

31. Staurenghi, G., Sadda, S., Chakravarthy, U., Spaide, R.F. & International Nomenclature for Optical Coherence Tomography, P. Proposed Lexicon for Anatomic Landmarks in Normal Posterior Segment Spectral-Domain Optical Coherence Tomography: The IN*OCT Consensus. *Ophthalmol.* **121**, 1572-8 (2014).

32. Wang, B.Q., Lu, R.W., Zhang, Q.X. & Yao, X.C. Enface optical coherence tomography of transient light response at photoreceptor outer segments in living frog eyecup. *Opt. Lett.* **38**, 4526-9 (2013).

33. Zhang, Q.X. et al. In vivo Optical Coherence Tomography of Light-Driven Melanosome Translocation in Retinal Pigment Epithelium. *Sci. Rep.* **3**, 2644 (2013).

34. Hofmann, K.P., Uhl, R., Hoffmann, W. & Kreutz, W. Measurements on fast light-induced light-scattering and -absorption changes in outer segments of vertebrate light sensitive rod cells. *Biophys. Struct. Mech.* **2**, 61-77 (1976).

35. Kuhn, H., Bennett, N., Michel-Villaz, M. & Chabre, M. Interactions between photoexcited rhodopsin and GTP-binding protein: kinetic and stoichiometric analyses from light-scattering changes. *Proc. Natl. Acad. Sci. U. S. A.* **78**, 6873-7 (1981).

36. Arshavsky, V.Y., Lamb, T.D. & Pugh, E.N., Jr. G proteins and phototransduction. *Annu. Rev. Physiol.* **64**, 153-87 (2002).

37. Feigl, B. & Morris, C.P. The challenge of predicting macular degeneration. *Curr. Med. Res. Opin.* **27**, 1745-8 (2011).

38. Friedman, D.S. et al. Prevalence of age-related macular degeneration in the United States. *Arch. Ophthalmol.* **122**, 564-72 (2004).

39. Deangelis, M.M., Silveira, A.C., Carr, E.A. & Kim, I.K. Genetics of age-related macular degeneration: current concepts, future directions. *Semin. Ophthalmol.* **26**, 77-93 (2011).

40. Ishikawa, K. et al. Focal macular electroretinograms after photodynamic therapy combined with intravitreal bevacizumab. *Graefes Arch. Clin. Exp. Ophthalmol.* **249**, 273-280 (2011).

41. Sunness, J.S. et al. Diminished foveal sensitivity may predict the development of advanced age-related macular degeneration. *Ophthalmol.* **96**, 375-81 (1989).

42. Owsley, C., McGwin, G., Jr., Jackson, G.R., Kallies, K. & Clark, M. Cone- and rod-mediated dark adaptation impairment in age-related maculopathy. *Ophthalmol.* **114**, 1728-35 (2007).

43. Curcio, C.A., Medeiros, N.E. & Millican, C.L. Photoreceptor loss in age-related macular degeneration. *Invest. Ophthalmol. Vis. Sci.* **37**, 1236-1249 (1996).

44. Li, Y.C. et al. Parallel optical monitoring of visual signal propagation from the photoreceptors to the inner retina layers. *Opt. Lett.* **35**, 1810-1812 (2010).

45. Cakir, Y. & Strauch, S.M. Tricaine (MS-222) is a safe anesthetic compound compared to benzocaine and pentobarbital to induce anesthesia in leopard frogs (Rana pipiens). *Pharmacol. Rep.* **57**, 467-74 (2005).

46. Srinivasan, V.J., Chen, Y., Duker, J.S. & Fujimoto, J.G. In vivo functional imaging of intrinsic scattering changes in the human retina with high-speed ultrahigh resolution OCT. *Opt. Express* **17**, 3861-77 (2009).

47. Latecki, L.J. & Lakamper, R. Shape similarity measure based on correspondence of visual parts. *IEEE Trans. Pattern Anal. Mach. Intell.* **22**, 1185-1190 (2000).

48. Wojtkowski, M. et al. Ultrahigh-resolution, high-speed, Fourier domain optical coherence tomography and methods for dispersion compensation. *Opt. Express* **12**, 2404-22 (2004).
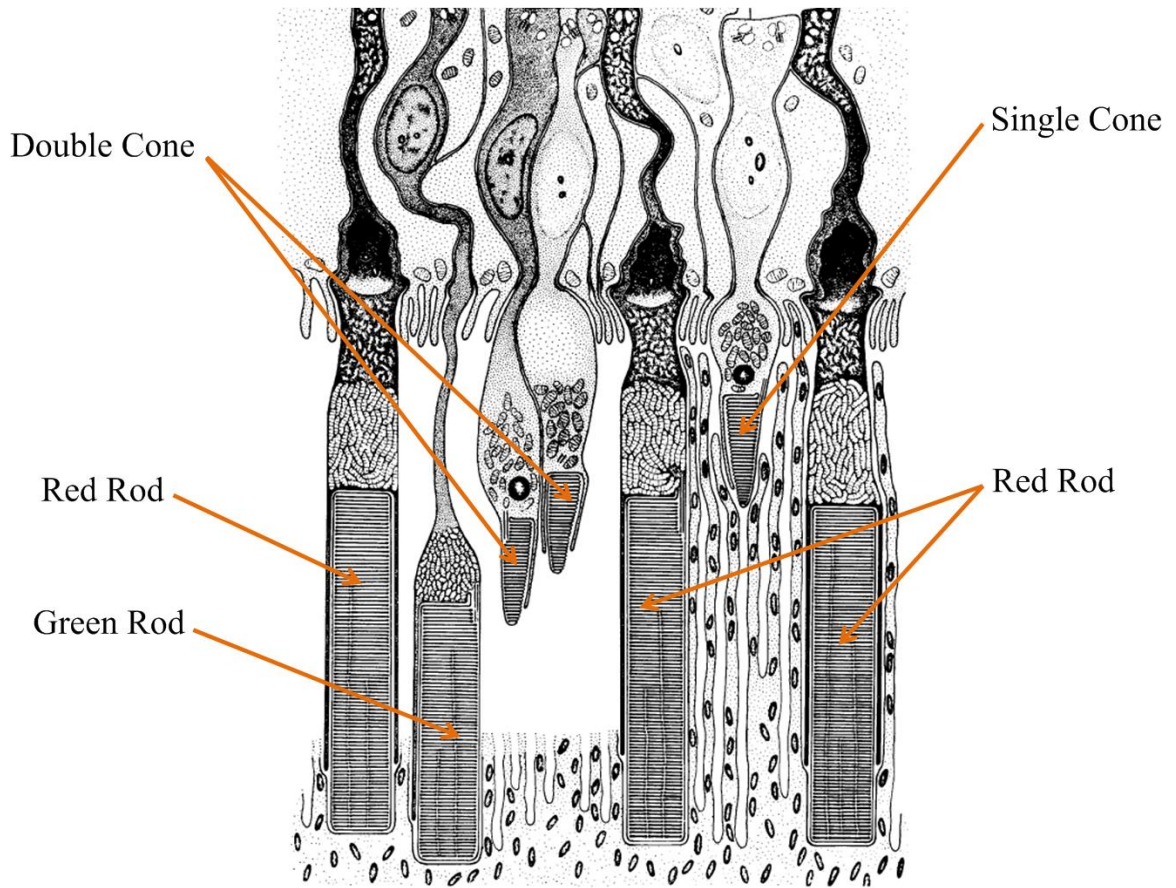
Figure 1. Schematic diagram of retinal photoreceptors of leopard frog (Rana Pipiens). Reprinted from *J Ultrastruct Res*, 10. Nilsson SE. An Electron Microscopic Classification of the Retinal Receptors of the Leopard Frog (Rana Pipiens). p390-p416, 1964, with permission form Eleevier.
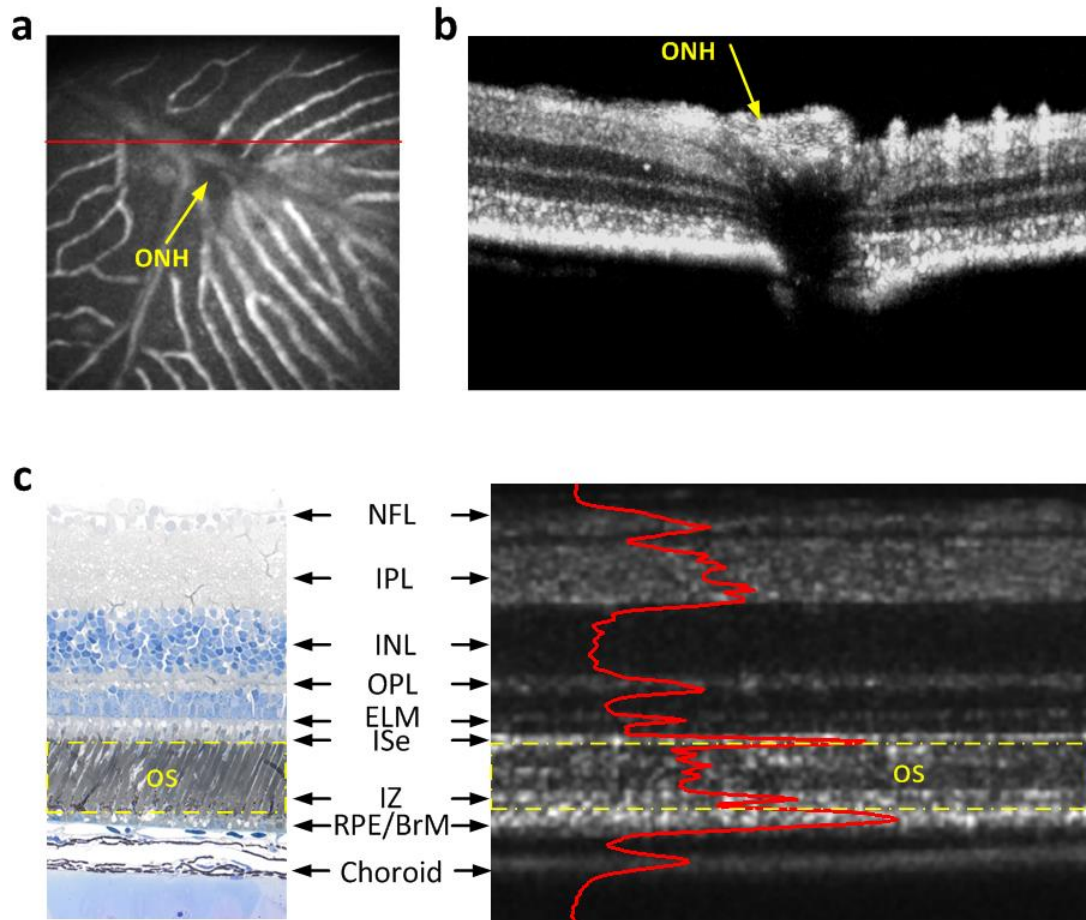
Figure 2. Combined OCT and fundus imaging. Fundus image reveals blood vessels around the optical nerve head (ONH). (b) OCT B-scan image of the area marked by the red line in A. (c) Histological image of frog retina (left) and the corresponding OCT B-scan image with individual layers labeled (right). Outer segment region is marked in yellow dashed rectangle in both histological image and OCT B-scan image. It contains both hyperreflective and hyporeflective bands in OCT B-scan image. The B-scan image is displayed in a linear scale. NFL: nerve fiber layer, IPL: inner plexiform layer, INL: inner nuclear layer, OPL: outer plexiform layer, ELM: external limiting membrane, ISe: inner segment ellipsoid, IZ: interdigitation zone, RPE/BrM: retinal pigment epithelium/Bruch's membrane.

Figure 3. Spatiotemporal characterization of functional OCT-IOS imaging with 10 ms flash stimulus. Raw OCT images are collected with frame rate of 100 Hz. Stimulus onset is indicated by time "0". OCT B-scan images are presented in linear scale. (a) OCT B-scan image and spatial IOS image sequence are averaged over 10 frames (100 ms interval). Images consist of 140 pixels (lateral) x 200 pixels (axial), corresponding to 200 μm (lateral) x 360 μm (axial). (b) IOS distribution map is superimposed on the OCT B-scan image. Positive signals (increasing reflectance) and negative signals (decreasing reflectance) are presented in red and green, respectively. Signal magnitude is not indicated in the image. (c) Temporal curves of averaged positive and negative IOSs. (d) To better visualize the signal onset time, enlarged profile of early 80 ms period is illustrated. (e) Comparative OCT-IOS and histological images of outer retina. In the histological image, cone photoreceptors are highlighted in green or red to show cell sizes and locations. Cone photoreceptor OS highlighted with red circles is located at the level of rod ISe.
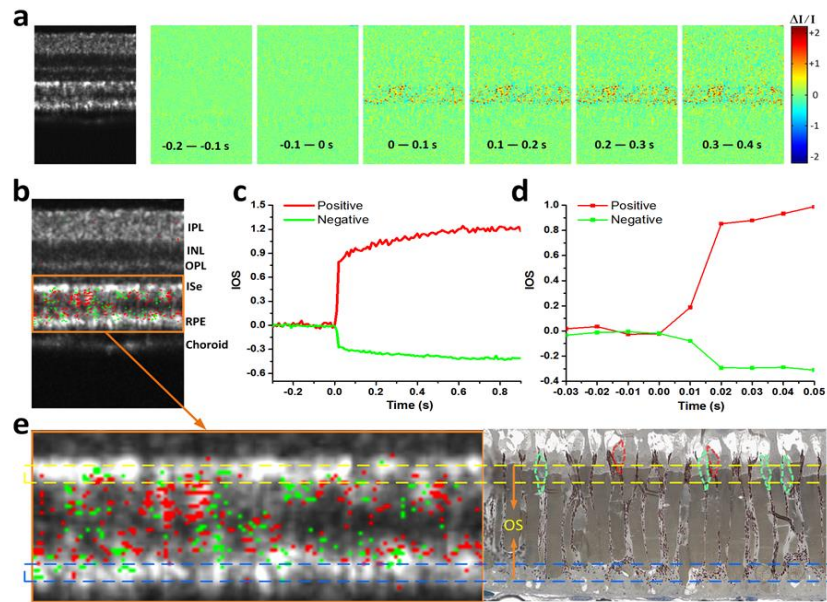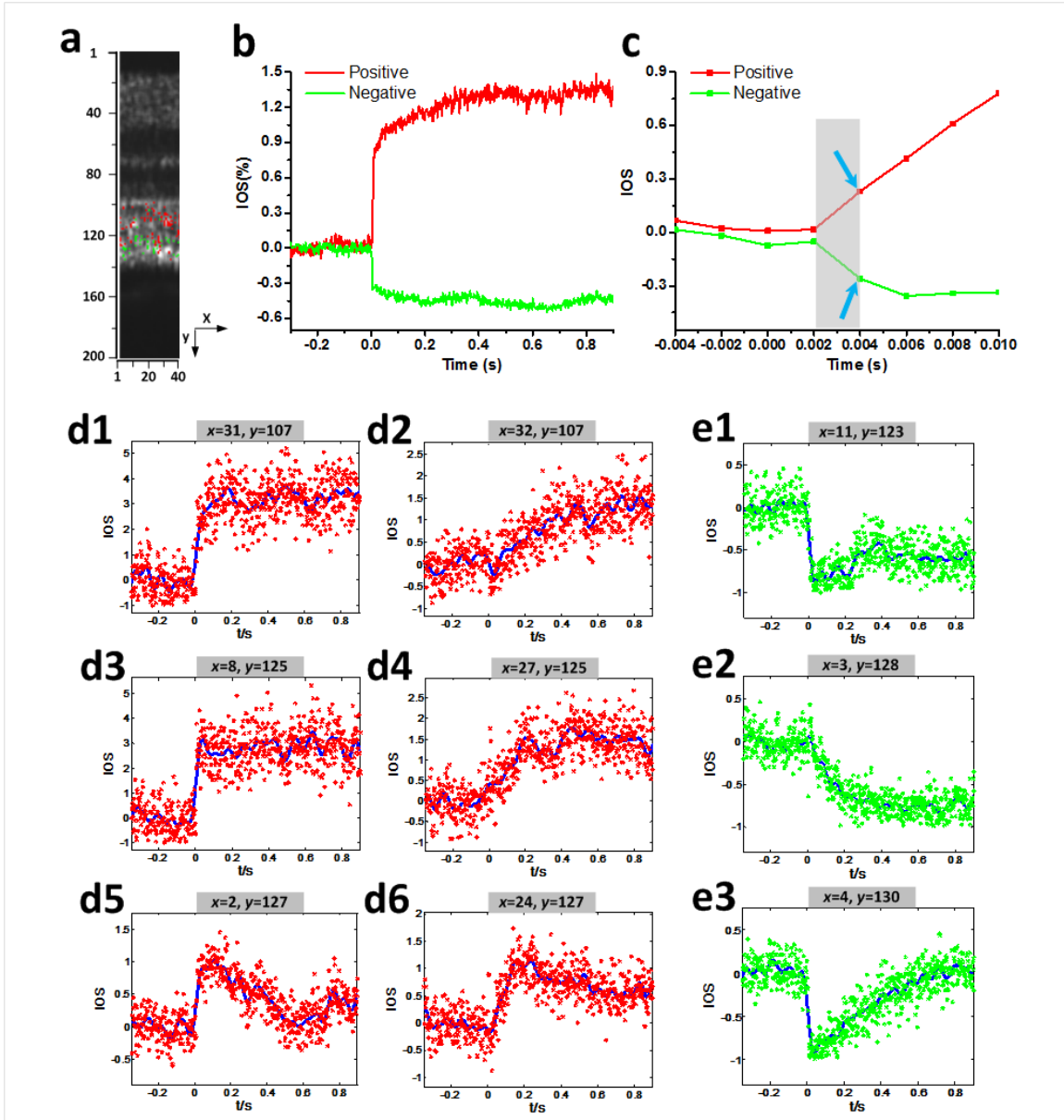
Figure 4. Spatiotemporal characteristics of fast IOSs with 10 ms flash stimulus. Raw OCT images are collected with frame rate of 500 Hz. Stimulus onset is indicated by time "0". (a) The OCT B-scan image consists of 40 pixels (lateral) x 200 pixels (axial), corresponding to 60 μm (lateral) x 360 μm (axial). Illustrated OCT B-scan images are displayed in linear scale. The IOS distribution map is superimposed on the OCT B-scan image. (b) Temporal curves of the averaged positive and negative IOSs. (c)

To better visualize the IOS onset times, enlarged profile of early 14 ms period is illustrated. (d1-d6) Positive IOSs of individual pixels; both raw data (labeled with star in red) and fitting curves (in blue) are shown. d1 ($x=31$, $y=107$) and d2 ($x=32$, $y=107$) are selected from the same axial location at adjacent locations in lateral direction. d3 ($x=8$, $y=125$) and d4 ($x=27$, $y=125$) also share the same axial location but with different lateral positions. d5 ($x=2$, $y=127$) and d6 ($x=24$, $y=127$) are the same. (e1-e3) Negative IOSs of individual pixels; both raw data (labeled with star in green) and fitting curve (in blue) are shown. e1 ($x=11$, $y=123$), e2($x=3$, $y=128$) and e3 ($x=4$, $y=130$) are from different locations.
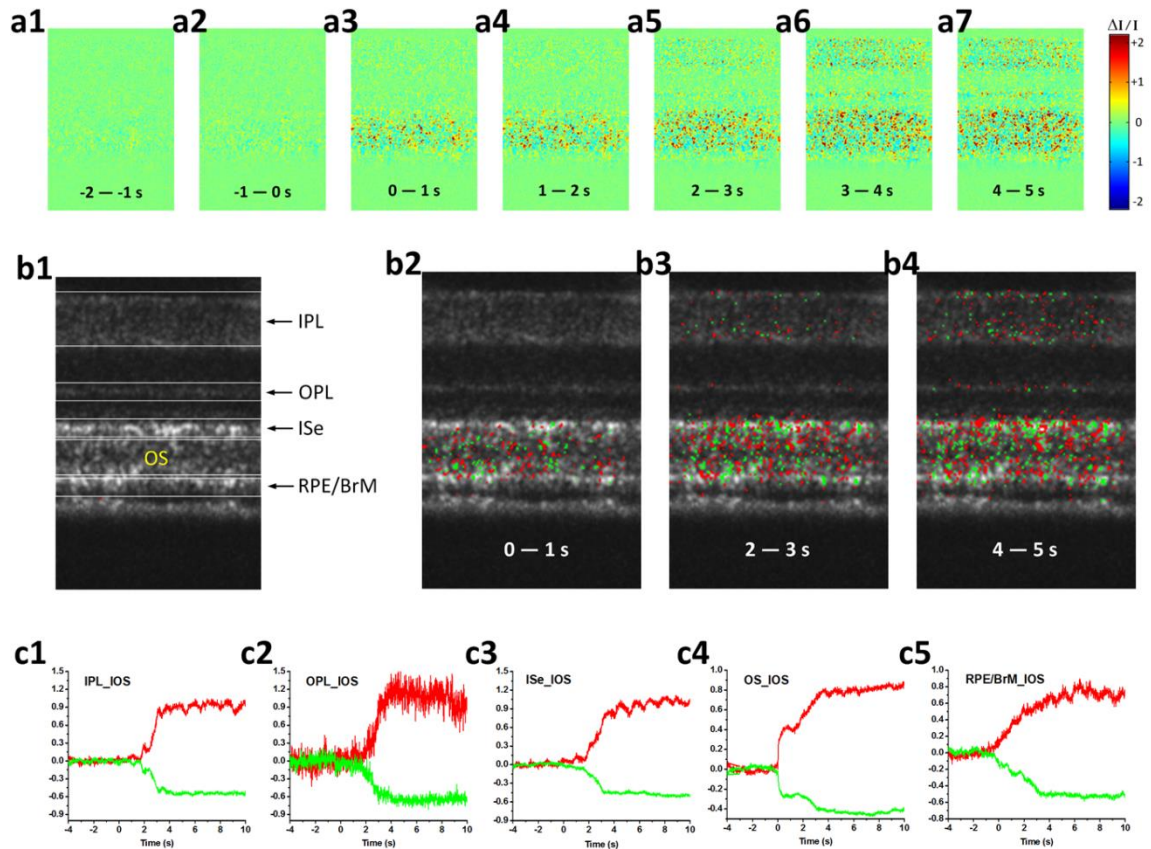
Figure 5. Spatiotemporal characterization of functional OCT-IOS imaging with 500 ms stimulus. OCT B-scan images are collected with frame rate of 100 Hz. (a) Spatial IOS image sequence averaged over 100 frames (1000 ms interval). (b) OCT B-scan image and OCT-IOS images at 0-1s, 2-3 s and 4-5 s. (c) The corresponding individual temporal curves of averaged positive and negative IOSs from IPL, OPL, ISe, OS and RPE/BrM.
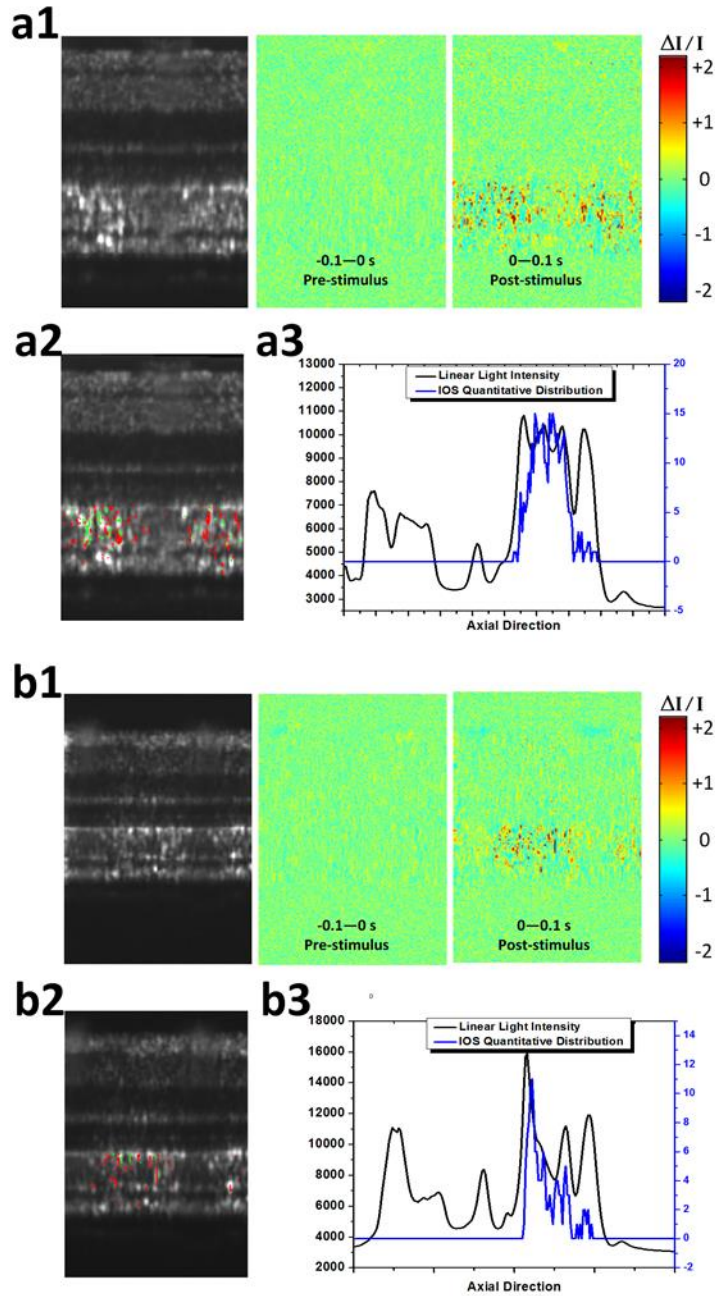
Figure 6. Spatial characteristics of the IOSs in different background light conditions. OCT B-scan images are displayed in a linear scale. (a1) OCT B-scan image and spatial IOS images are collected in dark condition. Pre-stimulus and post-stimulus images are averaged over 10 frames (100 ms interval) (a2) OCT-IOS image in the dark condition. (a3) Corresponding light intensity and IOS distribution curve across the retina. The light

intensity curve is obtained by averaging the light intensity of the OCT B-scan image laterally. The IOS distribution is obtained by calculating the pixel number of IOSs laterally in the axial direction. The signal polarities are ignored for calculating IOS quantities. (b1) OCT B-scan image and spatial IOS images are collected under light condition (~ 200 cd·s/m2). Pre-stimulus and post-stimulus are averaged over 10 frames (100 ms interval) (b2) OCT-IOS image in the light condition. (b3) Corresponding light intensity and IOS distribution curve across the retina.
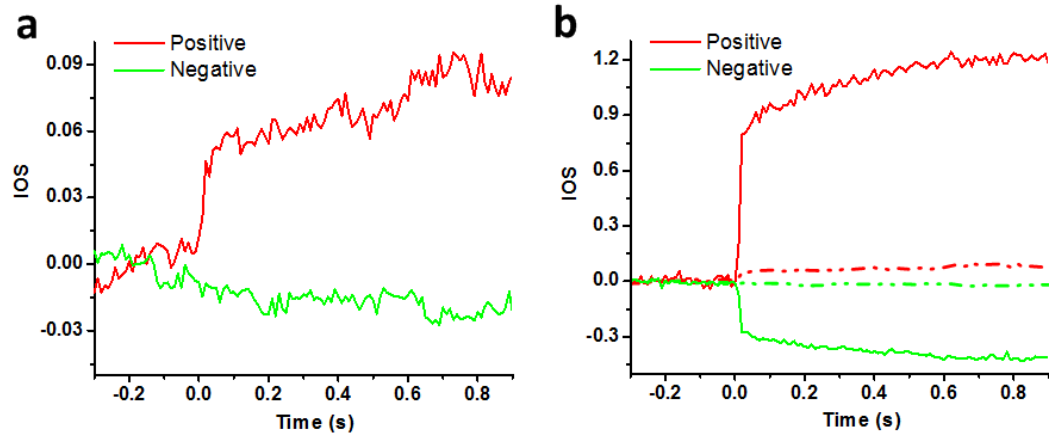
Figure 7. Comparative IOSs before and after applying adaptive algorithm. (a) Averaged positive and negative IOSs are processed with traditional method, i.e. for each pixel, if the IOS larger than 0.05 ΔI/I , it would be accounted as positive signal, while those below -0.05 ΔI/I would be regarded as negative signals. (b) Combined IOSs processed with the adaptive algorithm (solid lines) and those processed with traditional method (dotted lines).
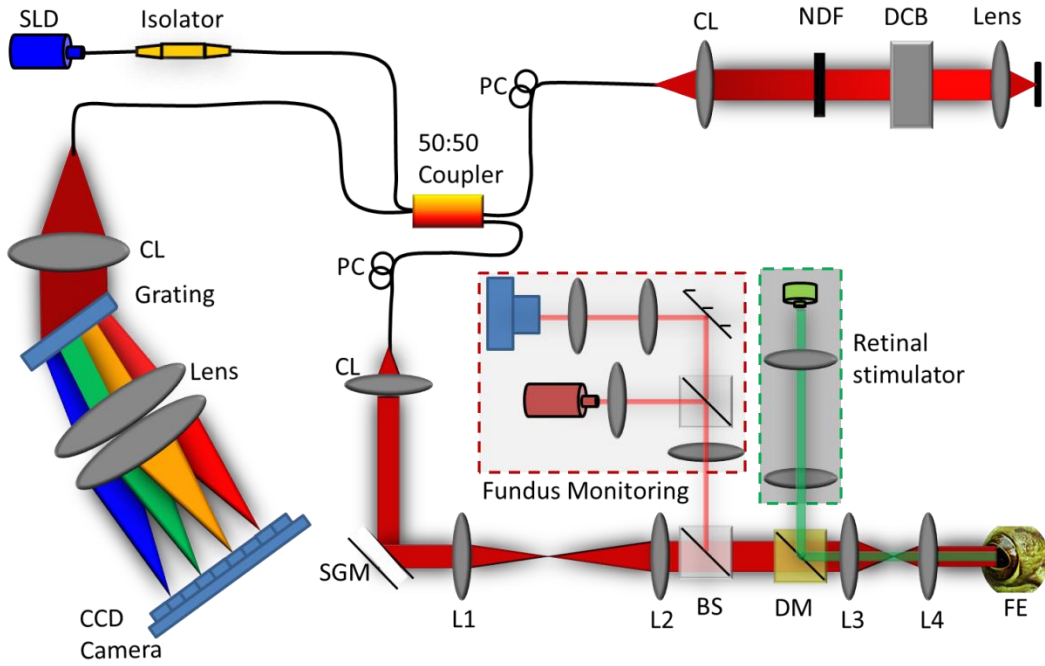
Figure 8. Schematic diagram of the experimental setup. The system is configured with retinal stimulator (indicated within green dash line) and fundus camera (indicated within rea dash line) for in vivo functional IOS imaging of the retina. SLD: superluminescent diode, PC: polarization controller, CL: collimation lens, NDF: neutral density filter, DCB: dispersion compensating block, SGM: scanning galvanometer mirror, BS: beam splitter, DM: dichroic mirror, FE: frog eye, CCD: charge-coupled device, L1–L4: lens. Focal lengths of lenses L1, L2, L3 and L4 are 75, 100, 35, and 25 mm, respectively.

SUMMARY

The primary aim of my Ph.D. dissertation research is to design and develop optical systems for *in vivo* IOS recording, therefore, to pave the way for clinical application of IOS imaging for early retinal eye disease detection. A lot of previous studies were conducted in our lab to investigate the IOS characteristic or signal source from isolated frog retinas. My Ph.D. desertion research is committed to realize *in vivo* IOS imaging and overcome the limitations in previous research for *in vivo* IOS imaging, such as low spatiotemporal resolution and low SNR. IOS imaging *in vivo* is usually challenging due to relatively small signal magnitude caused by contamination from ocular movement, heat beat and blood flow etc. Therefore, *in vivo* IOS imaging from anesthetized animal is more reliable than that from awake humans. In addition, before the new imaging technique can be brought into clinical use, more investigation regarding to the signal sources and characteristics need to be conducted.

A rapid line-scan confocal ophthalmoscope for *in vivo* IOS imaging from anesthetized frog retina was developed. Compared with traditional point-to-point confocal microscope, line-scan confocal is featured by its rapid image acquisition speed up to 200 Hz, which is essential for fast IOS recording. At the same time, by rejecting out-of-focus light, line-scan confocal ophthalmoscope is capable to provide the resolution to differentiate individual photoreceptors *in vivo*. In addition to good optical system design, the signal synchronization is also very critical for the experiment. In order to generate control signals to different system components and make them work together, we used to employ a stack of function generators which can cost more than 10 thousand

113

dollars. I updated the system by using a multifunctional data acquisition board and developed the related labview programs, which is more cost-effective compared with functional generators. Besides, by using LABVIEW, the experimental procedures become simpler and more effective. Another key factor for *in vivo* IOS imaging is the simulation delivery subsystem. We used localized stimulation. First, it can produce natural control and experimental areas. Second, the localized stimulation pattern facilitates the detection of a small dysfunctional area. The experimental results of line-scan confocal-IOS imaging of localized retinal response in anesthetized frog eye showed the robust and reliable IOSs pattern related with localized rectangle stimulation. Meanwhile artifacts originated from the blood vessels were also observed. By using a spatial filter, most of the rapid blood flow activities were ruled out from stimulus-evoked retinal responses. With a clean background, the stimulus activated IOS pattern could be visualized clearly. Both positive and negative signals were observed almost immediately after the retinal stimulation.

We also designed an experiment to demonstrate the feasibility of using IOS imaging to detect small lesion in the retina. The structural images of the retina in normal condition and the image with small area of laser-injury could barely show any visible differences. After a full field stimulus was applied, IOS image of local laser-injury retina showed a signal-absent area located at the place where the damaged was introduced, while in health retina, IOSs were homogenously distributed.

In order to investigate the physiological mechanism of confocal IOS, comparative IOS and electroretinography (ERG) measurements were conducted using normal frog eyes activated by variable intensity stimuli. The overall trend of IOS magnitude and time-

to-peak of IOSs was quite consistent with those of a-wave, which suggests that the confocal-IOSs may come from retinal photoreceptors. As we all know, retinal photoreceptors include outer segment, inner segment, and synaptic ending. Due to the limited axial resolution of the confocal system, it is impossible to accurately verify the axial location of the IOS source within the photoreceptor. Therefore, we also developed another optical system, SD-OCT.

We custom designed the spectrometer to approach the theoretical axial resolution limited by the light source. The lens combinations in the sample arm of SD-OCT were also specially designed for *in vivo* frog retina imaging. The constructed system is featured by its high spatial resolution in three dimensions (3.0 μm x 3.0 μm x 3.0 μm) and millisecond temporal resolution (500 Hz). Using this system, we not only revealed that the IOSs was primarily originated from the photoreceptor outer segment, but also demonstrated the feasibility of functional OCT mapping of rod and cone photoreceptors by conducting the comparative studies of dark- and light-adapted retinas.

In additional to functional retinal imaging, we also applied the SD-OCT system for *in vivo* dynamic observation of light-driven melanosome translocation in RPE. Comparative OCT examination of dark- and light- adapted frog eyes verified that RPE melanosomes is a primary source of reflectivity in the RPE band. To the best of our knowledge, this is the first time demonstration of the feasibility of dynamic OCT monitoring of sub-cellular RPE translocation.

Up till now, all reported IOS studies were based on normal retinas. The feasibility of using fast IOS imaging to differentiate abnormal retinas from normal ones was yet to be demonstrated. Using a custom-modified microscope, we have conducted preliminary

investigations of both wild-type and mutant mouse retinas. A Cngb1 knockout mouse model (Mus musculus) that does not express the β-subunit of the cGMP-gated cation channel and the related GARP proteins was employed for this study. Rod function is attenuated but a small group of individual photoreceptor cells, spreading over the whole region of images and lasting over the detectable up to 6 months. By 1 year of age the ERG response is no longer detectable and all rod cells have degenerated. Experimental results revealed that rod-degenerated mice, compared to wild-type mice of the same species. In comparison with traditional ERG recording, IOS imaging could also disclose spatial distribution information of the signal. With relatively clean background for wild-type mice, mutant mice showed scattered granular patterns over the whole recording time. This preliminary study of accurate retinas has demonstrated the potential of using fast IOS to differentiate normal and diseased retinas.

GENERAL LIST OF REFERENCE

1.   Curcio CA, Medeiros NE, Millican CL. Photoreceptor loss in age-related macular degeneration. *Investigative Ophthalmology & Visual Science* 1996, **37**(7)**:** 1236-1249.

2.   Nagy D, Schonfisch B, Zrenner E, Jagle H. Long-term follow-up of retinitis pigmentosa patients with multifocal electroretinography. *Invest Ophthalmol Vis Sci* 2008, **49**(10)**:** 4664-4671.

3.   Qin YW, Xu GZ, Wang WJ. Dendritic abnormalities in retinal ganglion cells of three-month diabetic rats. *Curr Eye Res* 2006, **31**(11)**:** 967-974.

4.   Scholl HP, Zrenner E. Electrophysiology in the investigation of acquired retinal disorders. *Survey of ophthalmology* 2000, **45**(1)**:** 29-47.

5.   Hood DC. Assessing retinal function with the multifocal technique. *Progress in retinal and eye research* 2000, **19**(5)**:** 607-646.

6.   Quigley HA, Dunkelberger GR, Green WR. Retinal ganglion cell atrophy correlated with automated perimetry in human eyes with glaucoma. *American journal of ophthalmology* 1989, **107**(5)**:** 453-464.

7.   Cohen LB. Changes in neuron structure during action potential propagation and synaptic transmission. *Physiological reviews* 1973, **53**(2)**:** 373-418.

8.   Zepeda A, Arias C, Sengpiel F. Optical imaging of intrinsic signals: recent developments in the methodology and its applications. *Journal of neuroscience methods* 2004, **136**(1)**:** 1-21.

9.   Ts'o DY, Frostig RD, Lieke EE, Grinvald A. Functional organization of primate visual cortex revealed by high resolution optical imaging. *Science* 1990, **249**(4967)**:** 417-420.

10.   Frostig RD, Lieke EE, Ts'o DY, Grinvald A. Cortical functional architecture and local coupling between neuronal activity and the microcirculation revealed by in vivo high-resolution optical imaging of intrinsic signals. *Proceedings of the*

National Academy of Sciences of the United States of America 1990, **87**(16)**:** 6082-6086.

11.   Roe AW, Ts'o DY. Visual topography in primate V2: multiple representation across functional stripes. *The Journal of neuroscience : the official journal of the Society for Neuroscience* 1995, **15**(5 Pt 2)**:** 3689-3715.

12.   Ghose GM, Ts'o DY. Form processing modules in primate area V4. *Journal of neurophysiology* 1997, **77**(4)**:** 2191-2196.

13.   Malonek D, Tootell RB, Grinvald A. Optical imaging reveals the functional architecture of neurons processing shape and motion in owl monkey area MT. *Proceedings Biological sciences / The Royal Society* 1994, **258**(1352)**:** 109-119.

14.   Tsunoda K, Yamane Y, Nishizaki M, Tanifuji M. Complex objects are represented in macaque inferotemporal cortex by the combination of feature columns. *Nature neuroscience* 2001, **4**(8)**:** 832-838.

15.   Li YG, Zhang QX, Liu L, Amthor FR, Yao XC. High spatiotemporal resolution imaging of fast intrinsic optical signals activated by retinal flicker stimulation. *Optics express* 2010, **18**(7)**:** 7210-7218.

16.   Li YG, Liu L, Amthor F, Yao XC. High-speed line-scan confocal imaging of stimulus-evoked intrinsic optical signals in the retina. *Optics letters* 2010, **35**(3)**:** 426-428.

17.   Zhang QX, Lu RW, Li YG, Yao XC. In vivo confocal imaging of fast intrinsic optical signals correlated with frog retinal activation. *Optics letters* 2011, **36**(23)**:** 4692-4694.

18.   Wang B, Lu R, Zhang Q, Jiang Y, Yao X. En face optical coherence tomography of transient light response at photoreceptor outer segments in living frog eyecup. *Optics letters* 2013, **38**(22)**:** 4526-4529.

19.   Hofmann KP, Uhl R, Hoffmann W, Kreutz W. Measurements on fast light-induced light-scattering and -absorption changes in outer segments of vertebrate light sensitive rod cells. *Biophysics of structure and mechanism* 1976, **2**(1)**:** 61-77.

20.   Kuhn H, Bennett N, Michel-Villaz M, Chabre M. Interactions between photoexcited rhodopsin and GTP-binding protein: kinetic and stoichiometric analyses from light-scattering changes. *Proceedings of the National Academy of Sciences of the United States of America* 1981, **78**(11)**:** 6873-6877.

21. Arshavsky VY, Lamb TD, Pugh EN, Jr. G proteins and phototransduction. *Annual review of physiology* 2002, **64:** 153-187.

22. Yao XC, Rector DM, George JS. Optical lever recording of displacements from activated lobster nerve bundles and Nitella internodes. *Applied optics* 2003, **42**(16)**:** 2972-2978.

23. Tasaki I, Byrne PM. Rapid structural changes in nerve fibers evoked by electric current pulses. *Biochemical and biophysical research communications* 1992, **188**(2)**:** 559-564.

24. Kim GH, Kosterin P, Obaid AL, Salzberg BM. A mechanical spike accompanies the action potential in Mammalian nerve terminals. *Biophys J* 2007, **92**(9)**:** 3122-3129.

25. Barriga ES, Pattichis M, Ts'o D, Abramoff M, Kardon R, Kwon Y*, et al.* Spatiotemporal independent component analysis for the detection of functional responses in cat retinal images. *IEEE transactions on medical imaging* 2007, **26**(8)**:** 1035-1045.

26. Schallek J, Kardon R, Kwon Y, Abramoff M, Soliz P, Ts'o D. Stimulus-evoked intrinsic optical signals in the retina: pharmacologic dissection reveals outer retinal origins. *Investigative ophthalmology & visual science* 2009, **50**(10)**:** 4873-4880.

27. Schallek J, Li H, Kardon R, Kwon Y, Abramoff M, Soliz P*, et al.* Stimulus-evoked intrinsic optical signals in the retina: spatial and temporal characteristics. *Investigative ophthalmology & visual science* 2009, **50**(10)**:** 4865-4872.

28. Ts'o D, Schallek J, Kwon Y, Kardon R, Abramoff M, Soliz P. Noninvasive functional imaging of the retina reveals outer retinal and hemodynamic intrinsic optical signal origins. *Japanese journal of ophthalmology* 2009, **53**(4)**:** 334-344.

29. Schallek J, Ts'o D. Blood contrast agents enhance intrinsic signals in the retina: evidence for an underlying blood volume component. *Investigative ophthalmology & visual science* 2011, **52**(3)**:** 1325-1335.

30. Schallek JB, McLellan GJ, Viswanathan S, Ts'o DY. Retinal intrinsic optical signals in a cat model of primary congenital glaucoma. *Investigative ophthalmology & visual science* 2012, **53**(4)**:** 1971-1981.

31.   Tsunoda K, Oguchi Y, Hanazono G, Tanifuji M. Mapping cone- and rod-induced retinal responsiveness in macaque retina by optical imaging. *Investigative ophthalmology & visual science* 2004, **45**(10)**:** 3820-3826.

32.   Hanazono G, Tsunoda K, Shinoda K, Tsubota K, Miyake Y, Tanifuji M. Intrinsic signal imaging in macaque retina reveals different types of flash-induced light reflectance changes of different origins. *Investigative ophthalmology & visual science* 2007, **48**(6)**:** 2903-2912.

33.   Hanazono G, Tsunoda K, Kazato Y, Tsubota K, Tanifuji M. Evaluating neural activity of retinal ganglion cells by flash-evoked intrinsic signal imaging in macaque retina. *Investigative ophthalmology & visual science* 2008, **49**(10)**:** 4655-4663.

34.   Tsunoda K, Hanazono G, Inomata K, Kazato Y, Suzuki W, Tanifuji M. Origins of retinal intrinsic signals: a series of experiments on retinas of macaque monkeys. *Japanese journal of ophthalmology* 2009, **53**(4)**:** 297-314.

35.   Hanazono G, Tsunoda K, Kazato Y, Suzuki W, Tanifuji M. Functional topography of rod and cone photoreceptors in macaque retina determined by retinal densitometry. *Investigative ophthalmology & visual science* 2012, **53**(6)**:** 2796-2803.

36.   Abramoff MD, Kwon YH, Ts'o D, Soliz P, Zimmerman B, Pokorny J*, et al.* Visual stimulus-induced changes in human near-infrared fundus reflectance. *Investigative ophthalmology & visual science* 2006, **47**(2)**:** 715-721.

37.   Grieve K, Roorda A. Intrinsic signals from human cone photoreceptors. *Invest Ophthalmol Vis Sci* 2008, **49**(2)**:** 713-719.

38.   Yao XC, Yamauchi A, Perry B, George JS. Rapid optical coherence tomography and recording functional scattering changes from activated frog retina. *Applied optics* 2005, **44**(11)**:** 2019-2023.

39.   Bizheva K, Pflug R, Hermann B, Považay B, Sattmann H, Qiu P*, et al.* Optophysiology: depth-resolved probing of retinal physiology with functional ultrahigh-resolution optical coherence tomography. *Proceedings of the National Academy of Sciences of the United States of America* 2006, **103**(13)**:** 5066-5071.

40.   Srinivasan VJ, Wojtkowski M, Fujimoto JG, Duker JS. In vivo measurement of retinal physiology with high-speed ultrahigh-resolution optical coherence tomography. *Optics letters* 2006, **31**(15)**:** 2308-2310.

41. Rha J, Schroeder B, Godara P, Carroll J. Variable optical activation of human cone photoreceptors visualized using a short coherence light source. *Optics letters* 2009, **34**(24)**:** 3782-3784.

42. Srinivasan VJ, Chen Y, Duker JS, Fujimoto JG. In vivo functional imaging of intrinsic scattering changes in the human retina with high-speed ultrahigh resolution OCT. *Optics express* 2009, **17**(5)**:** 3861-3877.

43. Schmoll T, Kolbitsch C, Leitgeb RA. In vivo functional retinal optical coherence tomography. *Journal of biomedical optics* 2010, **15**(4)**:** 041513.

44. Moayed AA, Hariri S, Choh V, Bizheva K. In vivo imaging of intrinsic optical signals in chicken retina with functional optical coherence tomography. *Optics letters* 2011, **36**(23)**:** 4575-4577.

45. Akhlagh Moayed A, Hariri S, Choh V, Bizheva K. Correlation of visually evoked intrinsic optical signals and electroretinograms recorded from chicken retina with a combined functional optical coherence tomography and electroretinography system. *Journal of biomedical optics* 2012, **17**(1)**:** 016011.

46. Suzuki W, Tsunoda K, Hanazono G, Tanifuji M. Stimulus-induced changes of reflectivity detected by optical coherence tomography in macaque retina. *Investigative ophthalmology & visual science* 2013, **54**(9)**:** 6345-6354.

47. Yao XC, Yamauchi A, Perry B, George JS. Rapid optical coherence tomography and recording functional scattering changes from activated frog retina. *Applied Optics* 2005, **44**(11)**:** 2019-2023.

48. Yao XC, George JS. Dynamic neuroimaging of retinal light responses using fast intrinsic optical signals. *NeuroImage* 2006, **33**(3)**:** 898-906.

49. Yao XC, George JS. Near-infrared imaging of fast intrinsic optical responses in visible light-activated amphibian retina. *Journal of biomedical optics* 2006, **11**(6)**:** 064030.

50. Yao XC, Zhao YB. Optical dissection of stimulus-evoked retinal activation. *Optics express* 2008, **16**(17)**:** 12446-12459.

51. Zhao YB, Yao XC. Intrinsic optical imaging of stimulus-modulated physiological responses in amphibian retina. *Optics letters* 2008, **33**(4)**:** 342-344.

52.   Yao XC. Intrinsic optical signal imaging of retinal activation. *Japanese journal of ophthalmology* 2009, **53**(4)**:** 327-333.

53.   Yao XC, Liu L, Li YG. Intrinsic optical signal imaging of retinal activity in frog eye *Journal of Innovative Optical Health Sciences* 2009, **2**(2)**:** 201–208.

54.   Li YG, Zhang QX, Liu L, Amthor F, Yao XC. High spatiotemporal resolution imaging of fast intrinsic optical signals activated by retinal flicker stimulation. *Opt Express* 2010, **18**(7)**:** 7210-7218

55.   Li YG, Liu L, Amthor F, Yao XC. High-speed line-scan confocal imaging of stimulus-evoked intrinsic optical signals in the retina. *Optics Letters* 2010, **35**(3)**:** 426-428.

56.   Li YC, Strang C, Amthor F, Liu L, Li YG, Zhang QX*, et al.* Parallel optical monitoring of visual signal propagation from the photoreceptors to inner retina layers *Optics Letters* 2010, **35**(11).

57.   Zhang QX, Wang JY, Liu L, Yao XC. Microlens array recording of localized retinal responses. *Optics Letters* 2010, **35**(22)**:** 3838-3840.

58.   Jonnal RS, Rha J, Zhang Y, Cense B, Gao W, Miller DT. In vivo functional imaging of human cone photoreceptors. *Optics express* 2007, **15**(24)**:** 16141-16160.

59.   Aho AC. The visual acuity of the frog (Rana pipiens). *Journal of comparative physiology A, Sensory, neural, and behavioral physiology* 1997, **180**(1)**:** 19-24.

60.   Huang D, Swanson EA, Lin CP, Schuman JS, Stinson WG, Chang W*, et al.* Optical coherence tomography. *Science* 1991, **254**(5035)**:** 1178-1181.

61.   Wojtkowski M, Leitgeb R, Kowalczyk A, Bajraszewski T, Fercher AF. In vivo human retinal imaging by Fourier domain optical coherence tomography. *Journal of biomedical optics* 2002, **7**(3)**:** 457-463.

62.   Srinivasan VJ, Ko TH, Wojtkowski M, Carvalho M, Clermont A, Bursell SE*, et al.* Noninvasive volumetric imaging and morphometry of the rodent retina with high-speed, ultrahigh-resolution optical coherence tomography. *Investigative ophthalmology & visual science* 2006, **47**(12)**:** 5522-5528.

63.   Konno S, Akiba J, Yoshida A. Retinal thickness measurements with optical coherence tomography and the scanning retinal thickness analyzer. *Retina* 2001, **21**(1)**:** 57-61.

64.   Koozekanani D, Boyer K, Roberts C. Retinal thickness measurements from optical coherence tomography using a Markov boundary model. *IEEE transactions on medical imaging* 2001, **20**(9)**:** 900-916.

65.   Bizheva K, Pflug R, Hermann B, Povazay B, Sattmann H, Qiu P*, et al.* Optophysiology: depth-resolved probing of retinal physiology with functional ultrahigh-resolution optical coherence tomography. *Proc Natl Acad Sci U S A* 2006, **103**(13)**:** 5066-5071.

66.   de Boer JF, Cense B, Park BH, Pierce MC, Tearney GJ, Bouma BE. Improved signal-to-noise ratio in spectral-domain compared with time-domain optical coherence tomography. *Optics letters* 2003, **28**(21)**:** 2067-2069.

67.   Schrottner J, Leitgeb N. [Influence of body size on the electric current perception threshold]. *Biomed Tech (Berl)* 2003, **48**(10)**:** 291-295.

68.   Leitgeb R, Hitzenberger C, Fercher A. Performance of fourier domain vs. time domain optical coherence tomography. *Optics express* 2003, **11**(8)**:** 889-894.

69.   Strouthidis NG, Yang H, Reynaud JF, Grimm JL, Gardiner SK, Fortune B*, et al.* Comparison of clinical and spectral domain optical coherence tomography optic disc margin anatomy. *Investigative ophthalmology & visual science* 2009, **50**(10)**:** 4709-4718.

70.   Hassenstein A, Meyer CH. Clinical use and research applications of Heidelberg retinal angiography and spectral-domain optical coherence tomography - a review. *Clinical & experimental ophthalmology* 2009, **37**(1)**:** 130-143.

71.   Ehlers JP, Tao YK, Farsiu S, Maldonado R, Izatt JA, Toth CA. Integration of a spectral domain optical coherence tomography system into a surgical microscope for intraoperative imaging. *Investigative ophthalmology & visual science* 2011, **52**(6)**:** 3153-3159.

72.   Chauhan DS, Marshall J. The interpretation of optical coherence tomography images of the retina. *Investigative ophthalmology & visual science* 1999, **40**(10)**:** 2332-2342.

73.   Wojtkowski M, Srinivasan V, Ko T, Fujimoto J, Kowalczyk A, Duker J. Ultrahigh-resolution, high-speed, Fourier domain optical coherence tomography and methods for dispersion compensation. *Optics express* 2004, **12**(11)**:** 2404-2422.

74.   {Izatt I, J. A., Hee MR, Owen GM, Swanson EA, Fujimoto JG. Optical coherence microscopy in scattering media. *Opt Lett* 1994, **19**(8)**:** 590-592.

APPENDIX A

INSTITUTIONAL ANIMAL CARE AND USE COMMITTEE APPROVAL
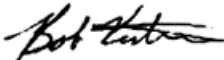
UAB THE UNIVERSITY OF ALABAMA AT BIRMINGHAM

Institutional Animal Care and Use Committee (IACUC)

NOTICE OF APPROVAL

DATE: November 20, 2013

TO: XINCHENG YAO, Ph.D.
          VH -390B
          (205) 996-7459

FROM: *[signature]*

          Robert A. Kesterson, Ph.D., Chair
          Institutional Animal Care and Use Committee (IACUC)

SUBJECT: Title: CAREER: Simultaneous Imaging of Photoreceptor and Post-Photoreceptor
          Responses in the Retina
          Sponsor: National Science Foundation
          Animal Project_Number: 131109312

As of November 20, 2013 the animal use proposed in the above referenced application is approved. The University of Alabama at Birmingham Institutional Animal Care and Use Committee (IACUC) approves the use of the following species and number of animals:

Species	Use Category	Number In Category
Frogs	A	100

Animal use must be renewed by November 19, 2014. Approval from the IACUC must be obtained before implementing any changes or modifications in the approved animal use.

Please keep this record for your files, and forward the attached letter to the appropriate granting agency.

Refer to Animal Protocol Number (APN) 131109312 when ordering animals or in any correspondence with the IACUC or Animal Resources Program (ARP) offices regarding this study. If you have concerns or questions regarding this notice, please call the IACUC office at (205) 934-7692.

Institutional Animal Care and Use Committee (IACUC) | Mailing Address:
CH19 Suite 403 | CH19 Suite 403
933 19th Street South | 1530 3rd Ave S
(205) 934-7692 | Birmingham, AL 35294-0019
FAX (205) 934-1188

UAB THE UNIVERSITY OF ALABAMA AT BIRMINGHAM

Institutional Animal Care and Use Committee (IACUC)

NOTICE OF APPROVAL

DATE: February 24, 2014

TO: STEVEN J PITTLER, Ph.D.
            VH -375B
            (205) 934-6744

FROM:

Robert A. Kesterson, Ph.D., Chair
Institutional Animal Care and Use Committee (IACUC)

SUBJECT: Title: Analysis of Retina Rod Photoreceptor GARP and cGMP-Gated Cation Channel
               Sponsor: NIH
               Animal Project_Number: 140208381

As of February 24, 2014 the animal use proposed in the above referenced application is approved. The University of Alabama at Birmingham Institutional Animal Care and Use Committee (IACUC) approves the use of the following species and number of animals:

Species	Use Category	Number In Category
Mice	A	2500

Animal use must be renewed by February 23, 2015. Approval from the IACUC must be obtained before implementing any changes or modifications in the approved animal use.

Please keep this record for your files, and forward the attached letter to the appropriate granting agency.

Refer to Animal Protocol Number (APN) 140208381 when ordering animals or in any correspondence with the IACUC or Animal Resources Program (ARP) offices regarding this study. If you have concerns or questions regarding this notice, please call the IACUC office at (205) 934-7692.

Institutional Animal Care and Use Committee (IACUC) | Mailing Address:
CH19 Suite 403 | CH19 Suite 403
933 19th Street South | 1530 3rd Ave S
(205) 934-7692 | Birmingham, AL 35294-0019
FAX (205) 934-1188 |

126

Admission to Candidacy
Research Compliance Verification Form

Instructions
Complete this form, including all applicable forms and the signatures of the student, the student's advisor, and the Graduate Program Director. For research approval forms, contact the Institutional Review Board (IRB) (http://www.uab.edu/irb or 934-3789), or the Institutional Animal Care and Use Committee (IACUC) (http://www.uab.edu/iacuc or 934-7692).

Human Subjects
The University of Alabama at Birmingham defines a human subject as not only a living human being, but also human tissue, blood samples, pathology or diagnostic specimens, study of medical records, observation of public behavior, and all questionnaires or surveys.

Does the research proposed by the student involve human subjects? ☐ Yes (continue below) ☒ No
This research is:
    Approved _____   Date _____

IRB Protocol No. _____

Attach a copy of your IRB approval. Your own name must appear on the original approval or on an attached amendment.

Animal Subjects
The University of Alabama at Birmingham defines a laboratory animal as any vertebrate animal (e.g., traditional laboratory animals, farm animals, wildlife, and aquatic animals) and certain higher invertebrate animals used in research, teaching, or testing at UAB or sponsored through UAB but conducted off-site (i.e., field research or at collaborating institutions, etc.).

Does the research proposed by the student involve animal subjects? ☒ Yes (continue below) ☐ No

This research is:
    Approved ___✓___   Date _November 7, 2012_

IACUC Protocol No. _121209312_ _110208331_

Attach a copy of your IACUC Notice of Approval, showing your research subject and the animal project number. If your own name does not appear on the Notice of Approval, take this form to the IACUC office for verification of approval.

The IACUC office verifies that _QIUXIAG ZHANG_ is covered under the attached approval.
    (name of candidate)

Signature of IACUC representative _Trelli_ Date: _8-22-13_

NOTE: The student's advisor, the student, and the Graduate Program Director agree that no research will be initiated until an application is submitted for review and approved by the appropriate review boards (IRB and/or IACUC) if the proposed thesis or dissertation project requires approval. **If approval already exists, this student's name must be added to the existing protocol before candidacy will be approved by the Graduate School.** It is the responsibility of the student's advisor and the student to comply with federal and UAB regulations associated with this research. Documentation of continuous, appropriate approval will be required before degree conferral; all required IRB and/or IACUC approvals must be current at the time final versions of theses or dissertations are submitted to the Graduate School.

Qiuxiang Zhang   BME   08/22/2013
Student's Signature   Dept.   Date

(signature)   BME   8/21/2013
Signature of Student's Advisor   Dept.   Date

Vladimir Fast   BME   8/22/13
Graduate Program Director   Dept.   Date

Updated 10/31/08